CHARACTERIZATION OF ACTUATION AND FATIGUE PROPERTIES OF PIEZOELECTRIC COMPOSITE ACTUATORS

A Thesis
Presented to
The Academic Faculty
By
Kyle Grant Webber

In Partial Fulfillment
Of the Requirements for the Degree
Master of Science in Mechanical Engineering

Georgia Institute of Technology
August 2005

CHARACTERIZATION OF ACTUATION AND FATIGUE
PROPERTIES OF PIEZOELECTRIC COMPOSITE ACTUATORS

Approved by:

Dr. Christopher S. Lynch, Chairman
School of Mechanical Engineering
Georgia Institute of Technology

Dr. Kenneth A. Cunefare
School of Mechanical Engineering
Georgia Institute of Technology

Dr. W. Steven Johnson
School of Materials Science and Engineering
School of Mechanical Engineering
Georgia Institute of Technology

Date Approved: May 5, 2005

To my step-father for teaching me never to take anything for granted, and my mother for keeping me on the straight and narrow.

ACKNOWLEDGEMENTS

Firstly, I would like to thank my advisor, Dr. Lynch for giving me the opportunity to work on this project and for helping me tirelessly along the way.

I thank Dr. Billy Oates and Dr. Tieqi Liu for answering my barrage of questions nearly everyday.

I thank Matt Hammond, Ameila Case, and Amar Atre for all of their help in everything.

I thank Dr. Kenneth A. Cunefare and Dr. W. Steven Johnson for taking the time to review my work.

I thank the Air Force Office of Scientific Research for generously funding this project through grant F49620-02-1-0030.

Lastly, I would like to thank everyone that has given me a chance.

TABLE OF CONTENTS

LIST OF TABLES

LIST OF FIGURES

LIST OF SYMBOLS

α	coefficient of thermal expansion
ε	strain
γ	shear strain
σ	stress
τ	shear stress
ν	Poisson's ratio
G	shear modulus
E	Young's modulus
ECLIPSE	epoxy composite laminated piezoelectric stress-enhanced
PZT	lead zirconate titanate
THUNDER	thin unimorph-like driver
RAINBOW	reduced and internally biased oxide wafer
LIPCA	lightweight piezo-composite curved actuator
MAC	miniature autoclave
CLT	classical lamination theory
ECLT	extended classical lamination theory
LDV	laser doppler vibrometer
P_s	saturation polarization
E_c	coercive field
Q	electric charge
A	area
D	dielectric displacement

d	piezoelectric constant
k	electromechanical coupling factor
s	compliance
E	electric field
K	dielectric permittivity constant
c	elastic stiffness
e	piezoelectric stress constant
PLZT	lead lanthanum zirconate titanate
APCM	Adhesive Prepregs for Composite Manufacturers
psi	pounds per square inch, unit of pressure
L	actuator length
h	dome height
ρ	radius of curvature
θ	radians, measure of angle
ε_1	strain of top surface of actuator
ε_2	strain of bottom surface of actuator
d_1	distance of neutral axis from top surface
d_2	distance of neutral axis from bottom surface
t	overall actuator thickness
n	number of plies
z(n)	height of arbitrary ply from bottom of laminate
e^o	midplane normal strains
k	bending curvatures in the laminate

z	distance from midplane
e^{σ}	mechanical strain
e^{T}	thermal strain
e^{P}	piezoelectric strain
Q	reduced stiffness matrix
T	transformation matrix
A	extensional stiffness matrix
B	bending-extension coupling stiffness matrix
D	bending stiffness matrix
H	total thickness of laminate
N	normal force
M	moment force
N^{σ}	mechanical loading
N^{T}	thermal loading
N^{P}	piezoelectric coupling
M^{σ}	mechanical moment
M^{T}	thermal moment
M^{P}	piezoelectric moment
L_x	actuator length
L_y	actuator width
$\hat{s}_x^T$	stresses due to thermal expansion in the *x* direction
$\hat{s}_y^T$	stresses due to thermal expansion in the *y* direction
π	potential energy

$\hat{N}_x^T$	normal force due to thermal expansion in the x direction
$\hat{N}_y^T$	normal force due to thermal expansion in the y direction
$\hat{M}_x^T$	moment force due to thermal expansion in the x direction
$\hat{M}_y^T$	moment force due to thermal expansion in the y direction
u^o	displacement approximation in the x diretion
v^o	displacement approximation in the y direction
w^o	displacement approximation in the z direction
a	unknown coefficient
b	unknown coefficient
c	unknown coefficient
d	unknown coefficient
C	stability matrix
V	volt
°C	degrees Celsius, unit measure of temperature
°F	degrees Fahrenheit, unit measure of temperature
CTE	coefficient of thermal expansion
cm	centimeters, unit measure of length - 10^{-2} meters
g	gram, unit measure of mass
GPa	gigapascal, unit measure of stress - 10^9 Pascals
HCF	high cycle fatigue
hrs	hour, unit measure of time - 3600 seconds
LVDT	linear variable differential transformer

μm	micrometer, unit measure of length – 10^{-6} meters
min	minute, unit measure of time – 60 seconds
mm	millimeter, unit measure of length – 10^{-3} meters
μm/m	unit measure of strain (microstrain)
MPa	megapascal, unit measure of stress – 10^{6} Pascals
N	Newton, unit measure of force
Pa	Pascals, unit measure of stress
sec	seconds, unit measure of time
ΔT	temperature change
v_f	fiber volume fraction
Hz	Hertz

SUMMARY

Epoxy composite laminated piezoelectric stress-enhanced actuators (ECLIPSE) have been developed for potential applications by the United States Air Force and others. This class of actuators offers several advantages over other unimorph actuators such as lighter weight, design flexibility, and short production time. Anisotropic differential thermal expansion is utilized in the design of the actuators to achieve large out-of-plane curvature and place the brittle piezoelectric ceramic in residual compression. The numerous composite material choices and configurations can be used to control characteristics of the actuator such as radius of curvature and force output.

ECLIPSE actuators were characterized during this study. They were made from layers of Kevlar 49/epoxy composite and a lead zirconate titanate ceramic (PZT) plate. All ECLIPSE actuators tested were built with a PZT plate with the same dimensions and material, but had different layup configurations. By changing the stacking order of the composite and PZT material, characteristics of the actuator were altered. The performance of each ECLIPSE actuator was compared. The maximum achievable displacement of each actuator was measured by cyclically applying an electric field at low frequency between zero and the maximum electric field allowable for the piezoelectric material. The frequency was also increased to a resonance condition to characterize the fatigue behavior of these actuators. In addition, the force output of various actuators was measured with a four-point bending apparatus. The experimental data was compared to a classical lamination theory model and an extended classical lamination theory model. These models were used to predict actuator behavior as well as to calculate the stress and strain distribution through the thickness of the actuator.

Many key points were understood more fully after this investigation. The design and manufacturing process of ECLIPSE actuators was refined to produce very reliable and repeatable results. The excess material overhanging the PZT plate was minimized, which reduced the weight of actuator per dome height displacement ratio. The manufacturing can now be done with a minimum of space required using much more inexpensive equipment through the development of a miniature autoclave. The stacking order of the actuators has been tested and the effect of adding or reducing the number of composite layers on the displacement and the force production was characterized. It was found that by adding additional 0^{o} plies above the PZT plate the initial height of the actuator is reduced due to increased bending resistance from the stiffer 0^{o} plies, but the predicted stresses in the *y*-direction are in a more compressive state due to the thermal expansion of the added layers. In addition, it was found that by increasing the number of plies in an actuator, the force produced is increased when measured in a four-point bending test fixture. In addition, the fatigue behavior has been shown for fixed-free end conditions and a four-point bending setup. The actuator was shown to have little change due to high cycling for the fixed-free condition, but an apparent decrease in the more rigorous four-point bending test was shown.

CHAPTER 1

INTRODUCTION

Epoxy composite laminated piezoelectric stress-enhanced (ECLIPSE) actuators consist of a PZT ceramic plate sandwiched between layers of a unidirectional Kevlar 49/epoxy composite. Unidirectional Kevlar composite used during this study has anisotropic characteristics. The coefficients of thermal expansion parallel and perpendicular to the fibers are different. Curvature in a composite structure will form when the fibers of one layer are oriented perpendicular to the fibers of another in an unsymmetric layup. If a PZT plate is placed in between the Kevlar plies prior to curing, the entire structure will curve and a beneficial compressive stress will be induced through the brittle PZT. The stress allows the actuator to obtain large displacements without the piezoelectric material cracking. When an electric field is applied to the piezoelectric plate it reacts by expanding or contracting. This reaction is resisted by the composite material which causes a change in the actuator radius of curvature and a visible displacement. If the movement of the actuator is restricted, then a force is produced. This study focuses on actuator manufacturing, characterization of high and low cycle reliability, and actuator force output.

There are many potential applications for ECLIPSE actuators. Because an ECLIPSE actuator is curved, it would fit seamlessly onto a cylindrical structure. These actuators have a very low profile, have lower weight then other actuators made with metal, and can be bonded to the surface of a cylinder easily. Furthermore, these actuators could be readily integrated in to a composite structure, as the actuator is itself a composite. Composites are becoming more common in engineered structures; a

composite based piezoelectric actuator, which could act as a sensor or receiver, would integrate well with these structures. Additional applications include control of low-frequency noise in passenger aircraft cabins (Simpson 1991), torpedo feedback sensors (Sumali 1991), unwanted vibrations in piping systems (White 1972), and submarine hulls (Clark 1993); all of which can be modeled as a cylinder.

ECLIPSE actuators are similar in operation to earlier generations of unimorph actuators, such as THUNDER and RAINBOW. Thin unimorph-like driver (THUNDER) actuators are made from a PZT plate bonded to a stainless steel substrate with LaRC-SI™ polyimide adhesive. The actuator is then cured in an autoclave at a high temperature. Upon removal from the autoclave a curvature and stress gradient are induced in the actuator due to the differences in thermal expansion between the piezoelectric material and stainless steel. Reduced and internally biased oxide wafer (RAINBOW) actuators are fabricated by chemically reducing a PZT plate into a substrate material at a high temperature. Upon cooling the differences in the coefficients of thermal expansion between the piezoelectric material and the substrate cause a curvature and stress gradient. In both the THUNDER and RAINBOW actuators, repoling is necessary after the curing process is completed due to the high curing temperature. ECLIPSE actuators are created using similar concepts, but a different manufacturing process is applied. ECLIPSE actuators are created by cutting and laying up composite plies with a PZT plate located between two layers. The entire stack is cured in an autoclave at a relatively low temperature. Repoling is not necessary after curing is completed due to the low curing temperature of Kevlar/epoxy composite. In addition, composite materials afford greater control over actuator characteristics. By changing the lay-up order, individual layer

orientation, or composite material, the composite actuators can be tailored for specific applications.

A study of previous research on unimorph actuators similar to ECLIPSE actuators is reviewed in Chapter 2. A further review of other unimorph bending actuators is discussed along with a discussion of a class of actuators with two PZT plates called bimorph actuators. The fundamental constitutive relations of piezoelectric theory are also reviewed along with the important characteristics and behaviors of piezoelectric material such as poling, switching, and domain wall motion.

The manufacturing of ECLIPSE actuators is discussed in Chapter 3. The actuator materials are discussed individually along with the orientation of these materials in the final actuator product. The advantages and disadvantages of the chosen composite material are discussed in further detail. A miniature autoclave (MAC) was designed and built to make actuators in the convenience of the lab. MAC allows actuators to be built on a small scale reducing cost over the larger scale autoclave. The mold preparation, curing cycle process, and the post curing process are all discussed.

Due to out-of-plane deflections which are much greater then the thickness, modeling ECLIPSE actuators is difficult. Two models are presented in Chapter 4. The first model uses classical lamination theory to predict actuator behavior. Although this model is a good approximation, it is still a linear theory which cannot model non-linear behavior found in ECLIPSE actuators. The second model presented is the extended classical lamination theory which was developed at Virginia Tech by Michael Hyer. This model uses approximate displacement expressions which contain unknown coefficients. These coefficients are solved for by a series of substitutions and the

minimization of a potential energy function. This technique contains non-linear terms in the strain relationships which help to account for non-linear actuator behavior. Both models were used to find the stress and strain distribution throughout the thickness of the actuators. This was done to ensure that the brittle piezoelectric plate remained in compression to prevent cracking. The strain distribution was also used to determine the neutral axis of the actuator. Neither the CLT nor ECLT models, which were used to predict the response of the actuators to an electric field, considered the hysteresis of the piezoelectric material, which is due largely to domain wall motion.

The experimentation and characterization results are seen in Chapter 5. ECLIPSE actuators were characterized by measuring the change in dome height of the actuator with a linear variable differential transducer (LVDT). The dome height of the actuators is related geometrically to the radius of curvature which can be calculated in CLT and ECLT. The change in dome height with change in electric field was studied for each different actuator layup and compared to both laminate theory models. The effect of moisture absorption by the composite material on the dome height displacement was also investigated. Additionally the cure temperature sensitivity of the models was tested and compared to measured values of actuators cured at various temperatures ranging from 157^{o}C to 197^{o}C. Fatigue testing was performed on the actuators to determine the useful service life. The resonant frequency was measured using a laser doppler vibrometer (LDV). Actuator specimens were cycled in an electric field range of 0 MV/m to 2 MV/m at resonance while a different set of actuators were tested at one half their measured resonant frequency with the same electric field range. All actuators tested were cycled unconstrained in a cantilevered setup. Cycling was stopped

periodically to measure the displacement capabilities of the actuator to determine a decrease in performance. Finally, force output was measured using a four point bending apparatus and compared to the calculated values found in CLT and ECLT.

Chapter 6 discusses the conclusions of the experimental and modeling results. Recommendations are also made for future research.

CHAPTER 2

BACKGROUND AND LITERATURE REVIEW

2.1 Piezoelectricity

In 1880 Pierre and Jacques Curie first discovered the piezoelectric effect, which is found in many common materials such as tourmaline, quartz, topaz, cane sugar, and Rochelle salt. They discovered that a surface charge could be measured when a mechanical stress was applied to certain crystals which had been given a surface treatment. The brothers also discovered that there was a relationship between temperature and surface charge intensity. The Curie brothers did not, however, predict that the "converse piezoelectric effect" was possible (electricity from a mechanical stress). It was not until 1881 when Gabriel Lippmann, Marie Curie's thesis advisor, proved mathematically that the converse piezoelectric effect was possible. The Curie brothers quickly completed experiments to show that it was indeed possible.

2.1.1 Piezoelectric Unit Cell

Ordinary solid materials, when subjected to a stress, display a strain proportional to the elastic modulus. Ferroelectric materials, or piezoelectric materials capable of reversing their polarization direction, are a crystalline material which also have a coupling between applied mechanical stress and electric polarization. If a mechanical stress in *x*-direction is applied which causes an electric displacement in the *y*-direction, then conversely, applying an electrical field in the *y*-direction will cause a mechanical displacement in the *x*-direction (Cady 1964). There are many naturally occurring materials which have this electromechanical coupling. A few such materials are

tourmaline, quartz, topaz, cane sugar, and Rochelle salt. Manufactured materials more commonly used for engineering applications include barium-titanate ($BaTiO_3$), lead titanate ($PbTiO_3$) and lead-zirconate-titanate (PZT) ($Pb(Ti,Zr)O_3$).

The piezoelectric effect is due to a lack of charge symmetry about the center of a piezoelectric unit cell. A unit cell is the smallest three-dimensional atomic structure that is repeated throughout and still shows crystal symmetry (Jaffe 1971). A schematic of a unit cell is shown in Figure 2.1. The piezoelectric effect is dependent on temperature. Above a certain temperature, defined as the Curie point, there is no piezoelectric effect. Above this temperature the unit cell is in an isotropic body centered cubic state (paraelectric), shown in Figure 2.1a. As the ambient temperature falls below the Curie point, the unit cell starts to form a polarized tetragonal structure (ferroelectric), shown in Figure 2.1b. Once below the Curie point the piezoelectric properties start to appear. As can be seen in the unit cell in Figure 2.1b, the piezoelectric effect is due to the positively charged titanium ion shifting away from the center location and above the plane of the negatively charged face centered oxygen ions. In the configuration shown in Figure 2.1, the top of the unit cell is positively charged and the bottom is negatively charged. This indicates the poling direction.

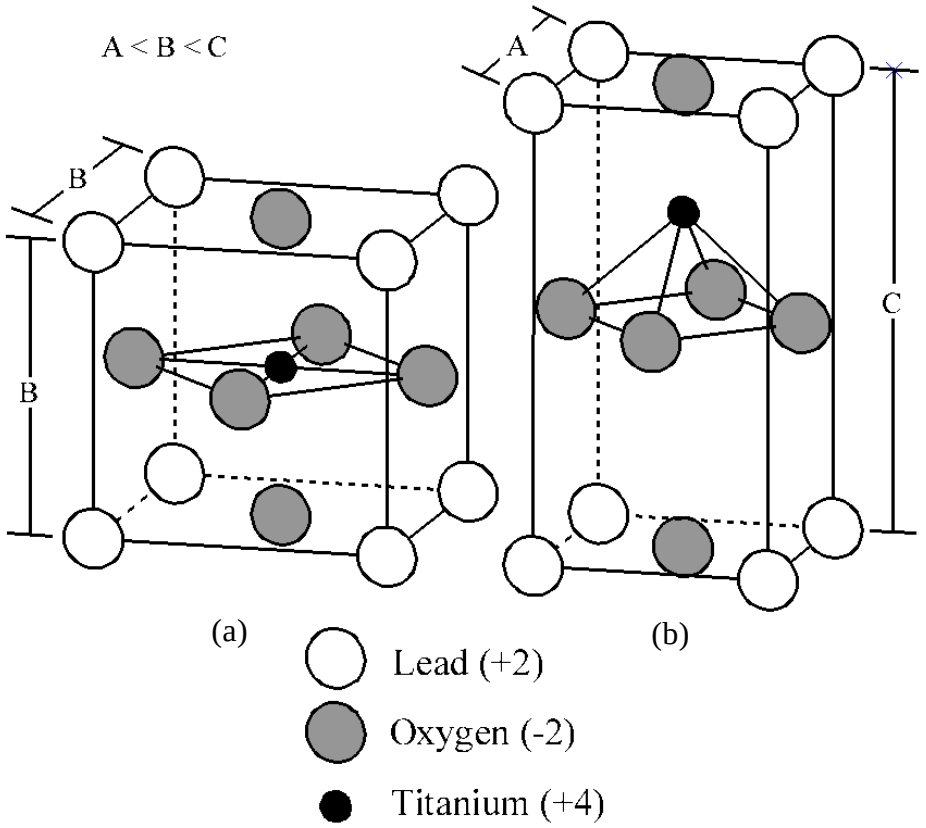

Figure 2.1. Cubic (a) and tetragonal (b) unit cells.

2.1.2 Poling and Switching

The poling direction is dependent on the location of the positively charged titanium ion in relation to the plane of negatively charged oxygen ions. A schematic of a poled unit cell is shown in Figure 2.2a. If an electric field is applied in the direction opposite to the poling direction, the titanium ion will be forced closer to the center, thereby reducing the overall height of the unit cell, as shown in Figure 2.2b. A compressive stress acts in a similar fashion as an electric field in the reverse direction by reducing the unit cell height, as shown in Figure 2.2c. At small loads this is approximately a linear response. In either case, if the electric field or mechanical stress become too great and exceed the coercive level the titanium ion will be forced past the

center plane of oxygen atoms, and the polarity will be reversed (Mauck 2002). This is referred to as “switching”. In the case of the electric field (ferroelectric switching), the polarization will be switched by 180^{o}, as shown in Figure 2.2d. In the case of the mechanical stress (ferroelastic switching), the polarization will shift to one of the four possible 90^{o} directions, as shown in Figure 2.2e. Conversely, if a tensile load or an electric field in the direction of the polarization is applied, the unit cell will elongate as shown in Figure 2.2f.

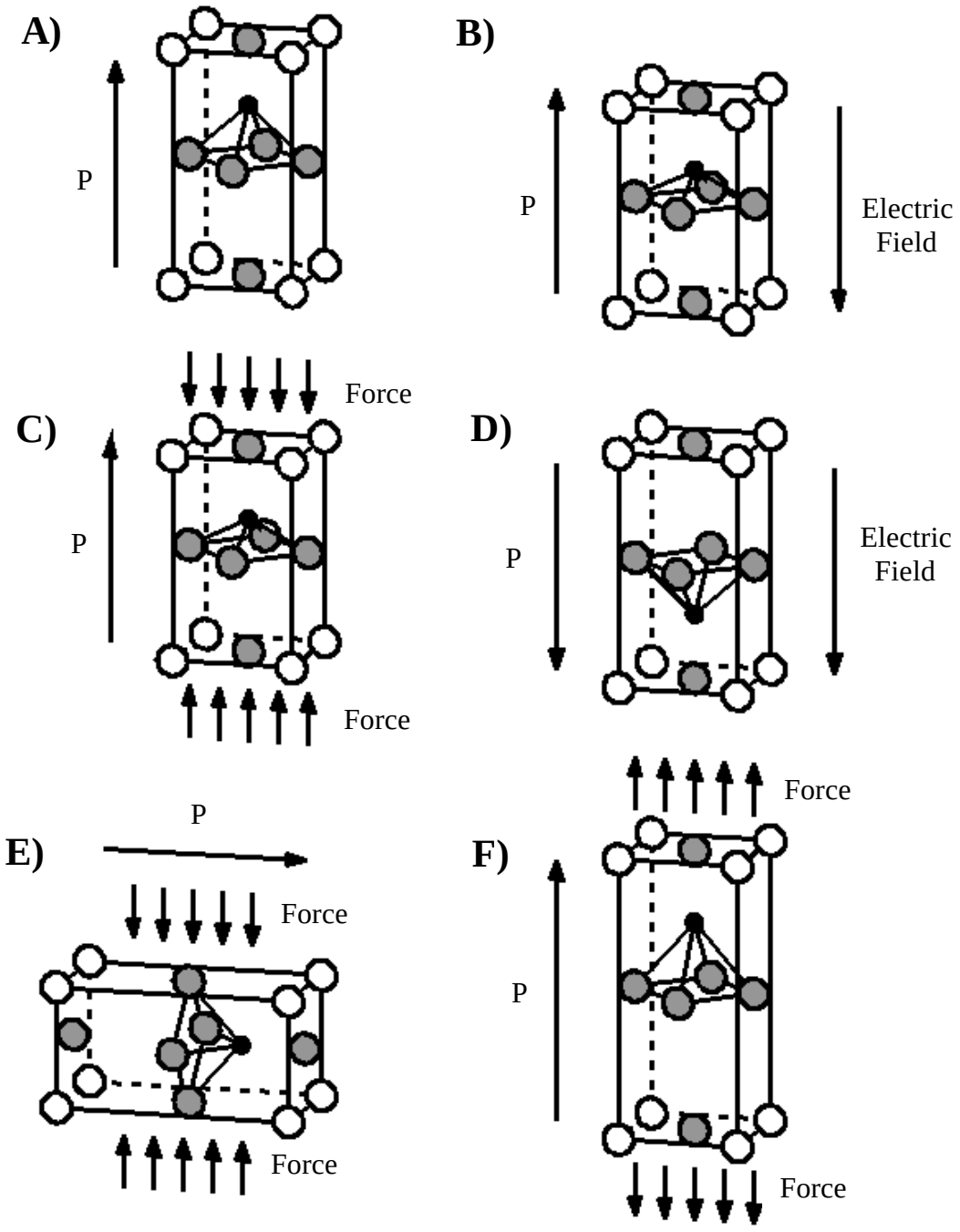

Figure 2.2. Schematics of various unit cell conditions.

A piezoelectric ceramic is a large collection of randomly oriented crystals, each with a polarization vector pointed in various directions. Each unit cell contains a dipole, which is a result from the differences between the center of the positive charges and the center of the negative charges found in the unit cell (Jaffe 1971). When this ceramic is cooled below the Curie point there is no instantaneous poling. When an electric field is applied to this random orientation of domains, groups of diploes with common orientation, each react in their respective directions and cancel the forces of one another. For this reason an unpoled piezoelectric material will not produce any useful work. A piezoelectric material must be poled to produce useful work. The alignment of polar axes in a ceramic can never be as perfect as in a single crystal material because of the originally random orientation of the domains (Jaffe 1971). Intergranular stresses which inhibit the reorientation of domains and imperfections which cause strains in the material, that act similarly, both prevent the ceramic from realizing perfect polarization. A schematic of a piezoelectric specimen before poling is shown in Figure 2.3a. If a small electric field is applied to the material the dipoles will begin to line up with the direction of the electric field. If this electric field is increased to a high level, then the dipoles will continue to move, until they are aligned with the applied electric field and will become poled. A schematic of a piezoelectric specimen during poling is shown in Figure 2.3b. When the electric field is removed the dipoles will relax slightly and the material will have a remanent polarization in the direction that the field was applied, as shown in Figure 2.3c.

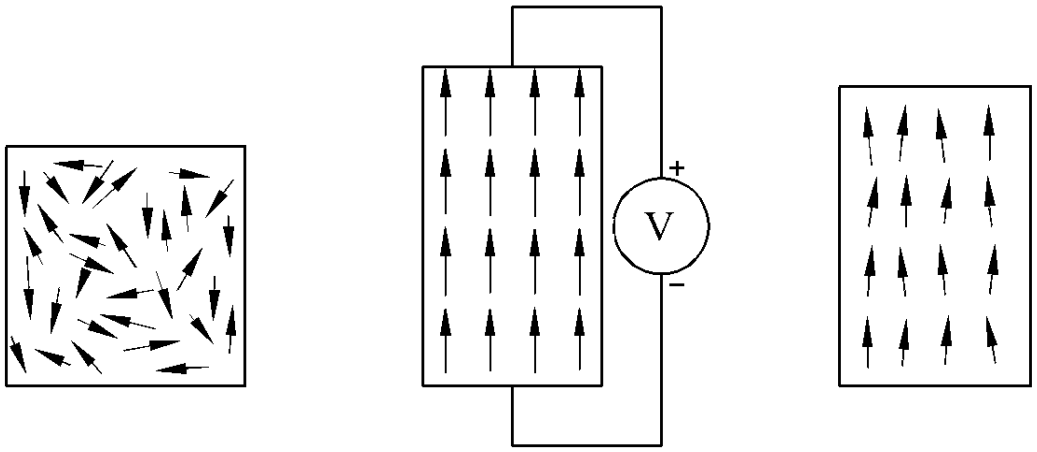

Figure 2.3. Domain orientations before (a), during (b), and after (c) polarization

Polarization switching is a non-linear process that contributes to hysteresis. A hysteresis curve is shown in Figure 2.4 (Brown 2003). The *y*-axis represents the polarization and the *x*-axis represents the applied electric field. Initially, before an electric field has been applied to the crystal, it is in the unpoled state. As an electric field is applied to the crystal it begins to become polarized, with the initial path shown with the dotted line. The non-linearity of the polarization can also be seen here. When the electric field has reached the coercive field, the saturation polarization, P_s, has been obtained. At the saturation polarization the domains have aligned themselves as close to parallel with the applied electric field as possible. If the electric field was removed after the maximum electric field had been applied, the polarization would not follow the dotted line in reverse direction, but follow the solid line to the remanent polarization point, P_r. This is due to the domains "relaxing". Upon application of a negative electric field, the

polarization will begin to decrease. When the electric field has been forced past the coercive field, E_c, the polarization switches to 180^o from the initial poling direction.

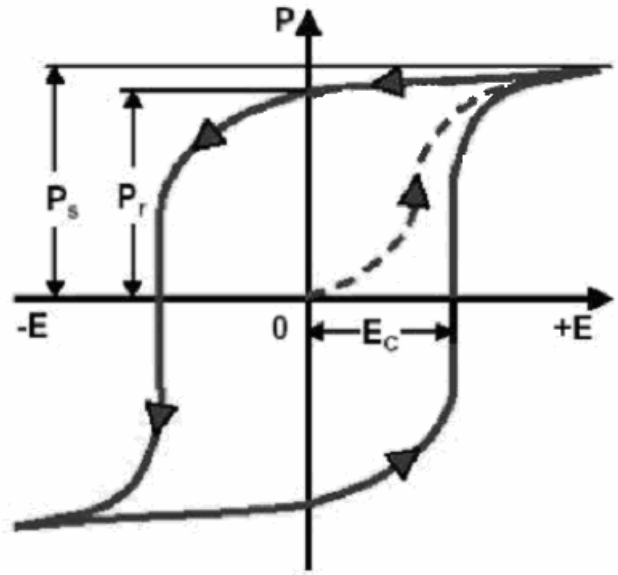

Figure 2.4. A typical dielectric hysteresis curve.

2.1.3 Domain Walls and Domain Wall Motion

An unpoled piezoelectric ceramic material is a collection of many dipoles randomly oriented throughout the material. Groups of dipoles oriented in the same direction are known as domains. There is no limit to the number of domains in a material, as there can be multiple different domains in a single specimen. The boundary between two different domains is called a domain wall. If a material has been perfectly poled in one direction, then the material consists of one large domain. When an electrical or mechanical stress is applied to the material past the coercive level, the entire material will not simultaneously change polarization. Initially one unit cell will switch polarization followed by the surrounding unit cells. This effect will "sweep" through the

material eventually switching the polarity of each unit cell until there is again only one domain. This is referred to as domain wall motion. Due to the sweeping effect, domain wall motion is a non-linear effect. A material does not have to be poled in one direction for domain wall motion to occur.

2.1.4 Constitutive Laws

To effectively use piezoelectric materials the response to applied stresses and electric fields must be characterized. During the linear response of piezoelectrics, the stresses and strains can be modeled by combining the elastic terms, governed by Hooke's Law, with the additional piezoelectric effect term. The direct piezoelectric effect is the augmentation of the electric charge with applied mechanical stress. The charge is proportional to the force applied and is expressed as the dielectric displacement, the charge Q per unit area A. In the following equation the dielectric displacement, D, is related to the stress, s, with the piezoelectric constant d (expressed in Coulombs/Newton).

$$D = Q/A = d \cdot s \tag{2.1}$$

The converse piezoelectric effect, where a strain, e, is produced by the application of an electric field E and is related by the converse piezoelectric constant, is expressed in the following equation.

$$e = d \cdot E \tag{2.2}$$

For both cases, direct and converse, the values are identical for the piezoelectric constant. The piezoelectric constant is very important to the design of a piezoelectric actuator as it relates the applied electric field to the amount of strain produced. The

piezoelectric constant is a third order tensor. The most important value for ECLIPSE actuators is the d_{31} term, which relates the electric field applied through the thickness of the actuator to the amount of strain along the length. This determines the amount of displacement, or force, which can theoretically be produced. As the piezoelectric constant is increased the performance of the actuator will also increase.

Another important measurement of the strength of a piezoelectric material is the electromechanical coupling factor, *k*. The electromechanical coupling factor relates the amount of the applied electric field converted to mechanical energy or conversely the amount of applied mechanical stress to electricity. This factor effectively gives the efficiency of the piezoelectric material. Since there are losses in any system, *k* is always less than one. Other piezoelectric material properties contribute to the performance of the actuator such as Young's modulus and thermal expansion.

The fundamental constitutive relations for piezoelectric materials can be formulated by combining the piezoelectric effect with the Hooke's law relations. These constitutive equations are shown in Equations 2.3 (Lines 1977).

$$\begin{aligned} e_{ij} &= s^{\mathrm{E}}_{ijkl} s_{kl} + d_{mij} \mathrm{E}_m \\ D_k &= d_{klm} s_{lm} + K^{s}_{kp} \mathrm{E}_p \\ s_{ij} &= c^{\mathrm{E}}_{ijkl} e_{kl} - e_{mij} \mathrm{E}_m \\ D_m &= e_{mkl} e_{kl} + K^{e}_{kp} \mathrm{E}_p \end{aligned} \tag{2.3}$$

Where e is the strain, s is the compliance, s is the stress, d is the piezoelectric constant, E is the electric field, D is the electric displacement, K is the dielectric permittivity constant, c is the elastic stiffness, and e is the piezoelectric stress constant; indices vary from 1 to 3. The superscripts E, s, and e indicate that the electric field,

stress and strain, respectively, are held constant for the particular variable they are paired with.

These relationships are only for the linear response and do not completely describe the behaviour of a piezoelectric material. As the electric field is increased the piezoelectric effect saturates and tapers off (Lynch 1996). This effect can be seen in Figure 2.5 (Lynch 1996), where the longitudinal strain in the *z*-direction is found on the *y*-axis and the electric field is on the *x*-axis. Initially the material has no remanent polarization or strain before it has been subjected to an electric field. The unpoled piezoelectric material follows the dotted line when an electric field is initially applied. After the material has been cycled several times it forms a stable hysteresis loop. At point A there is no electric field, but a positive remanent polarization and remanent strain. When a positive electric field is applied the strain begins to increase, but as the electric field gradually increases the change in strain for each increment of change in electric field starts to decrease.

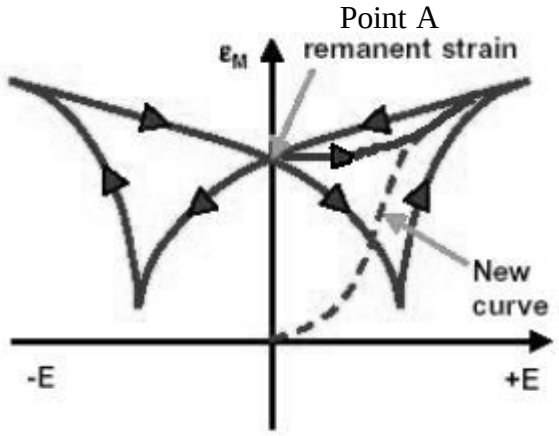

Figure 2.5. Longitudinal-strain-electric field loop.

2.2 Bending Actuators

Unimorph and bimorph actuators are both types of *31*-mode actuators in the "bender" class. Both types utilize the d_{31} piezoelectric coefficient to accomplish actuation. A unimorph bending actuator consists of only one piezoelectric layer bonded to an inactive material (Smits 1990). The PZT layer and the non-piezoelectric material each have a different coefficient of thermal expansion which when cured causes a curvature in the actuator and a residual compressive stress. When an electric field is applied it causes the PZT plate to either expand or contract, while the inactive layer resists this motion, causing the actuator to bend. Figure 2.6 shows a schematic of this reaction.

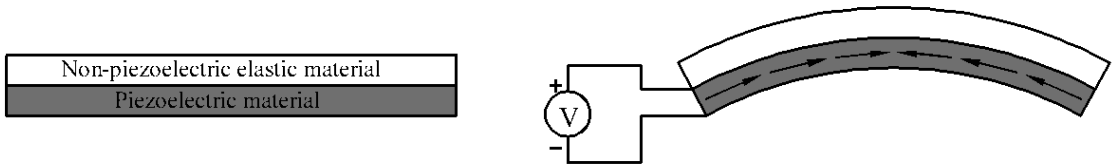

Figure 2.6. Schematic of unimorph actuation

2.2.1 Commercially Available Unimorph Actuators

Unimorph actuators are capable of very high displacements, but do not create exceptionally high forces. RAINBOW, THUNDER, and LIPCA actuators are commercial examples of unimorph actuators. A picture of a THUNDER actuator is shown in Figure 2.7.

Figure 2.7. Picture of a THUNDER actuator.

RAINBOW (Reduced and internally biased oxide wafer) actuators were the first devices to utilize the high force capabilities of piezoelectrics and a mechanical advantage mechanism to produce higher displacements then achievable with the piezoelectric material alone (Haertling 1994, Mulling 2000). RAINBOW was introduced by Haertling in 1994 and consists of a PLZT (lead lanthanum zirconate titanate) disk that has been reduced at high temperature into the surface layer of a non-piezoelectric wafer (Haertling 1994). The PLZT disk actually diffuses into the non-piezoelectric wafer and upon cooling forms a dome shape due to the differences in thermal expansion. The PLZT material must be poled after curing.

The THUNDER (Thin layer unimorph ferroelectric driver and sensor) actuator, similar in principal to the RAINBOW actuator, uses a different method to cause curvature (Mulling 2000, Ounaies 2001). A THUNDER actuator consists of a PZT plate bonded to a non-piezoelectric material, typically stainless steel, with the use the high temperature polyimide adhesive, LaRC-SI™. On the other side of the PZT plate a thin piece of aluminium foil is bonded using the same adhesive. Both the stainless steel and the aluminium serve as electrodes. Upon cooling from the 350 ^{o}C cure temperature, the structure curves due to the differences in thermal expansion between the stainless steel and PZT material.

A new generation of unimorph actuators is utilizing composite materials to reduce weight and add flexibility in design. LIPCA (Lightweight piezo-composite curved actuator) actuators are an example of such an actuator. LIPCA was introduced by Yoon et al in 2000 (Yoon 2001, Yoon 2001, Yoon 2000). LIPCA actuators consist of a carbon/epoxy layer electrically insulated by glass/epoxy layers, with a PZT plate in the middle and a glass/epoxy layer on the bottom. LIPCA utilizes the difference in thermal expansion in orthogonal direction of the composite material to induce curvature.

2.2.2 Bimorph Actuators

Another actuator in the bender class is the bimorph actuator. Bimorph actuators consist of two electroded piezoelectric layers poled along their thickness and adhesively bonded together (Kugel 1997). The polarity of the piezoelectric layer can either be in the same direction (parallel configuration), or in opposing directions (series configuration). A bimorph actuator that is in the parallel configuration is setup to only actuate in one direction. The addition of the extra PZT plate simply adds to the available force and displacement output of the actuator. A bimorph actuator that is in the series configuration is able to bend in either direction with less displacement or force in either direction then the bimorph with a parallel configuration. Series bimorphs are typical flat. Figure 2.8 shows the series and parallel configuration.

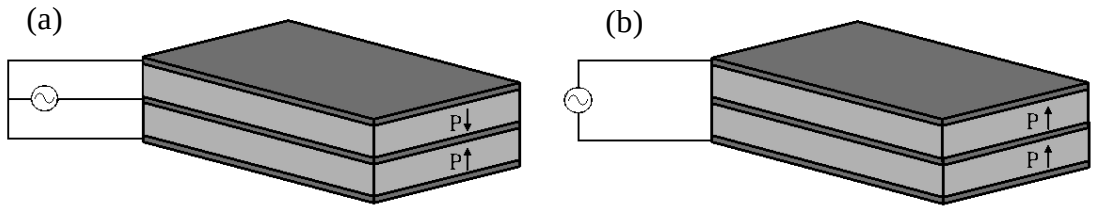

Figure 2.8. Schematics of a series (a) and parallel (b) bimorph actuators.

There are two actuation schemes for a series bimorph. During actuation of the bimorph in one direction, one PZT plate is actuating to the full scale, while the other PZT plate can either remain inactive or can be actuated negatively. Care must be taken to not force the piezoelectric plate past the coercive field because repolarization will result. If the secondary PZT layer is actuated negatively it adds to the developed displacement or force of the bimorph. The overall strain that is produced by a PZT plate is relatively low. This requires that the PZT plates in a bimorph actuator be located as closely as possible the neutral axis to receive the most usefulness.

CHAPTER 3

ACTUATOR MANUFACTURING

3.1 Actuator Materials

The unimorph design consists of one piezoelectric element bonded to a non-piezoelectric substrate. Upon cooling from an elevated curing temperature, a curvature is induced. Actuators of this type can be used in such applications that include control of low-frequency noise in passenger aircraft cabins (Simpson 1991), torpedo feedback sensors (Sumali 1991), unwanted vibrations in piping systems (White 1972), and submarine hulls (Clark 1993); all of which can be modeled as a cylinder. This study focuses on unimorph actuators made from Kevlar 49/epoxy composite and PZT.

3.1.1 Piezoelectric Material

The piezoelectric material used for the ECLIPSE actuators in this study was ceramic PZT, $Pb(Ti,Zr)O_3$. The specific brand was 3195HD, manufactured by CTS Communications Components, Inc. This material is comparable to Department of Defense type VI PZT. CTS 3195HD is a soft PZT material which displays large piezoelectric coefficients, high strain, and high hysteresis. Soft PZT is used in unimorph actuators because of the high value of the d_{31} piezoelectric constant. This constant relates the applied electric field through the thickness of the PZT plate to the amount of strain produced along its length. The piezoelectric d_{31} constant for 3195HD is listed by the manufacturer as -190×10^{-12} m/V. The negative value indicates that as the electric field is applied parallel to the poling direction, X_3, the PZT material shrinks in the direction perpendicular to the poling direction, X_1. For this study all of the PZT plates were cut

from the same block of material and had the same dimensions of 3.08in x 2.29in x .010in (78.2mm x 58.1mm x 0.254mm). The plate thickness was selected to minimize the overall thickness and weight of the actuators. Thinner plates were difficult to handle, as the ceramic material is brittle and would easily break during assembly. Both the top and the bottom of the plates had silver electrodes.

3.1.2 Unidirectional Composite Material

Creating unimorph actuators from composite materials has the advantage of a broad range of design parameters. The anisotropy of the composite material plies as well as the numerous material choices were used to control the characteristics of the actuator. For the purposes of this study, a unidirectional pre-impregnated (prepreg) Kevlar 49/epoxy composite was chosen. One reason for selecting Kevlar 49/epoxy is the coefficients of thermal expansion are higher then other common unidirectional composite materials (Mallick 1993). Prepreg composite materials give the advantage of quick layup time as well as repeatability and ease of production. Prepregs are thin sheets of evenly distributed fibers with a uniform distribution of epoxy already attached (Mallick 1993). During the cure cycle the epoxy thermoset was heated and flowed around the fibers before it cured. The added pressure and vacuum applied in the autoclave insured that any entrained air was forced out.

Composite materials are found in many different variations, with many choices available for the constituent parts. There are various fiber configurations available, but the most common types are unidirectional, chopped fiber, particle, and woven mat. Figure 3.1 shows pictures of various fiber configurations.

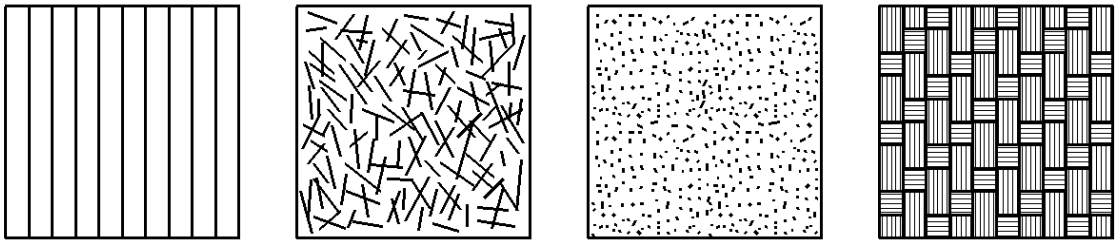

a) Unidirectional b) Chopped Mat c) Particle d) Woven Fiber

Figure 3.1. Various fiber configurations for composite materials

The matrix material is responsible for transferring stresses between the fibers, providing a barrier to the environment, and protecting the surface of the fibers from mechanical abrasion (Mallick 1993). There are many matrix material choices. Although epoxy is commonly used, other thermosets and even thermoplastics are available. Epoxy was chosen because of its low molecular weight and high curing temperature compared to other matrix materials such as thermoplastics. The combination of the high thermal expansion of the composite and the high curing temperature of the epoxy causes greater curvatures and compressive forces then other material choices. Epoxy also has excellent resistance to chemicals and solvents.

The fiber material chosen for this study was unidirectional Kevlar 49 because Kevlar 49 fibers have the lowest density and the highest tensile strength-to-weight ratio among available reinforcing fibers. In addition, Kevlar 49 fibers have better chemical and thermal stability then other organic fibers. Although Kevlar 49 has a high tensile strength, it reacts poorly in compression. Due to weak hydrogen bonds in adjacent molecules in the transverse direction Kevlar 49 has a high degree of longitudinal splintering, or brooming (Mallick 1993). This trait gives Kevlar 49 excellent damage tolerance during dynamic loading and is the reason it is useful for body armor. Kevlar

fibers are very sensitive to ultraviolet lights which can cause discoloration and loss in tensile strength. Discoloration can be seen in Figure 3.2. The material exposed to ultraviolet light is seen on the left while the other specimen kept in a dark environment is on the right.

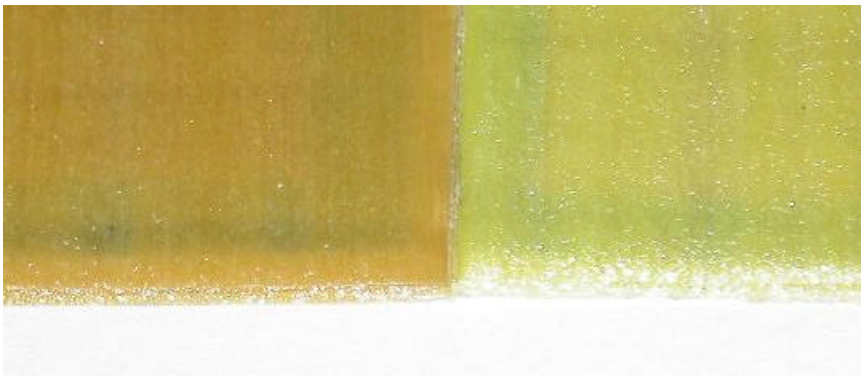

Figure 3.2. Discoloration of Kevlar 49/epoxy due to light expose.

Moisture absorption is also a concern for Kevlar 49. Typically for glass, carbon, and boron fibers the amount of moisture absorbed relative to the amount of matrix material is insignificant. This is not that case for Kevlar 49. This results in Kevlar 49 reinforced composites absorbing more water than other composites. In addition, Kevlar 49 also displays creep behavior, unlike glass, carbon, or boron fibers (Sturgeon 1978).

The specific composite material used was DA-4518K manufactured by Adhesive Prepregs for Composite Manufacturers (APCM). The prepreg composite is available with either an epoxy that cures at 121 ^{o}C (250 ^{o}F) or 177 ^{o}C (350 ^{o}F). The epoxy with the higher curing temperature was chosen in spite of being closer to the Curie point of the piezoelectric material because the higher curing temperature causes a greater residual stress in the actuator after curing. The coefficient of thermal expansion (CTE) for the Kevlar 49/epoxy composite used is different in the orthogonal directions. The CTE in

the Kevlar/epoxy composite is such that there was a contraction perpendicular to the fibers and an expansion parallel to the fibers after cooling from the cure temperature. The CTE perpendicular to the fibers is principally controlled by the material properties of the epoxy material and the CTE in the direction parallel to the fiber is principally controlled by the fibers. The thickness of a single layer of Kevlar 49/epoxy after curing was measured as approximately 0.20 mm.

3.1.2.1 Chemical Shrinkage

The residual stresses in composite structures are principally caused by the difference in volumetric change between the matrix material and the fibers (Lahtinen 2003). Two mechanisms that can cause volumetric changes are thermal shrinkage and chemical shrinkage. Thermal shrinkage is caused by the differences in the coefficients of thermal expansion between the matrix material and the fibers. The stresses due to thermal shrinkage can be altered simply by removing or adding heat to the composite material. When a composite structure is heated back to the curing temperature it returns to a stress free state. The stresses caused by thermal shrinkage will return when the temperature is again lowered to room temperature. Chemical shrinkage, however, is irreversible and does not change with time. Chemical shrinkage is caused by the contraction of the matrix material molecules during crosslinking and therefore depends on the chemical composition and the polymerization reaction (Daniel 1990).

It has been shown that the effects of chemical shrinkage on the residual stresses in a composite laminate can be significant (Daniel 1990, Yoon 2001, Lahtinen 2003, and Gigliotti et al. 2003). These stresses, however, do not contribute large amounts of

additional curvature for the case of flat, unsymmetric composite panels that are constrained during the curing process. It has been shown by Potter and Wisnom that if an unsymmetric composite laminate is free to shrink in any direction during curing then chemical shrinkage can play a significant role in producing curvature. However, if the composite laminate is constrained in the form of vacuum and pressure inside of the autoclave then the most of the chemical shrinkage occurs in the out-of-plane, thickness direction as shown in Figure 3.3. Because the curvature is small, a state of plane stress is assumed, and the stresses that the shrinkage in the thickness direction causes are not considered. Due to this, chemical shrinkage was not considered in the classical lamination theory model.

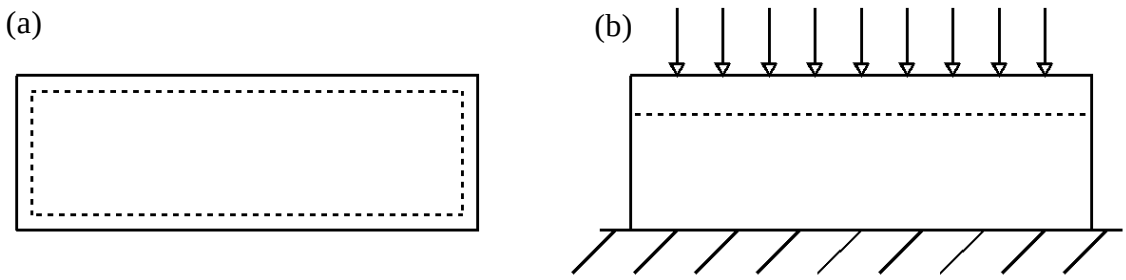

Figure 3.3. Chemical shrinkage for an unconstrained (a) and constrained (b) composite laminate panel.

3.1.3 Electrode Material

To create an electric field through the PZT plate wrapped in an electrical insulator there must be some method used to make electrical contact with the piezoelectric. The material used for the electrodes was a thin copper foil material that was perforated to form a mesh. This copper foil mesh was manufactured by Dexmet Corporation. The meshing allows the epoxy to flow through the perforations during curing and adhere to

the PZT plate. The copper mesh was interspersed with solid pieces of copper that acted as the soldering points. The copper mesh was laid along the whole length of the PZT. The electrode tab configuration used during testing is shown in Figure 3.4. In this configuration the two terminals protrude on opposite sides.

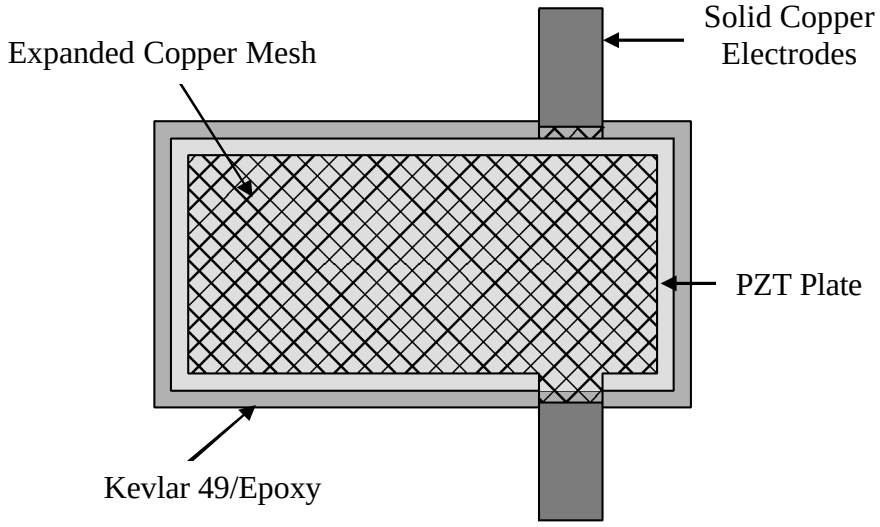

Figure 3.4. Schematic of standard electrode configuration.

3.1.4 Material Properties and Dimensions

Table 3.1 summarizes the material properties of the constitutive materials used in the modeling of the ECLIPSE actuators.

Table 3.1. Summary of material properties

	Kevlar 49 / epoxy	CTS 3195HD PZT
E_{11} (GPa)	55.8	67
E_{22} (GPa)	5.5	67
G_{12} (GPa)	2.1	25.6
v_{12}	0.31	0.31
d_{311} (pm/V)	-	-190
d_{322} (pm/V)	-	-190
α_{11} (με/K)	-3.6	3
α_{22} (με/K)	54	3

All actuators tested were made with a PZT plate with dimensions 77.47mm x 29.21mm x 0.254mm (3.05in x 1.15in x 0.01in) poled in the [001] direction. Figure 3.5 shows the coordinate systems and poling directions. The final length and width dimensions of the actuators were 82.55mm x 34.29mm (3.25in x 1.35in) with different thicknesses dependent on the number of composite layers utilized. A small amount of overhanging Kevlar material was necessary to ensure that the PZT plate was securely surrounded by composite material. This overhang was limited to 2.54mm (0.1in) for electrical insulation. It is interesting to note that as the amount of Kevlar material extending past the edge of the PZT plate decreased; the model predictions came closer to the measured values. As the overhang increased, the model under-predicted the initial dome height while continuing to correctly predict the change in dome height.

3.2 Actuator Design

Five different layups were considered in this study; [90/PZT/90/0], [90/90/PZT/90/90/0], [90/90/PZT/90/0/0], [90/90/90/PZT/90/90/0/0], and [90/90/90/PZT/90/0/0/0]. Previous generations of ECLIPSE actuators had large amounts of Kevlar composite material hanging over the edge. This overhanging material was left to provide a platform for the electrode to be secured to. The actuator design has been improved by removing this extraneous material and leaving the electrode tabs unsupported, thereby reducing the actuator weight. Figure 3.5 shows an exploded view of the layers in a [90/90/PZT/90/90/0] layup. Figure 3.6 shows a picture of a cured ECLIPSE actuator.

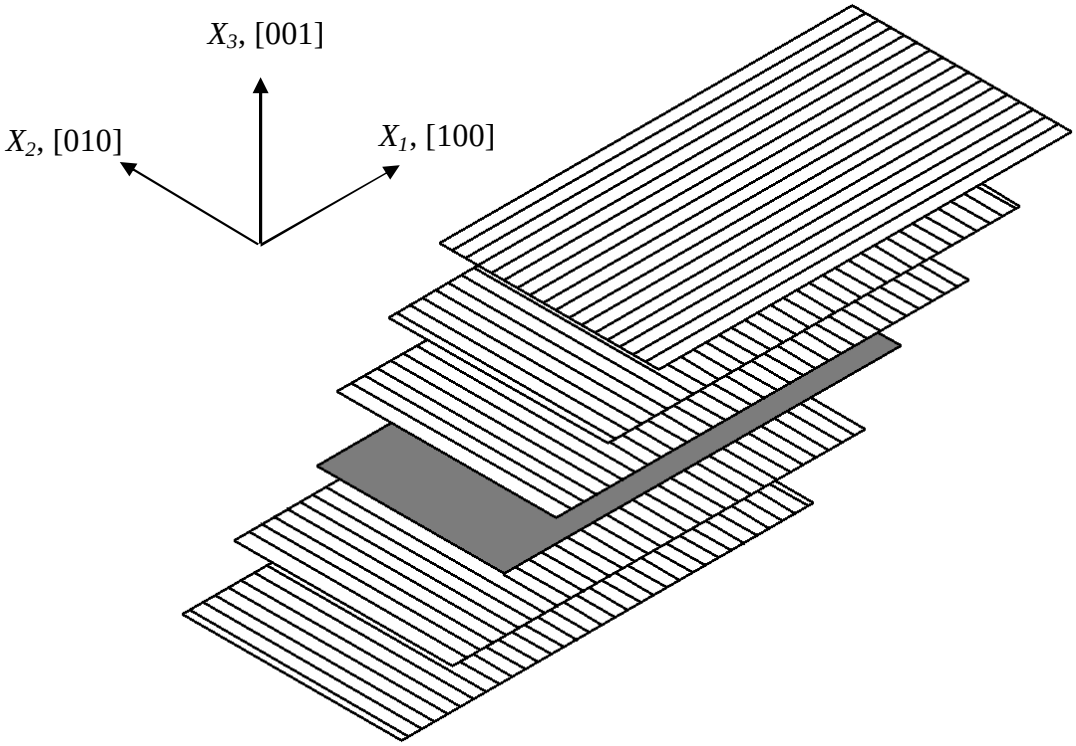

Figure 3.5. [90/90/PZT/90/90/0] actuator layup schematic.

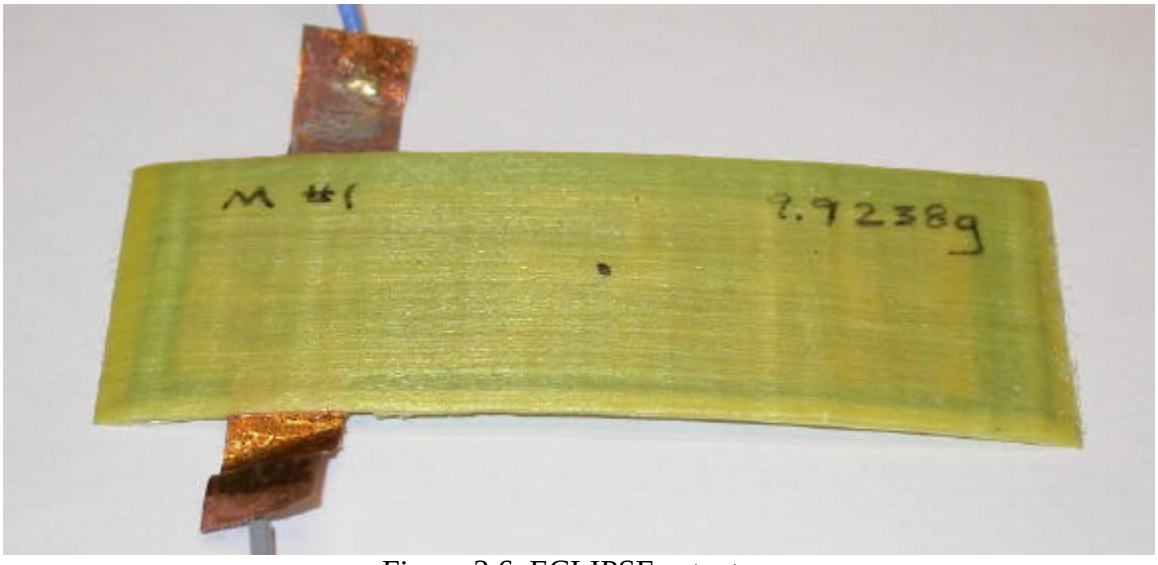

Figure 3.6. ECLIPSE actuator.

3.3 Miniature Autoclave

A miniature-autoclave (MAC) was created at the Georgia Institute of Technology by Christopher Lynch's research group that has the capability to produce multiple actuators daily without the expense of a full scale autoclave. The MAC consists of a steel box with removable top and bottom aluminum plates. The box is made from 0.635 cm thick steel plate and measures 33 cm x 33 cm x 20 cm, while the aluminum plates are both 43 cm x 43 cm x 0.953 cm. The structure was sandwiched together with sixteen tie rods along the edge of the box. The unit was sealed with a high temperature gasket recessed into the top and bottom aluminum plates. The actuator mold fits inside and there are both a pressure and a vacuum connection on the side off the MAC. The air pressure was controlled by a wall mounted regulator, supplied by shop air and the vacuum was created by a small low flow vacuum pump. Inside a vacuum connection is hard-piped to the vacuum bag connection. A schematic line drawing can be seen in Figure 3.7. A picture of the MAC can be seen in Figure 3.8.

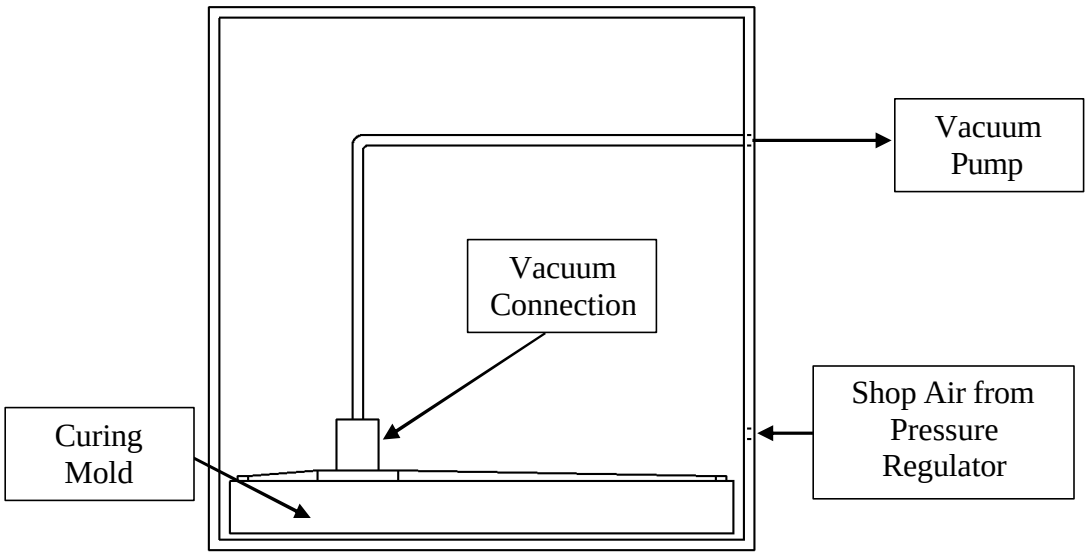

Figure 3.7. Schematic line drawing of MAC.

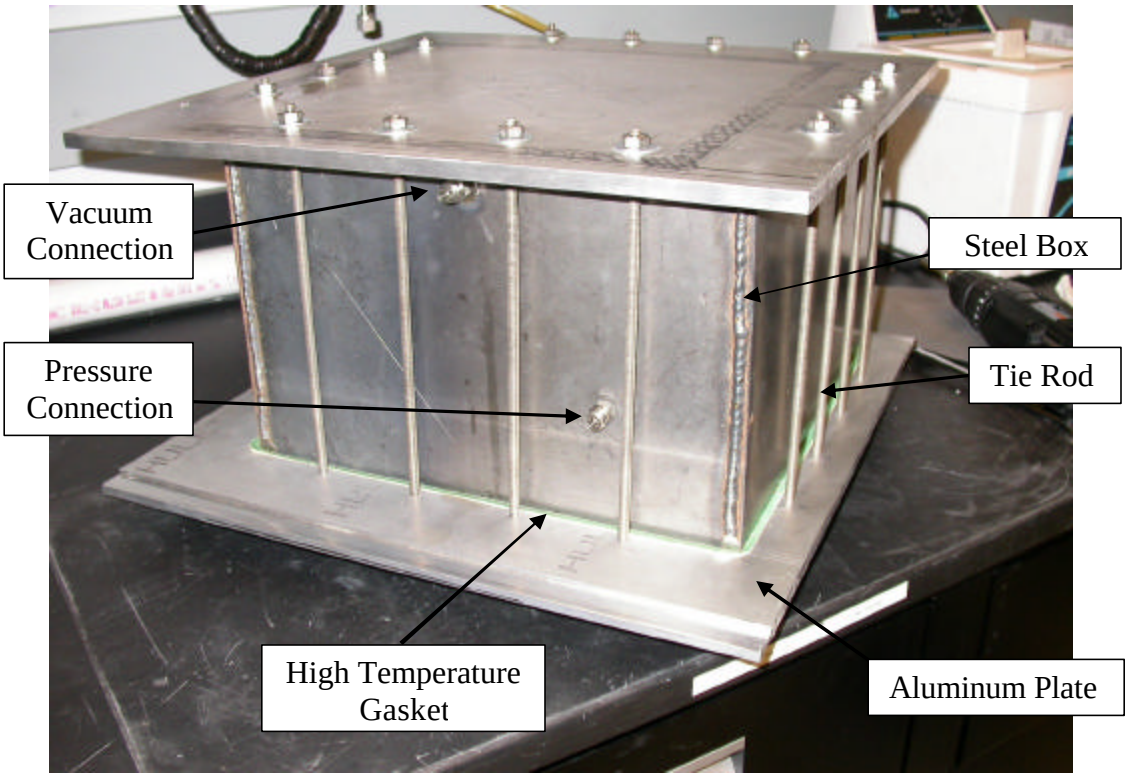

Figure 3.8. Miniature autoclave.

3.3.1 Mold Preparation

When the materials for the actuators were cut to their final dimensions, they were assembled and placed on the aluminum curing mold after it had been prepared. The mold was simply a flat, polished aluminum plate. It was found that if a plate was placed on the actuators during curing, as is standard for curing typical composite panels, uneven pressure was applied and the PZT plates tended to crack (Hopkinson, 2002). To prepare the mold for actuator curing it was first cleaned by polishing it with fine grit sandpaper. This step removed any surface asperities or epoxy from previous curing cycles. After polishing, an AIRTECH AT-200Y sealant tape was laid around the edges of the mold to seal the vacuum bag. In the middle of the plate AIRTECH Release-All #19 release agent was painted onto the surface. This release agent ensured the actuator did not bond to the

surface of the mold during curing. The assembled actuators were then placed on the prepared mold and covered with a release film. This film acted similarly to the release agent painted onto the mold. A few layers of bleeder cloth were placed around the actuators, but not touching them. Bleeder cloth performed a dual purpose; it allowed a vacuum to be pulled throughout the entire vacuum bag while simultaneously absorbing extra composite resin that leaked from the actuators during curing. A plastic vacuum bag was placed over the entire configuration and a tight seal was ensured around the edges so no air was allowed to enter. After being placed into the MAC, the vacuum connection was made and the top and bottom plates were secured. The entire structure was sealed by tightening the 16 tie rods. The whole unit was then inserted into the oven and the exterior pressure and vacuum connections made. A picture of the MAC inserted into the oven can be seen in Figure 3.9.

Figure 3.9. MAC inserted into oven.

3.3.2 Curing Cycle

The target cure cycle that was used with the miniature autoclave is plotted in Figure 3.10. The actuators were cured for one hour at 177 ^{o}C (350 ^{o}F) and 2.4 bars (35 psi) as recommended by the composite manufacturer. This cure cycle differs from the cure cycle used in the full scale autoclave because of the time it took to bring the inside of the MAC up to the proper curing temperature. The time that it took for the steel and aluminum of the MAC to reach full temperature caused a lag in the inside temperature of the box both during the heating and cooling portions of the curing cycle. To determine the extent of this delay the temperatures were measured with thermocouples both inside and outside of the MAC during a temperature ramp up cycle. The measurements from the thermocouples were read with a multimeter and compared to one another. The time for the inside temperature to reach the same temperature as the exterior temperature was determined by comparing the thermocouple readings with the temperature displayed by the oven. When the thermocouples had equal values, and the oven was at 177^{o}C, equilibrium between the inside and outside of the oven was assumed. The temperature inside the MAC took one and a half hours to reach equilibrium with the exterior oven temperature. In addition, the vacuum and pressure were not automated and therefore did not ramp up with the temperature, as in the larger automated autoclave.

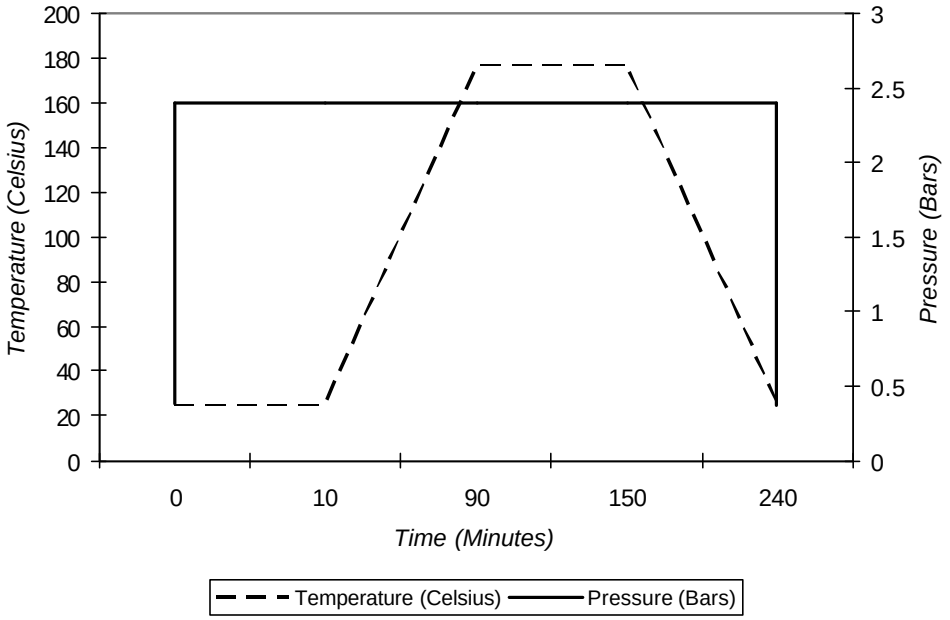

Figure 3.10. Target temperature and pressure variations during curing cycle.

3.3.3 Post Curing Processing

When the actuators had been removed from the cooled oven they required minimal preparation before testing. During curing, excess resin leaked from the pre-impregnated composite and soaked into the bleeder cloth. The small amount of this resin that attached itself to the edge of the actuator was sanded off. There was also resin on the top surface of the electrodes that was removed before wire leads were attached. The actuators came from the oven almost the exact size that they were used; therefore no cutting was required to bring them to their final size.

In addition, there was no repoling of the PZT material required after curing since the curing temperature of the Kevlar 49/epoxy prepreg composite is substantially below the Curie point of the PZT material. The Curie point specified by the manufacturer for 3195HD is 350^{o}C, which is almost twice the curing temperature required for the composite material.

CHAPTER 4

ACTUATOR CHARACTERIZATION AND MODELING

4.1 Background

The initial radius of curvature of the actuators being produced is an important design parameter. It is difficult to measure the radius of curvature directly and much easier to measure the dome height of the actuator. The dome height is the height difference between the bottom of the actuator and a flat, level area it is placed upon. A schematic is shown in Figure 4.1.

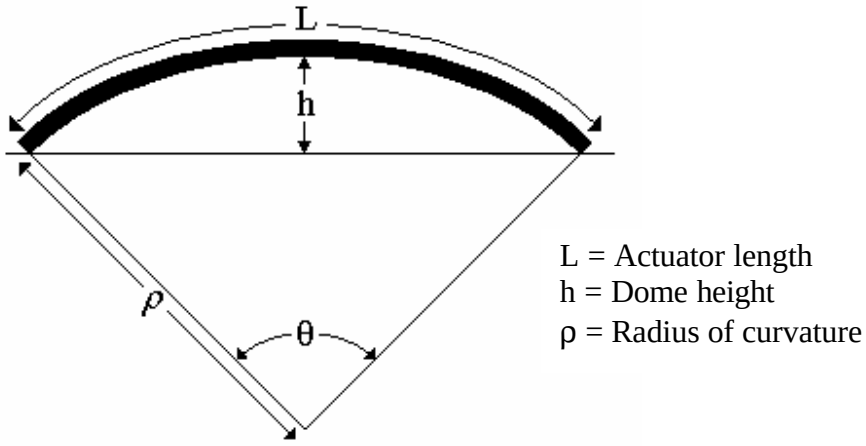

Figure 4.1. Actuator schematic.

4.1.1 Calculation of Curvature

The dome height, *h*, can be found using the geometry of the actuator in Figure 4.1. Equation (4.1) gives the relationship between the radius of curvature, r, the angle that the actuator sweeps through, q, and the dome height.

$$\cos\left(\frac{q}{2}\right) = \frac{r-h}{r} \tag{4.1}$$

Equation (4.2) gives the relationship between q, the arc length which subtends it, L, and the radius of curvature, r.

$$L = r \times q \tag{4.2}$$

Combining Equations (4.1) and (4.2) and solving for h yields Equation (4.3).

$$h = r\left[1 - \cos\left(\frac{L}{2r}\right)\right] \tag{4.3}$$

Equation (4.3) is a relationship that allows the radius of curvature to be calculated from the dome height measurements.

The dome height and radius of curvature can also be found from the strains on the top and bottom of the actuator. Figure 4.2 contains a schematic of an actuator showing the strains on the top and bottom surfaces.

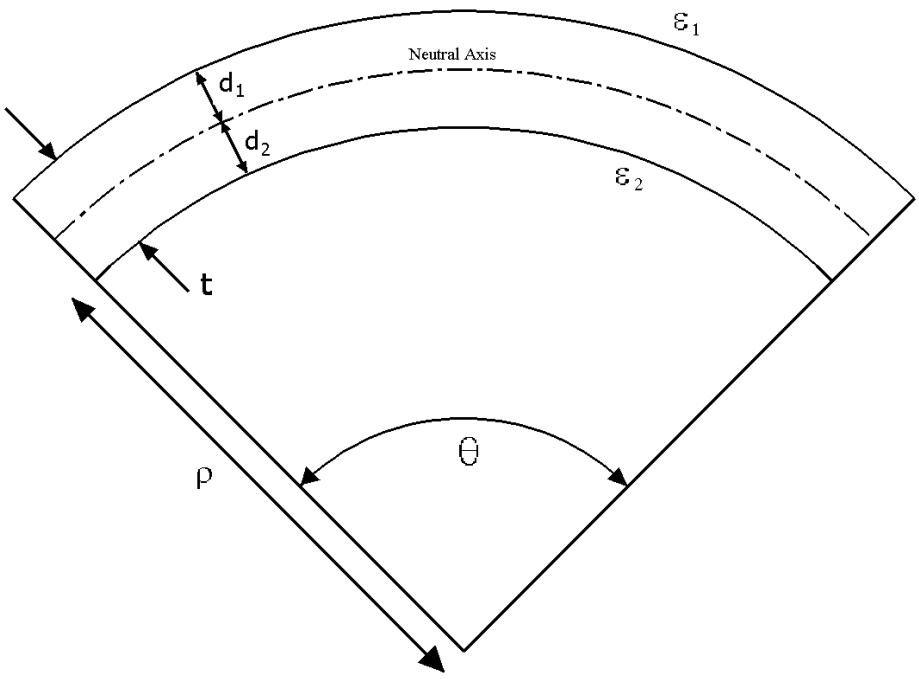

Figure 4.2. Schematic of actuator with associated strains on top and bottom surfaces.

The strain on the top surface of the actuator, e_1, can be related to the radius of curvature and the distance from the neutral axis to the outer most fiber on the top surface by the relationship in Equation (4.4).

$$e_1 = d_1 / r \tag{4.4}$$

Additionally the strain on the bottom surface of the actuator, e_2, can be related to the radius of curvature, and the distance from the neutral axis to the outer most fiber on the bottom surface by the relationship in Equation (4.5). The negative sign is used to denote a compressive strain.

$$e_2 = - d_2 / r \tag{4.5}$$

The overall thickness, t, is the sum of the thickness above the neutral axis, d_1, and the thickness below the neutral axis, d_2, is shown in Equation (4.6).

$$t = d_1 + d_2 \tag{4.6}$$

Combining Equations (4.4), (4.5), and (4.6) gives Equation (4.7) for the radius of curvature.

$$r = \frac{t}{e_1 - e_2} \tag{4.7}$$

This can be combined with Equation (4.3) to obtain Equation (4.8) for the actuator dome height.

$$h = \left[\frac{t}{e_1 - e_2}\right]\left[1 - \cos\left(\frac{L(e_1 - e_2)}{2t}\right)\right] \tag{4.8}$$

4.1.2 Error Sources

There are errors associated with the idealizations used in this analysis. It is assumed that the properties are uniform throughout the entire length, width, and thickness of each ply and that the layup is uniform. This is not true for any of the plies, including

the PZT plate. The PZT plate does not fully extend to the edges of the laminate. This non-uniform layup causes the ends of the composite actuators to have more curvature than the center section. Figure 4.3 illustrates the increased curvature due to overhanging composite material. The amount of Kevlar 49/epoxy material allowed to overhang the edges of the PZT plate was minimized, however; some amount of overhanging material was necessary to ensure that the PZT plate was electrically insulated by composite material.

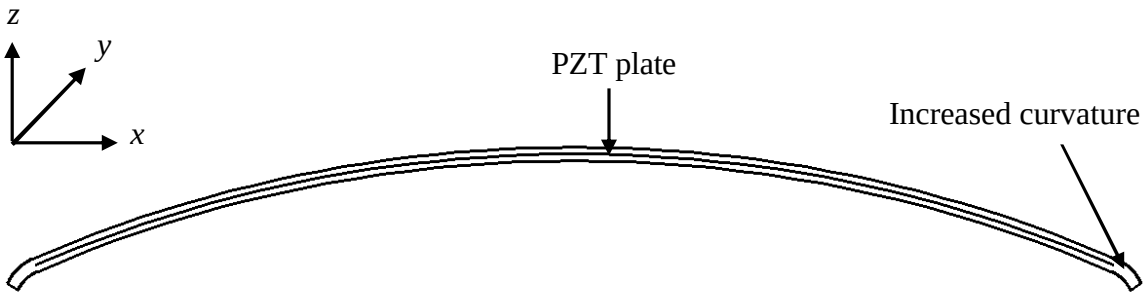

Figure 4.3. Increased curvature due to overhanging composite material.

An additional source of error is introduced by the hysteresis seen in the actuators due to domain wall motion in the PZT material. Figure 4.4 shows a typical hysteresis loop for an ECLIPSE actuator. As electric field is increased the actuator displaces as shown by the bottom line of the hysteresis loop. When the electric field on the actuator begins to decrease, the line on the top of the hysteresis loop is followed. In Figure 4.4, two hysteresis loops are shown for the same actuator tested at two different maximum electric field levels. The non-linearity of the PZT material causes difficulty in accurately measuring the slope of each loop. As can be seen from the straight lines drawn from the end points of each loop on Figure 4.4, the slope of the loops are different. The slope of the larger electric field loop is lower because of the effect of saturation of the PZT at

higher field levels. This can cause a problem in comparison of the change in displacement for measurements at two different electric field levels. However, for this study the only electric field level used to characterize and test actuators is 2 MV/m. For this reason the slopes can be directly compared between actuators and will be defined as the slope of the line created by the two extreme points of the hysteresis loop.

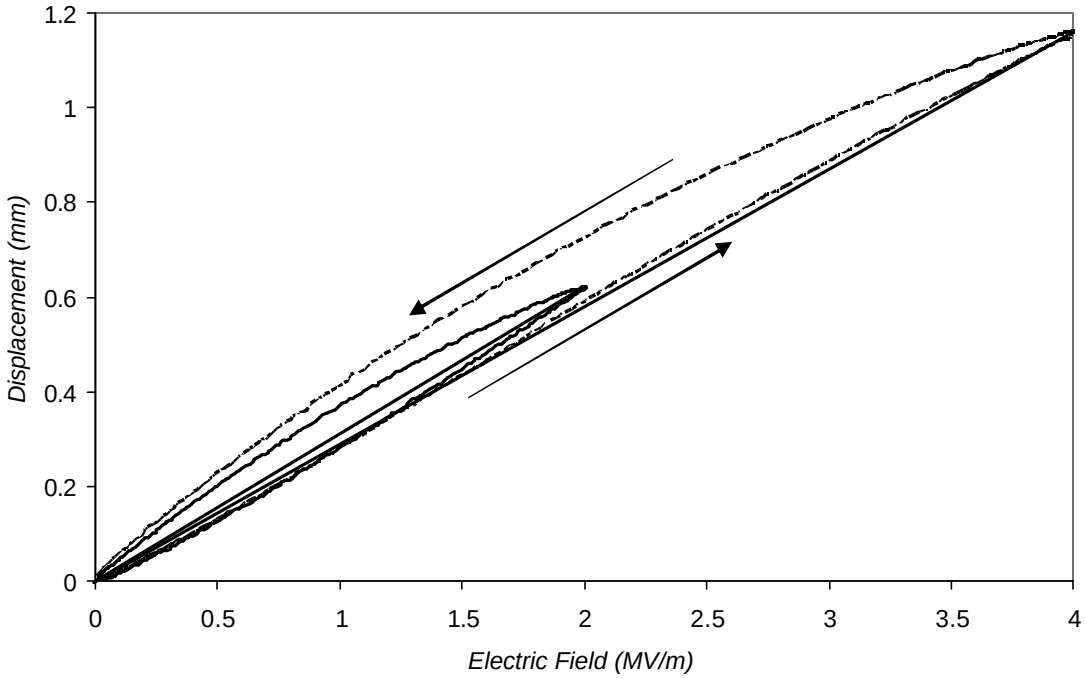

Figure 4.4. Typical hysteresis loops for the same actuator tested at different electric field levels.

4.2 Experimental Arrangement

To measure the change in dome height, a Schaevitz 005 MHR linear variable differential transducer (LVDT) with a 0.038 mm resolution was used. The LVDT is made up of a primary and secondary coil with an air core. These coils are located inside of a protective metal casing. A rod with an attached magnetic core moves within the air core and the amplitude of the resultant voltage is proportional to the rod position, while

the phase change indicates direction of movement from a reference zero position. The main advantage of the LVDT over other types of displacement measurement devices is the high degree of accuracy and repeatability. Additionally, there is also no physical contact across the sensing element so there is no wear in the sensing element. The LVDT was connected to a Schaevitz ATA 2001 LVDT signal conditioner and the output of the signal conditioner was recorded using a personal computer with a LabView™ data acquisition card. A schematic of the LVDT setup is shown in Figure 4.5.

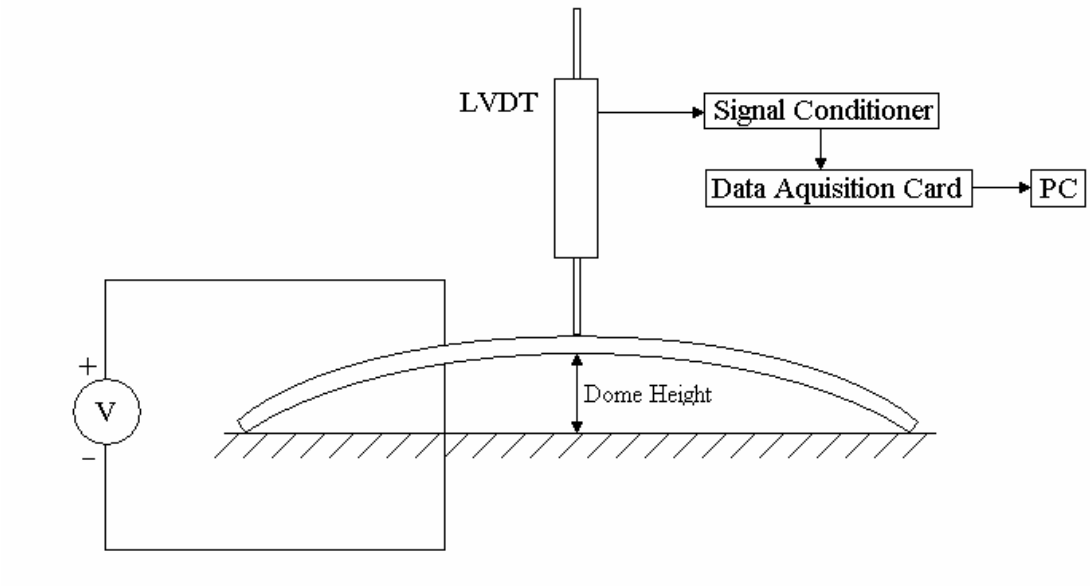

Figure 4.5. LVDT test setup

A small mark was made on the surface of the actuator to ensure that the tip of the LVDT was placed in the same location for successive measurements. The unevenness of the composite surface due to fiber bunching caused differences in measurements of initial dome height. These differences were on the order of $^{+}$/- 0.1mm depending on the level of fiber bunching in the area of measurement. The bottom side of the actuator remained

flat because it was in contact with the flat mold surface during curing. The surface of the actuator could be smoothed by adding a small amount of additional epoxy, or paint to create a more uniform measurement area. This was not done during the tests performed. Figure 4.6 illustrates the measuring differences due to fiber bunching.

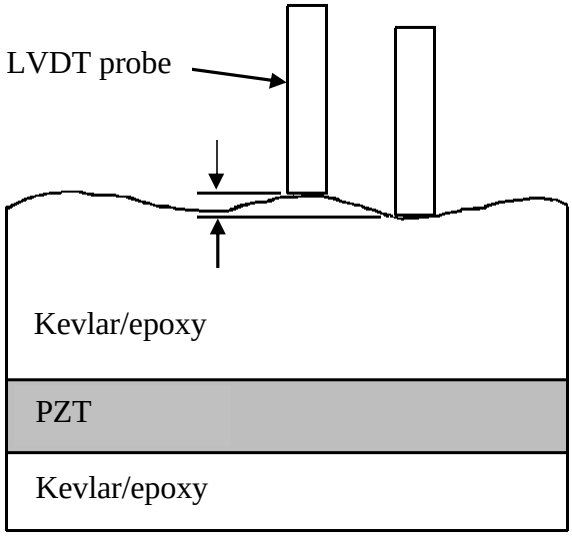

Figure 4.6. Measuring difference due to surface irregularities.

4.3 Classical Lamination Theory

Classical lamination theory was used to model the linear elastic response of thin laminated structures. CLT was also useful in calculating the stresses and strains in each lamina while the structure was subjected to external moments and in-plane loads and was also used to predict the initial as well as the change in radius of curvature of the entire structure. The calculated stress in each ply was used to ensure that the brittle PZT plate remained in compression throughout an electric field cycle. Additionally, the calculated strain was used to locate the neutral axis. The following derivations are similar to the classical work by Pister and Dong and Reissner and Stavsky.

4.3.1 Kirchhoff Hypothesis and Assumptions

It is assumed in classical lamination theory that each layer is in a state of plane stress and that the deformation of the actuator follows the Kirchhoff hypothesis for plates after cooling from the curing temperature. The Kirchhoff hypothesis makes simplifying assumptions for deformation of plates. These assumptions to not restrict a plate to a flat laminate, and can be used for curved shapes such as the ECLIPSE actuator. The following are the assumptions used in CLT (Mallick 1993, Herakovich 1998, Love 1927, Jones 1999):

i. The laminate layers are perfectly bonded, which implies that the laminate acts as a single layer. The bonds are assumed to be infinitesimally thin and non-shear-deformable.

ii. For thin laminates, lines originally straight and perpendicular to the middle surface of the laminate remain straight and perpendicular even after deformation.

iii. The lines perpendicular to the middle surface have constant length. This implies that strain through the thickness is zero ($e_{zz} = 0$).

iv. In-plane displacements are linear functions of the thickness; therefore the shear strains g_{xz} and g_{yz} are negligible.

v. The laminate is thin and wide resulting in plane stress (width, length>> thickness).

vi. All lamina are macroscopically homogeneous and behave linearly elastic.

vii. Individual ply properties can be isotropic, orthotropic, or transversely isotropic.

4.3.2 Laminate Strains

The strains throughout the laminate are linearly related to the distance from the midplane. This is a consequence of the Kirchhoff assumptions. The derivation of the strain equations is shown in Appendix A Figure 4.7 shows a cross-section of a laminate with an arbitrary number of *n* plies. The height from the bottom of the actuator is labeled as *z(n)*, with *z(0)* representing the bottom of the laminate. The total thickness of the stack is *t*. The X_1 and X_2 directions are in-plane and perpendicular to the X_3 direction, which is parallel to the poling direction of the piezoelectric material.

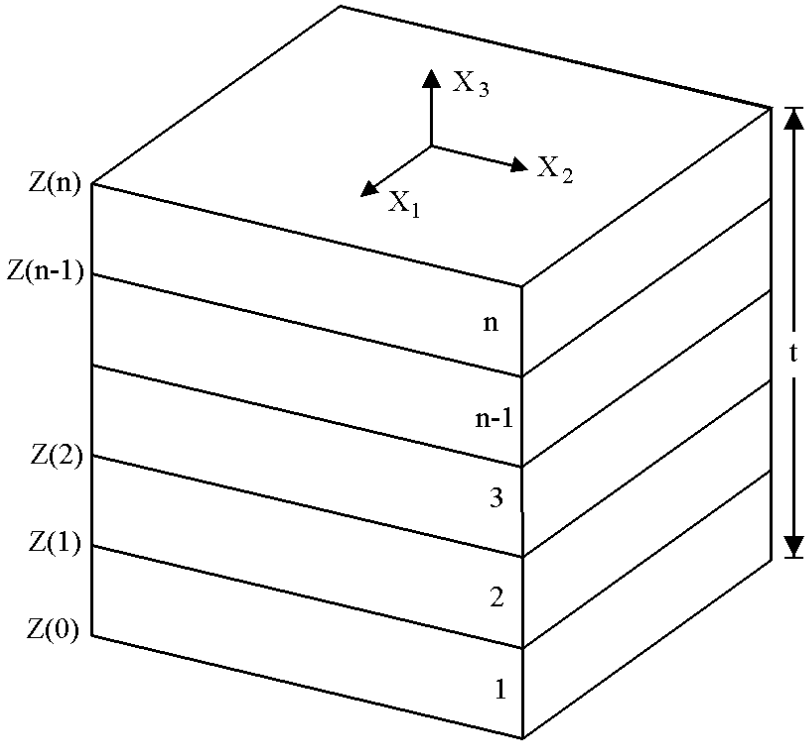

Figure 4.7. Cross-section of composite material

In the following equations the total strain, e, is related to the midplane normal strains, e^o, the bending curvatures in the laminate, k, and the distance from the mid-plane in the thickness direction X_3, z.

$$e_{xx} = e_{xx}^{\,o} + z \cdot k_{xx} \tag{4.9}$$

$$e_{yy} = e_{yy}^{\,o} + z \cdot k_{yy} \tag{4.10}$$

Similarly, in Equation (4.11), the total shear strain, g_{xy}, is related to the midplane shear strain, g^o, the twisting curvature in the laminate, k_{xy}, and the distance from the midplane in the thickness direction X_3, z.

$$g_{xy} = g_{xy}^{\,o} + z \cdot k_{xy} \tag{4.11}$$

Additionally, the total strain is also the summation of the mechanical strain, e^{σ}, the thermal strain, e^{T}, and the piezoelectric strain, e^{P}, as shown in Equation (4.12).

$$\{e\} = \{e^{s}\} + \{e^{T}\} + \{e^{P}\} \tag{4.12}$$

The stress-strain relation for the both the composite material and piezoelectric plate is

$$\{e\} = [s]\{s\} + \Delta T\{\bar{a}\} + \mathrm{E}\{d\}. \tag{4.13}$$

The mechanical strain is the product of the compliance matrix, $[s]$, and the stress vector, $\{s\}$. The thermal component of the strain is due to the reduction in temperature from the cure temperature to room temperature, DT, and the coefficients of thermal expansion, $\{\bar{a}\}$. The piezoelectric portion of the strain is due to the electric field, E, and the piezoelectric strain coefficient, $\{d\}$.

The stress at any point through the thickness of the actuator can be found by combining Equations (4.9) - (4.13) and rearranging terms. The subscript k denotes the layer of the laminate.

$$\{s\} = \left[\overline{Q}\right]_k \left(\{e^\circ\} + z\{k\} - \Delta T\{\overline{a}\} - \mathrm{E}\{d\}\right) \tag{4.14}$$

where the $[\overline{Q}]$ are the reduced stiffnesses for a plane stress state. Plane stress is assumed because the thickness of the actuators is much smaller then the length and the width.

4.3.3 Reduced Stiffness Matrix

The general stress-strain relationship for all material symmetries is seen in Equation (4.15).

$$e_i = S_{ij} \cdot s_j \qquad i, j = 1, \ldots, 6 \tag{4.15}$$

The expansion of Equation (4.15) for the orthotropic case with constant electric field, where the 36 independent coefficients are reduced to 9 independent coefficients due to material symmetry, is shown in Equation (4.16).

$$\begin{Bmatrix} e_{11} \\ e_{22} \\ e_{33} \\ g_{23} \\ g_{31} \\ g_{12} \end{Bmatrix} = \begin{bmatrix} S_{11} & S_{12} & S_{13} & 0 & 0 & 0 \\ S_{12} & S_{22} & S_{23} & 0 & 0 & 0 \\ S_{13} & S_{23} & S_{33} & 0 & 0 & 0 \\ 0 & 0 & 0 & S_{44} & 0 & 0 \\ 0 & 0 & 0 & 0 & S_{55} & 0 \\ 0 & 0 & 0 & 0 & 0 & S_{66} \end{bmatrix} \begin{Bmatrix} s_{11} \\ s_{22} \\ s_{33} \\ t_{23} \\ t_{31} \\ t_{12} \end{Bmatrix} \tag{4.16}$$

Equation (4.16) can be further reduced because all out-of-plane stresses (s_{33}, t_{23}, and t_{31}) are assumed equal to zero in the plane stress assumption. For orthotropic materials the out-of-plane strains take the following form:

$$\begin{aligned} g_{23} &= s_{44} t_{23} = 0 \\ g_{13} &= s_{55} t_{13} = 0 \\ e_{33} &= s_{13} s_{11} + s_{23} s_{22} \end{aligned} \tag{4.17}$$

The stress-strain relationship can be reduced further to only the in-plane components as shown in Equation (4.18).

$$\begin{Bmatrix} e_{11} \\ e_{22} \\ g_{12} \end{Bmatrix} = \begin{bmatrix} s_{11} & s_{12} & 0 \\ s_{12} & s_{22} & 0 \\ 0 & 0 & s_{66} \end{bmatrix} \begin{Bmatrix} s_{11} \\ s_{22} \\ t_{12} \end{Bmatrix} \tag{4.18}$$

Solving for the stress vector by inverting the reduced compliance matrix yields the stress-strain relations in Equation (4.19).

$$\begin{Bmatrix} s_{11} \\ s_{22} \\ t_{12} \end{Bmatrix} = \begin{bmatrix} Q_{11} & Q_{12} & 0 \\ Q_{12} & Q_{22} & 0 \\ 0 & 0 & Q_{66} \end{bmatrix} \begin{Bmatrix} e_{11} \\ e_{22} \\ g_{12} \end{Bmatrix} \tag{4.19}$$

where Q_{ij} are the reduced stiffnesses for a state of plane stress in the 1-2 plane.

The components of the reduced stiffness matrix can be defined in terms of four independent constants: the Young's moduli, E_1 and E_2, the shear modulus, G_{12}, and the Poisson's ratio, n_{12}.

$$\begin{aligned} Q_{11} &= \frac{E_{11}}{1-n_{12}n_{21}} \\ Q_{22} &= \frac{E_{22}}{1-n_{12}n_{21}} \\ Q_{12} &= \frac{n_{21}E_{11}}{1-n_{12}n_{21}} = \frac{n_{12}E_{22}}{1-n_{12}n_{21}} \\ Q_{66} &= G_{12} \end{aligned} \tag{4.20}$$

There are only four independent terms needed due to the reciprocal relationship;

$$\frac{u_{12}}{E_{11}} = \frac{u_{21}}{E_{22}} \tag{4.21}$$

4.3.4 Stress-Strain Relations for Arbitrary Composite Layer Orientation

The stresses and strains that are defined in the principal material coordinates for an orthotropic composite material do not necessarily coincide with the coordinate system that is the simplest geometrically. In the case of ECLIPSE actuators, the unidirectional fibers in one layer may be orthogonal to the fibers of another layer. Transforming the material properties of the composite from one coordinate system to another is important. Figure 4.8 shows a picture of a positive rotation from principal material axes to the *x-y* axes through *q* degrees.

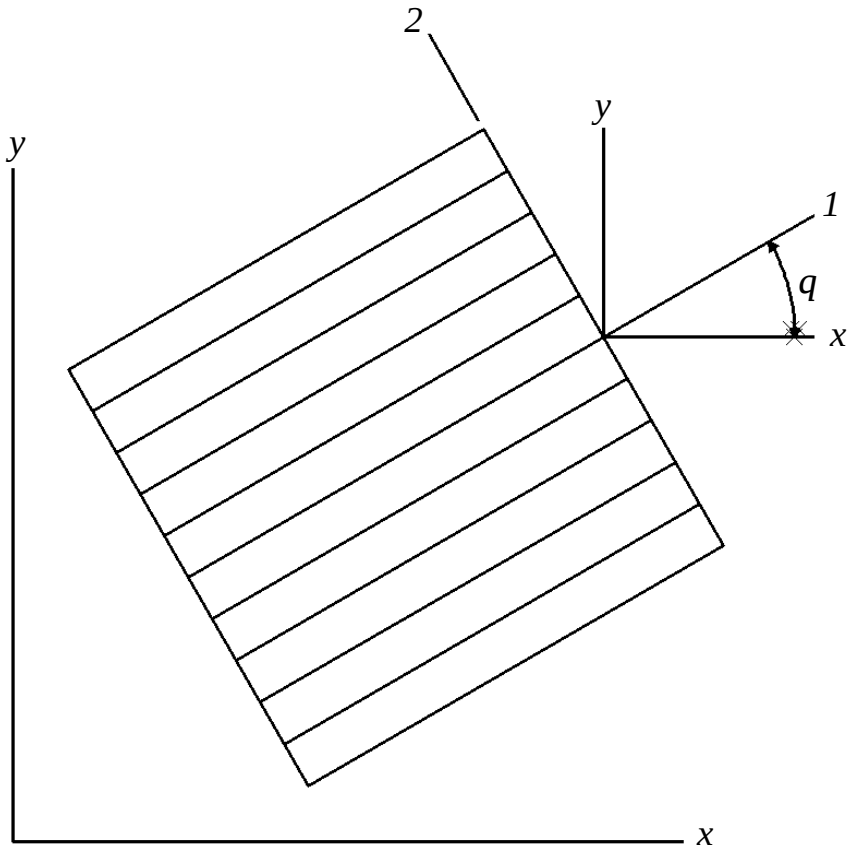

Figure 4.8. Positive rotation to principal material coordinates from arbitrary *x-y* axes.

From elementary mechanics of materials the transformation equation is defined as:

$$[T] = \begin{bmatrix} \cos^2(q) & \sin^2(q) & 2\sin(q)\cos(q) \\ \sin^2(q) & \cos^2(q) & -2\sin(q)\cos(q) \\ -\sin(q)\cos(q) & \sin(q)\cos(q) & \cos^2(q) - \sin^2(q) \end{bmatrix} \tag{4.22}$$

Utilizing this transformation matrix, the reduced stiffness matrix, Q_{ij}, can be transformed from one coordinate system to another. This allows for the calculation of stresses and strains for an arbitrary layup. Equation (4.23) shows the transformation of the reduced stiffness matrix into the transformed reduced stiffness matrix for an arbitrary transformation angle.

$$\begin{bmatrix} \overline{Q}_{11} & \overline{Q}_{12} & \overline{Q}_{16} \\ \overline{Q}_{12} & \overline{Q}_{22} & \overline{Q}_{26} \\ \overline{Q}_{16} & \overline{Q}_{26} & \overline{Q}_{66} \end{bmatrix} = [T]^{-1} \begin{bmatrix} Q_{11} & Q_{12} & 0 \\ Q_{12} & Q_{22} & 0 \\ 0 & 0 & Q_{66} \end{bmatrix} [T]^{-T} \tag{4.23}$$

Similarly, the coefficients of thermal expansion can be transformed from the principal material coordinates to the geometrically simplest coordinate system.

$$\begin{bmatrix} \overline{a}_{11} \\ \overline{a}_{22} \\ \overline{a}_{12} \end{bmatrix} = [T]^{-T} \begin{bmatrix} a_{11} \\ a_{22} \\ 0 \end{bmatrix} \tag{4.24}$$

4.3.5 Stiffness Matrices

The transformed reduced stiffness matrix is used to find the three stiffness matrices [A], [B], and [D]. The stiffness matrices are functions of the elastic properties of each layer and the position in relation to the midplane of the composite structure. Each stiffness matrix is related to a certain material behavior. The [A] matrix is the extensional stiffnesses, the [B] matrix is the bending-extension coupling stiffnesses, and

the [D] matrix is the bending stiffnesses. The stiffness matrices are shown in Equations (4.25 - 4.27)

$$[A] = \sum_{k=1}^{n} [\overline{Q}]_k (z_k - z_{k-1}) \tag{4.25}$$

$$[B] = \frac{1}{2} \sum_{k=1}^{n} [\overline{Q}]_k (z_k^2 - z_{k-1}^2) \tag{4.26}$$

$$[D] = \frac{1}{3} \sum_{k=1}^{n} [\overline{Q}]_k (z_k^3 - z_{k-1}^3) \tag{4.27}$$

4.3.6 Laminate Forces and Moments

The resultant forces are obtained by integrating the stresses found in each layer of the composite material through the thickness of the laminate as shown in Equation (4.28), where *H* is the total thickness of the laminate.

$$\{N\} = \int_{-H/2}^{H/2} \{s\} dz \tag{4.28}$$

Similarly, the resultant moments are obtained by multiplying the stresses by the distance from the midplane of the laminate, *z*, which acts as a moment arm, and integrating over the laminate thickness, as defined by Equation (4.29).

$$\{M\} = \int_{-H/2}^{H/2} \{s\} z \, dz \tag{4.29}$$

The total force on the actuator is due to mechanical loading, thermal loading, and piezoelectric coupling. For this model, the applied mechanical loads are taken to be zero since no external loading will be applied during characterization.

$$\{N\} = \{N^s\} + \{N^T\} + \{N^P\} \tag{4.30}$$

Similarly, the total moment on the actuator is a combination of the mechanical moments, thermal moments, and the moments due to the piezoelectric coupling as shown in Equation (4.31). The mechanical moments are also taken to be zero because no external moments were applied during characterization.

$$\{M\} = \{M^{s}\} + \{M^{T}\} + \{M^{P}\} \tag{4.31}$$

The normal force and moment caused by the thermal expansion are shown in Equation (4.32).

$$\begin{aligned} \{N^{T}\} &= \Delta T \sum_{k=1}^{n} [\overline{Q}]_k \{\overline{a}\}_k (z_k - z_{k-1}) \\ \{M^{T}\} &= \frac{1}{2} \Delta T \sum_{k=1}^{n} [\overline{Q}]_k \{\overline{a}\}_k (z_k^2 - z_{k-1}^2) \end{aligned} \tag{4.32}$$

where ΔT is the difference between the room temperature and the cure temperature, $\overline{a}$ are the coefficients of thermal expansion, transformed to account for the orientation of each ply, and n is the number of plies in the laminate.

Forces and moments due to piezoelectric coupling are given in Equation (4.33).

$$\begin{aligned} \{N^{P}\} &= E_3 \sum_{k=1}^{n} [\overline{Q}]_k \{d\}_k (z_k - z_{k-1}) \\ \{M^{P}\} &= \frac{1}{2} E_3 \sum_{k=1}^{n} [\overline{Q}]_k \{d\}_k (z_k^2 - z_{k-1}^2) \end{aligned} \tag{4.33}$$

where E is the electric field through the thickness of the actuator and d is the piezoelectric coefficient for the PZT material.

4.3.7 Calculation of the Midplane Strains and Curvatures

The normal and moment resultants are related to the midplane strains and curvatures through the stiffness matrices as shown in matrix notation in Equation (4.34).

$$\begin{Bmatrix} N \\ M \end{Bmatrix} = \begin{bmatrix} A & B \\ B & D \end{bmatrix} \begin{Bmatrix} e^o \\ k \end{Bmatrix} \tag{4.34}$$

Equation (4.27) is used to calculate the midplane strains and curvatures as the normal and moments resultants and A, B, and D are known. Substituting the midplane strains and curvatures back into the relationships shown, the stresses and strains, as well as the dome height of the actuator can be calculated.

4.3.8 CLT Computer Program

A Matlab™ computer program was created to predict actuator behavior by using classical lamination theory. This program allows the user to predict the actuator dome height and curvature, as well as the stress and strain distribution through the thickness of the actuator, from material properties and dimensions. Each layup is designed to ensure residual compression on the PZT plate and that the desired behavior, such as initial curvature or moment output, are sufficient.

The computer program is setup to be general and applicable to any laminate panel, not just ECLIPSE actuators. The user is first prompted to enter the actuator dimensions and operating conditions which include the number of layers, the actuator length, curing temperature, electric field, and position of the PZT plate in the stacking sequence. The material properties are then entered for each ply, starting from the bottom. The program then displays the dome height and figures that display the stress and strain through the thickness in the x and y directions. A flowchart for the computer

program is shown in Figure 4.9. This is an improvement over previous programs. Other programs used a number of subscripts which were specific to the number of plies in the actuator. For each layup with a different number of plies, a different program was needed. The new program is shorter and can be used for a layup with any

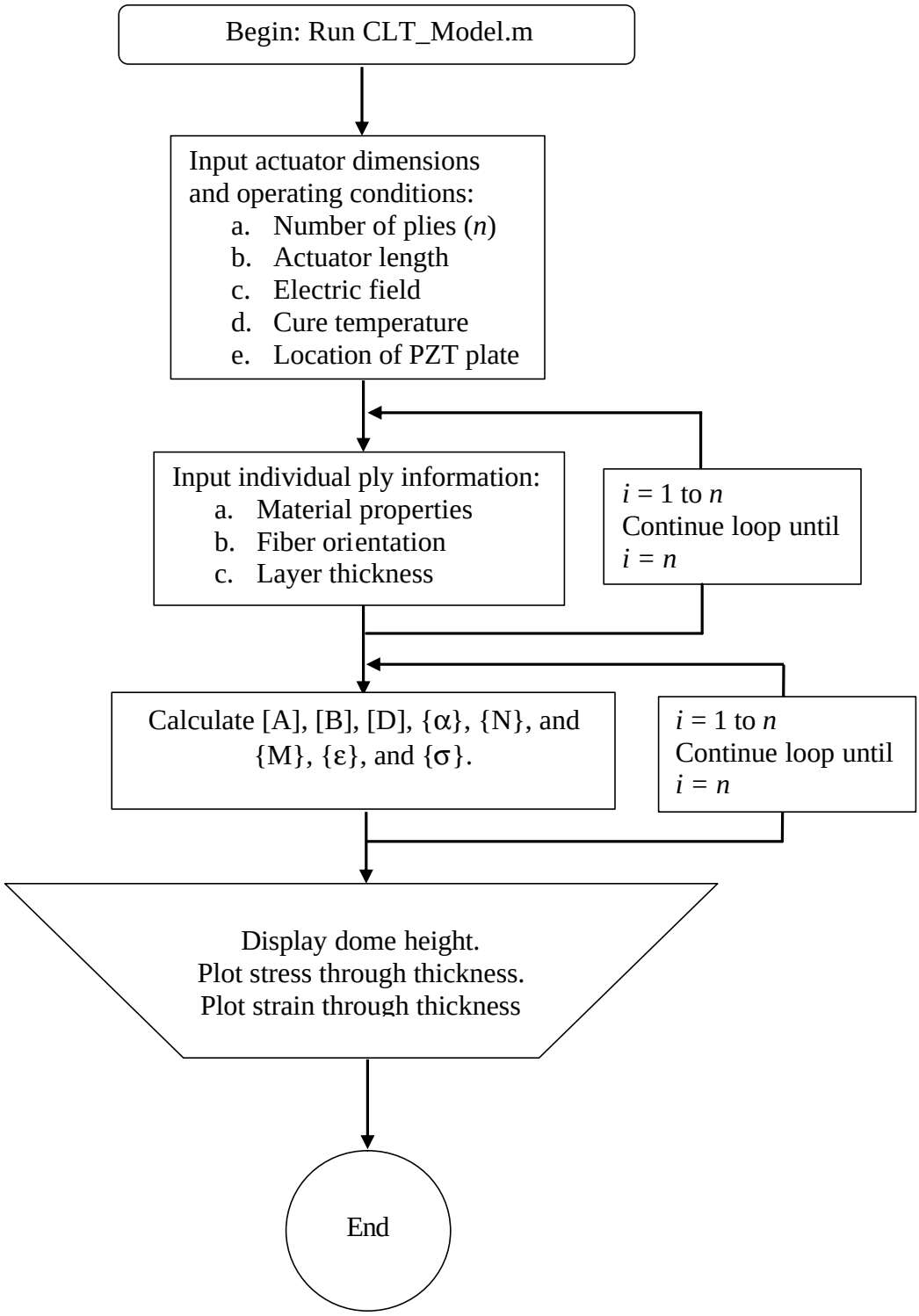

Figure 4.9. CLT computer program flowchart.

stacking order or number of layers. Individual ply orientations are also input by the user which allows for the design of actuators with any arbitrary fiber angle including twist coupling.

4.3.9 Comparison of Measured and Predicted Dome Heights

The initial dome height, due to thermal expansion, and the dome height displacement, in response to an electric field, are compared to the predicted values obtained by the CLT model. Five different specimens were compared. All had the same dimensions, but the stacking order of the layers varied. For each layup three actuators were tested. Table 4.3 contains the stacking sequence for the different specimens. Figures (4.10a-4.10e) show the displacement plot against the electric field for the measured data and the model predictions. The plots in Figures (4.10a-4.10e) show hysteresis loops, which are predominately due to the piezoelectric material behavior. The hysteresis loops for each actuator begins at zero electric field and zero displacement. There is an initial height due to thermal expansion, but this is not shown in these figures in order to illustrate the differences in the change of displacement for changes in the electric field and the hysteresis loops for each actuator. The electric field is increasing during the bottom portion of the hysteresis loop and decreasing during the top portion.

Table 4.1. Stacking sequence of tested actuators

Specimen	Ply 1	Ply 2	Ply 3	Ply 4	Ply 5	Ply 6	Ply 7	Ply 8
A,B,C	b	c	b	a	-	-	-	-
D,E,F	b	b	c	b	a	a	-	-
G,H,I	b	b	c	b	b	a	-	-
J,K,L	b	b	b	c	b	a	a	a
M,N,O	b	b	b	c	b	b	a	a

a. 0^o Unidirectional Kevlar 49/epoxy

b. 90^o Unidirectional Kevlar 49/epoxy

c. CTS 3195HD PZT

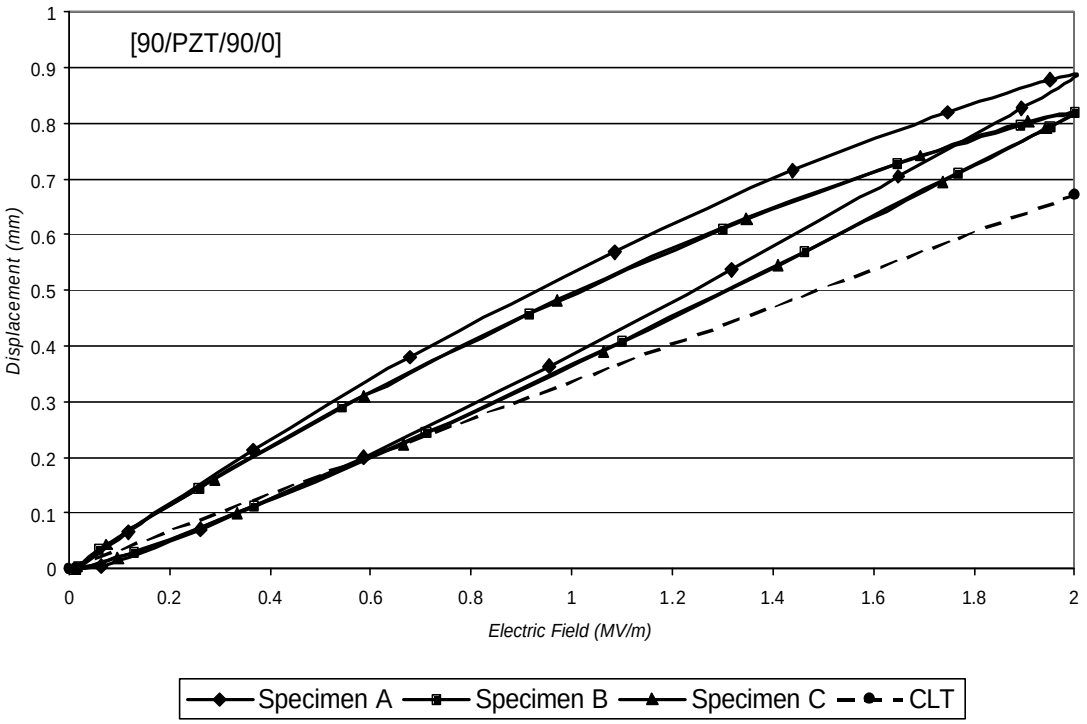

Figure 4.10a. Displacement vs. electric field for the LVDT measurements and CLT model

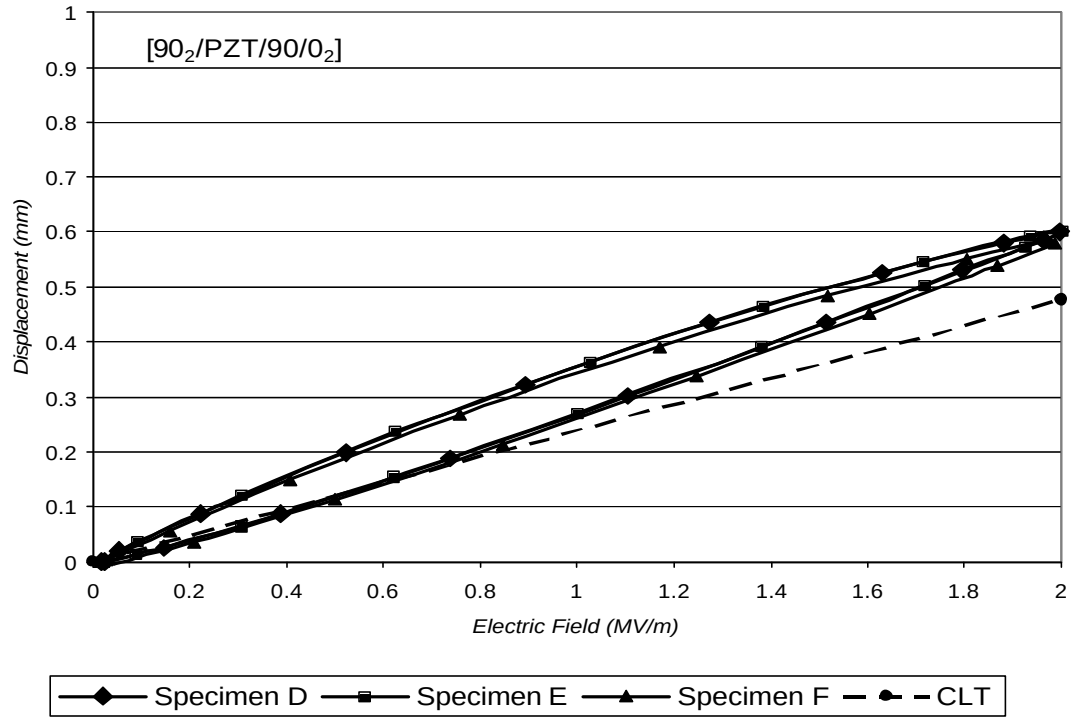

Figure 4.10b. Displacement vs. electric field for the LVDT measurements and CLT model

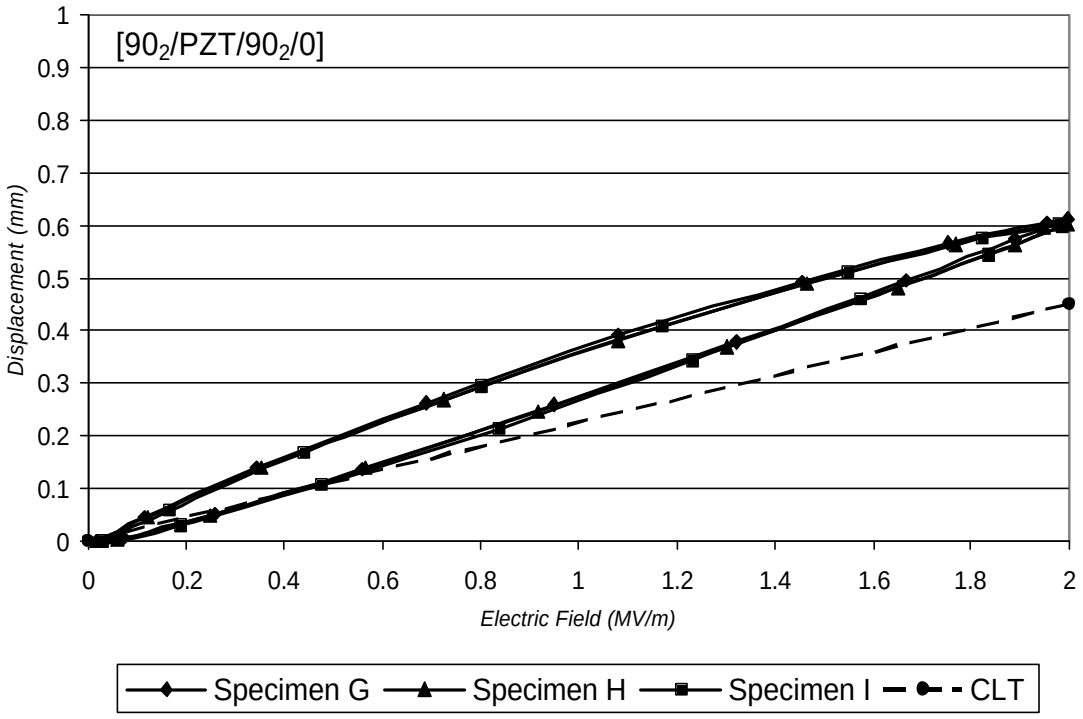

Figure 4.10c. Displacement vs. electric field for the LVDT measurements and CLT model

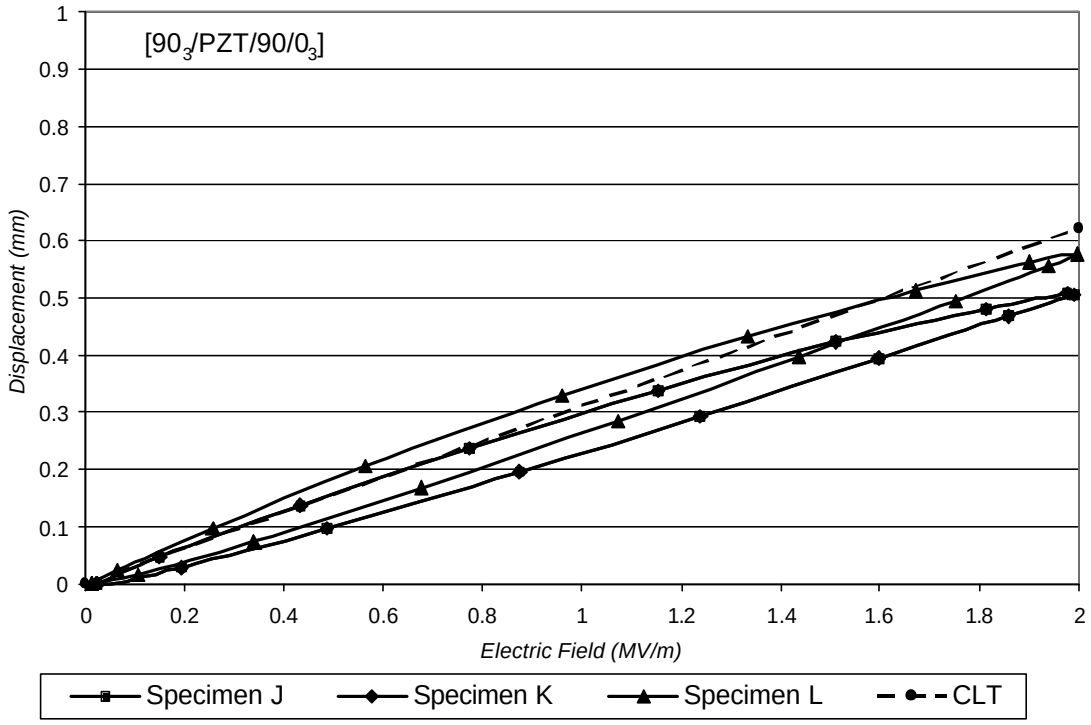

Figure 4.10d. Displacement vs. electric field for the LVDT measurements and CLT model

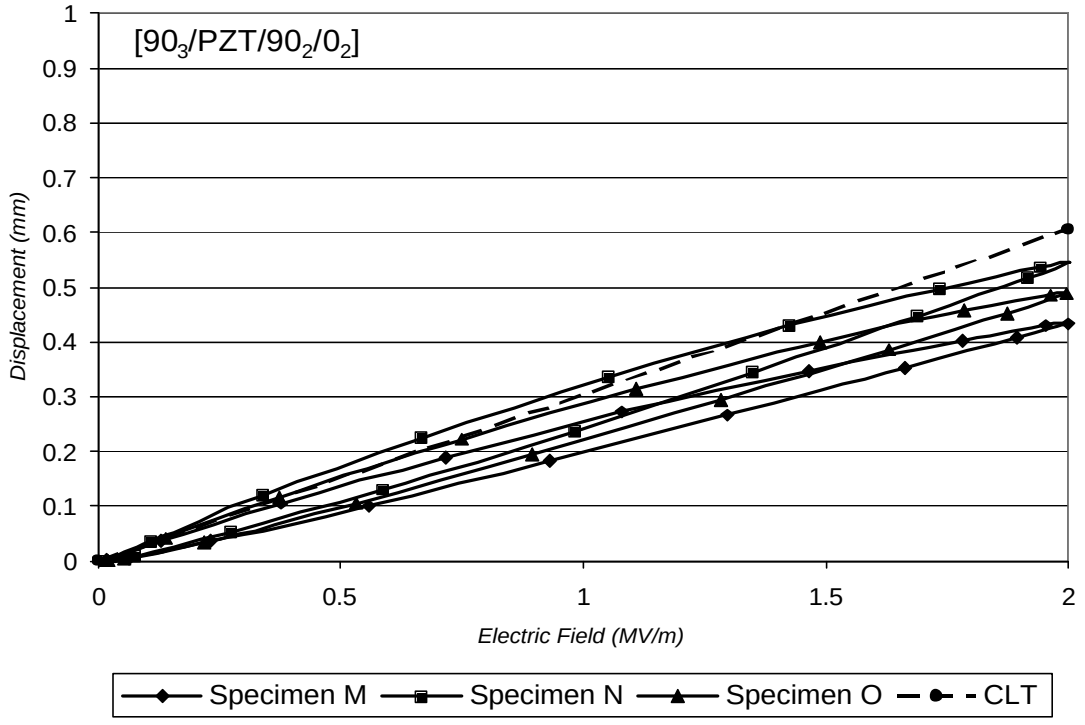

Figure 4.10e. Displacement vs. electric field for the LVDT measurements and CLT model

Figures 4.10a-4.10d show the repeatability of ECLIPSE actuators. The slope of the hysteresis loops in Figure 4.10e however varied from one another. This could have been due to manufacturer defects in the PZT or composite material. The initial actuator dome height predicted by the CLT model is compared to the measured results in Table 4.2 and the predicted slope of the actuator dome height displacement is compared to the measured values in Table 4.3. The hysteresis loop of the actuator was not considered when finding the slope of the measured actuators.

Table 4.2. Comparison of measured initial dome heights to CLT predictions.

	Actuator 1		Actuator 2		Actuator 3		
	Height (mm)	Diff	Height (mm)	Diff	Height (mm)	Diff	CLT Model
[90/PZT/90/0]	3.19926	8.71%	3.3481	13.76%	3.5769	21.54%	2.943
[90_2/PZT/90/0_2]	3.3988	2.42%	3.5606	7.29%	3.5718	7.63%	3.3186
[90_2/PZT/90_2/0]	3.0309	10.84%	3.0607	11.92%	3.0458	11.38%	2.7346
[90_3/PZT/90/0_3]	3.4785	3.23%	3.1715	-5.88%	2.9278	-13.11%	3.3696
[90_3/PZT/90_2/0_2]	3.59506	13.91%	3.27322	3.71%	3.43135	8.72%	3.1561

Table 4.3. Comparison of measured dome height displacement slopes to CLT predictions.

	Actuator 1		Actuator 2		Actuator 3		
	Slope (dh/dE)	Diff	Slope (dh/dE)	Diff	Slope (dh/dE)	Diff	CLT Model
[90/PZT/90/0]	0.44276	31.87%	0.4102	22.17%	0.4102	22.17%	0.33575
[90_2/PZT/90/0_2]	0.30045	25.74%	0.30045	25.74%	0.29208	22.23%	0.23895
[90_2/PZT/90_2/0]	0.30509	35.20%	0.30045	33.15%	0.301377	33.56%	0.22565
[90_3/PZT/90/0_3]	0.24463	-21.34%	0.2539	-18.36%	0.28835	-7.28%	0.311
[90_3/PZT/90_2/0_2]	0.2167	-28.59%	0.27161	-10.49%	0.244636	-19.38%	0.30345

The CLT model predicted the initial dome height, on average, within 9.6% of the actual measured values for every layup. The maximum difference between the model and the measured occurred for the [90/PZT/90/0] layup, which was 21.5%. The CLT model did not predict the slope of the dome height displacement with the same accuracy.

The model predicted the dome height differed from the measured values by an average of 23.8% for all of the layups.

The CLT model is a useful approximation for the response of the actuators, but has two notable limitations. First, it is limited to modeling linear behavior. The PZT is linear over a limited range because of a hysteresis in the response due to domain wall motion. Previous generations of ECLIPSE actuators used a softer PZT material with a higher d_{31} piezoelectric coupling factor that resulted in piezoelectric strain saturation at electric field values higher than 0.6 MV/m. For this case the model over-predicted the displacement response beyond that level. The ECLIPSE actuators used in this study utilized a less hysteretic material with a smaller d_{31} piezoelectric coupling factor resulting in improved linearity throughout the full range of applied electric fields. The slopes of the measured values and those of the model match closely for these actuators. The second limitation of classical lamination theory is the assumption that the properties are homogeneous throughout the entire length, width, and thickness of each ply; however, the PZT plate does not fully extend to the edges of the laminate. This non-uniform layup causes the ends of the composite actuators to have significantly more curvature than the center section. This explains the under-prediction of the initial dome height of the composite actuators which is evident in Figures 4.10a , 4.10b, 4.10c and 4.10e. However, in Figure 4.10d, the CLT model over-predicts the measured actuators. This is possibly due to the addition of 0^0 plies, which are stiff in bending, preventing the additional curvature at the edges. As the amount of Kevlar material extending past the edge of the PZT plate decreases; the model predictions come closer to the measured values. As the overhang increases the model under-predicts the initial curvature while it continues to

correctly predict the change in curvature. However, some amount of overhanging material is necessary to ensure that the PZT plate is electrically isolated by composite material.

4.3.10 Prediction of Stresses and Strains

This model is also useful for the prediction of the stresses and strains through the thickness of the actuator. Figures (4.11a-4.11e) show the stress and strain distribution of the actuators through their thickness in the X_1 and X_2 directions for the cases of no applied electric field and full electric field (2 MV/m). The figures illustrating the stress and strain in the X_1 direction show that there is a compressive stress on the PZT plate which is located below the neutral axis. Applying a positive electric field to the PZT plate will cause contraction, which makes the dome height of the actuator increase in addition to an increased tensile load on the PZT plate. The same 90^o plies that caused compression in the X_1 direction however become 0^o plies in the X_2 direction and cause an increase in the tensile load in the PZT plate. This effect was increased in layups when more 90^o plies were exchanged for 0^o plies above the PZT plate. There is a trade-off for substituting 0^o plies above the PZT plate for 90^o plies to increase the compressive stress on the PZT plate. The dome height and dome height displacement decrease due to increased rigidity added by plies with a 0^o orientation.

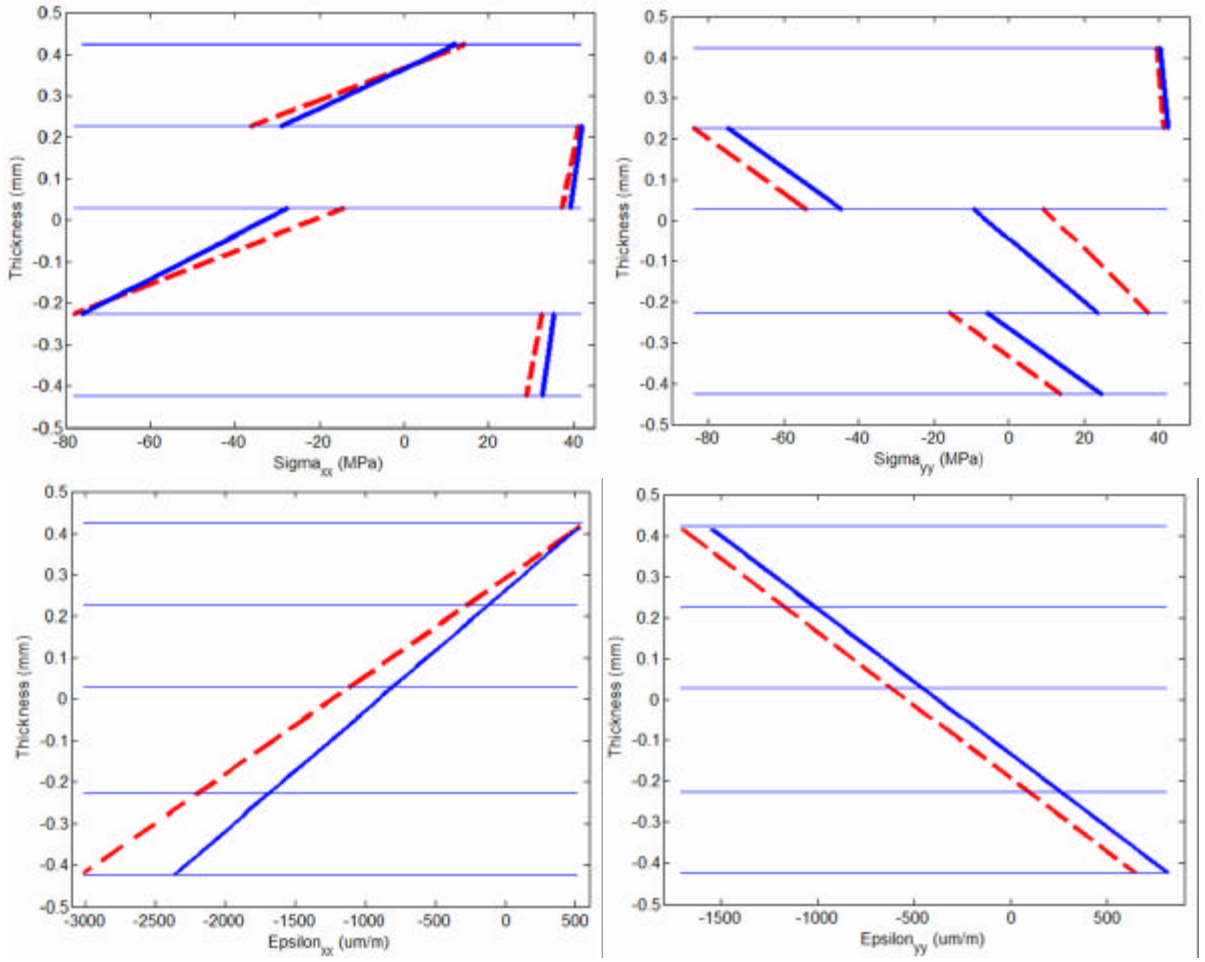

Figure 4.11a. Stress and strain distributions for zero electric field (solid) and full scale electric field (dashed) in the X_1 and X_2 directions for the [90/PZT/90/0] layup.

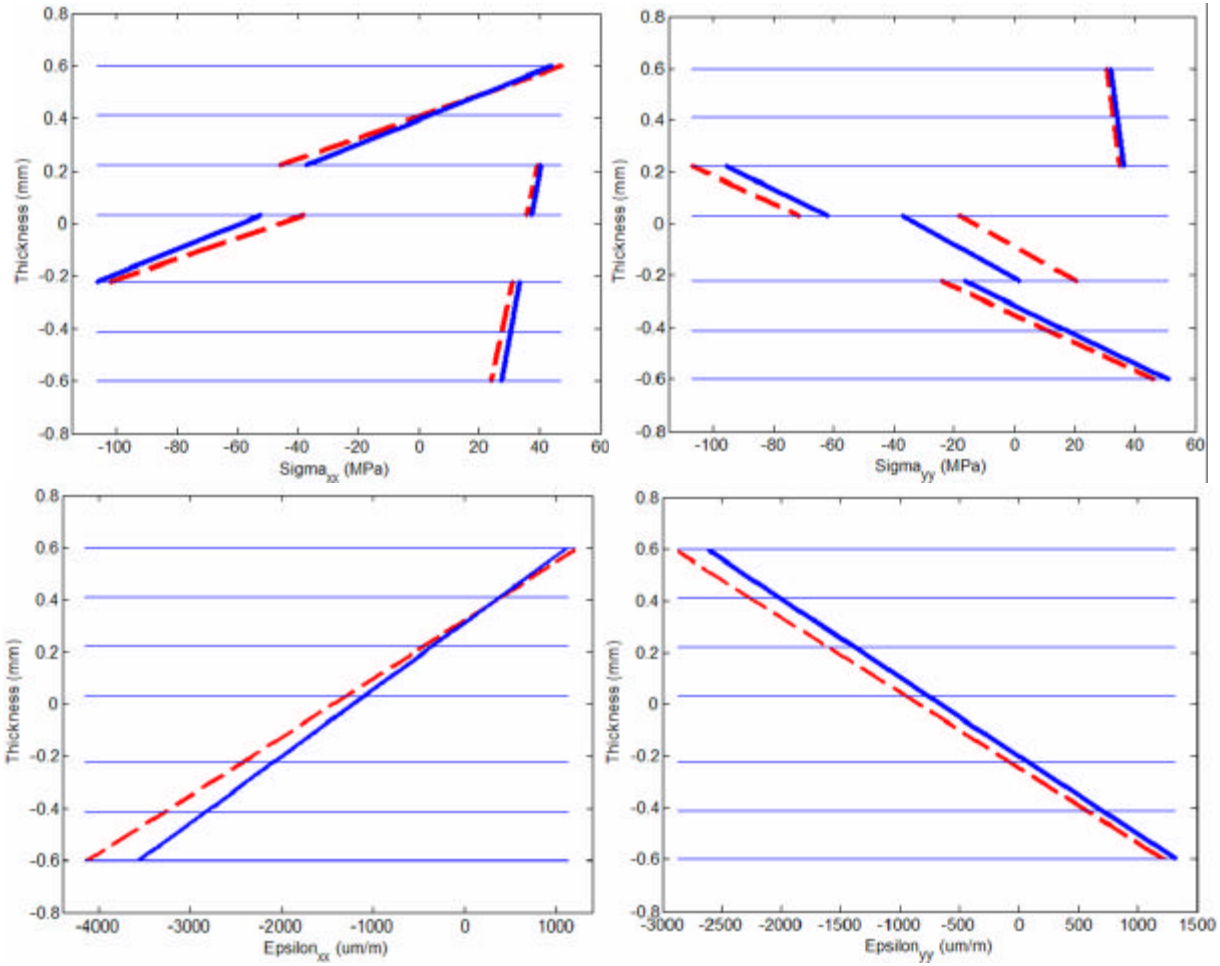

Figure 4.11b. Stress and strain distributions for zero electric field (solid) and full scale electric field (dashed) in the X_1 and X_2 directions for the [90/90/PZT/90/0/0] layup.

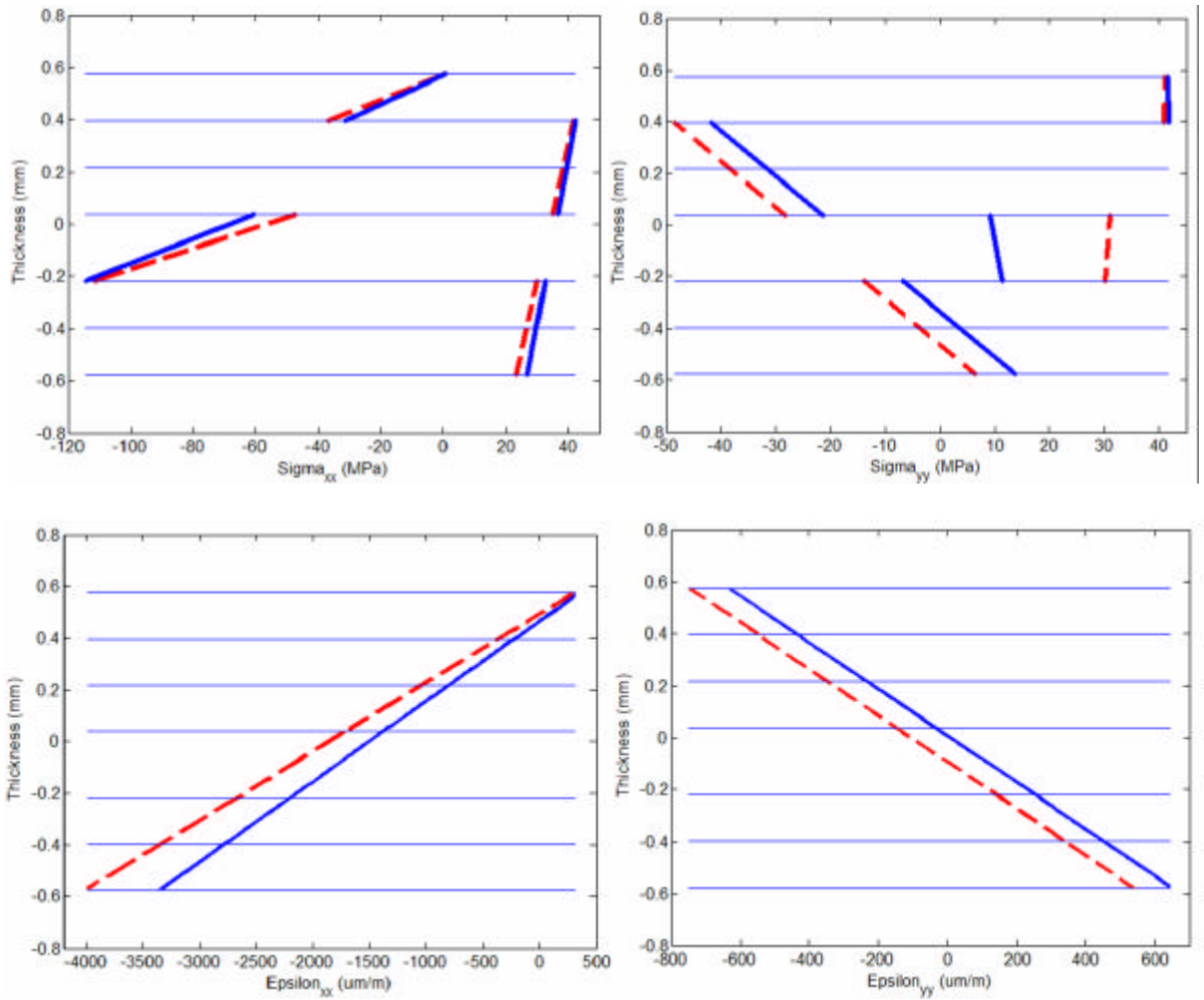

Figure 4.11c. Stress and strain distributions for zero electric field (solid) and full scale electric field (dashed) in the X_1 and X_2 directions for the [90/90/PZT/90/90/0] layup.

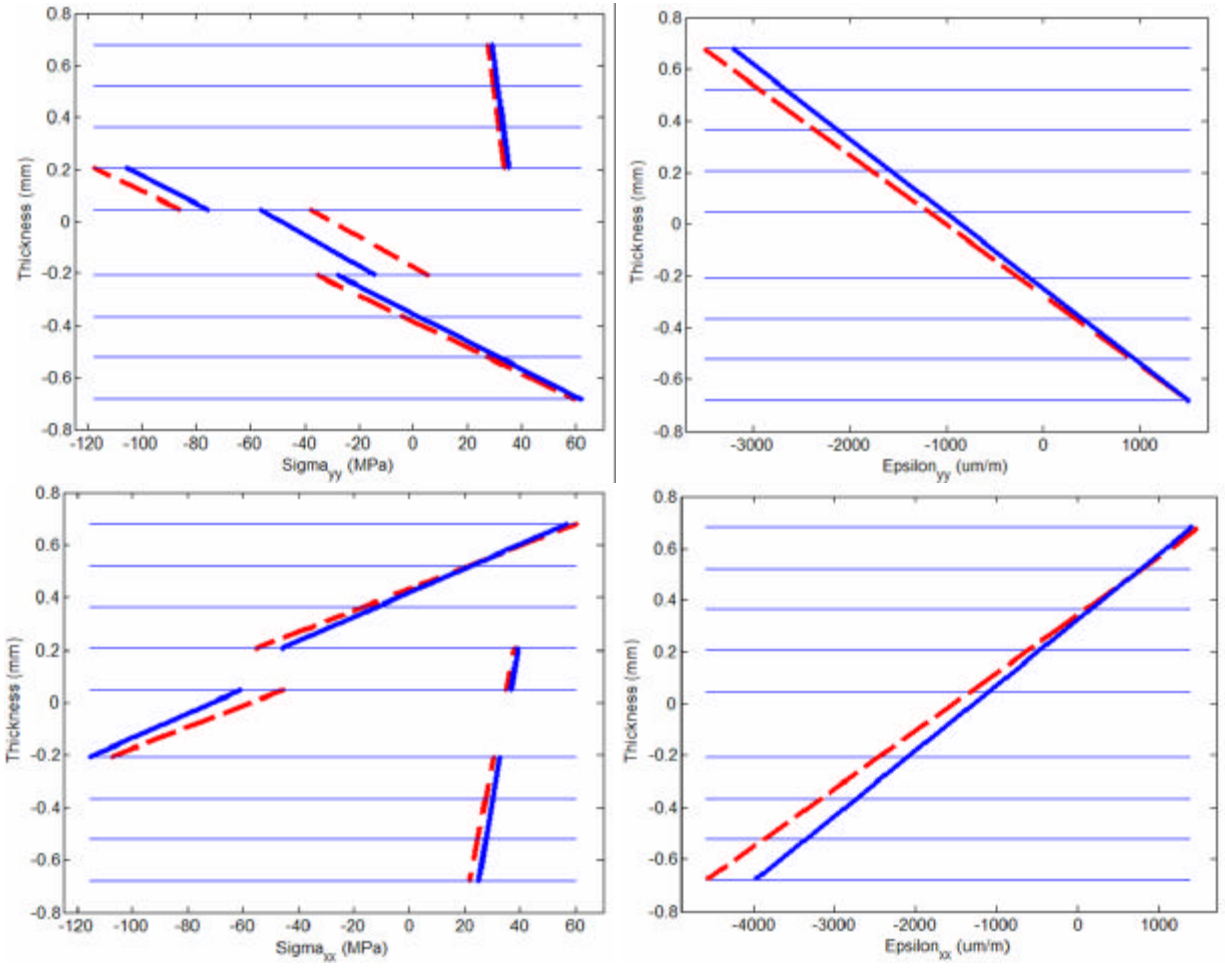

Figure 4.11d. Stress and strain distributions for zero electric field (solid) and full scale electric field (dashed) in the X_1 and X_2 directions for the [90/90/90/PZT/90/0/0/0] layup.

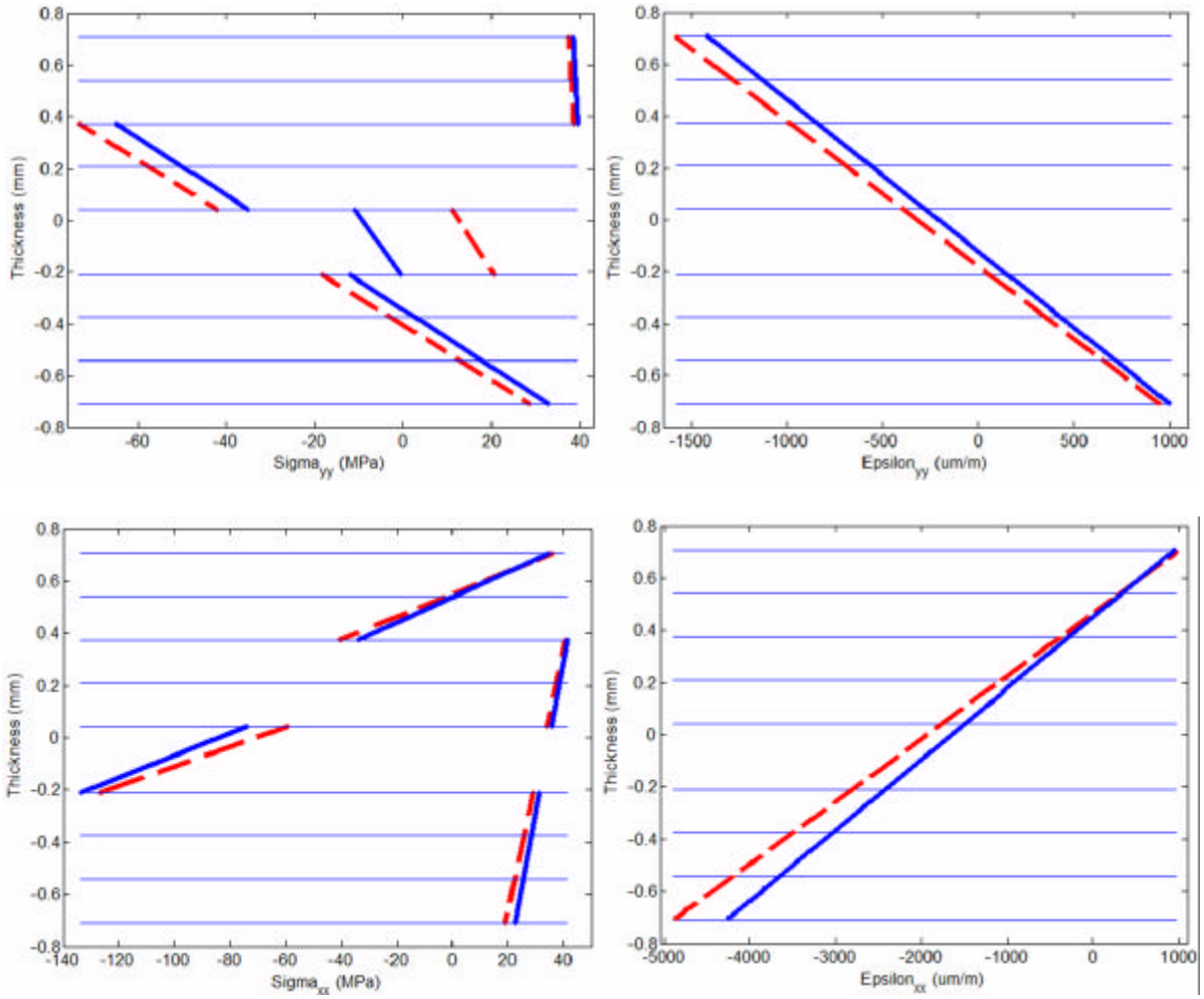

Figure 4.11e. Stress and strain distributions for zero electric field (solid) and full scale electric field (dashed) in the X_1 and X_2 directions for the[90/90/90/PZT/90/90/0/0] layup.

4.4 Extended Classical Lamination Theory

Extended classical lamination theory (ECLT) was developed by Hyer (Hyer 1981a, Hyer 1981b, Hyer 1982) to explain the non-linear behavior of unsymmetric cross-ply laminates. This theory has since been extended to laminates with other than cross-ply configurations. Built into CLT is the assumption that the strain-displacement relationship is linear. This is not the case for unsymmetric laminates where the out-of-plane displacements are many times the thickness of the structure. These large deflections cause geometric non-linearity to arise that a linear classical lamination theory cannot account for. There are three shapes possible for an unsymmetric cross-ply laminate after curing: saddle, cylindrical, and cylindrical in the opposite direction. CLT only predicts the saddle shape, whereas it has been discovered that two cylindrical shapes are also possible for certain unsymmetric laminates (Hamamoto 1987, Schlecht 1995, Dano 1998). The ECLT method predicts the laminate behavior by examining the total potential energy of the composite structure. The shape which minimizes the total potential energy at a given temperature below the cure temperature is considered the stable shape and therefore the one to occur. A schematic of the initial and cooled actuator shapes is shown in Figure 4.12 with appropriate nomenclature for ECLT (Aimmanee 2004).

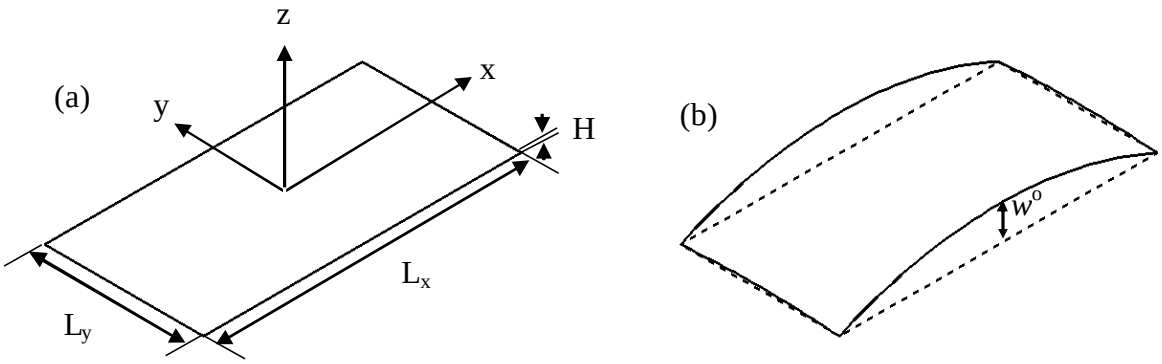

Figure 4.12. Schematic of the nomenclature used in ECLT for actuators before (a) and after (b) curing (Aimmanee 2004).

4.4.1 ECLT Assumptions

The assumptions made in ECLT are the same as for CLT which follow the Kirchhoff hypothesis for plates.

4.4.2 Total Potential Energy Function

The ECLT method revolves around minimizing the total potential energy of a laminate system. Each possible actuator shape after cooling has a total potential energy associated with it; some being higher than others. The shape which has the minimum potential energy is the most energetically favorable and therefore the one that the actuator will take. The total potential energy function for a state of plane stress is

$$p = \frac{1}{2}\int_{\frac{-Lx}{2}}^{\frac{Lx}{2}}\int_{\frac{-Ly}{2}}^{\frac{Ly}{2}}\int_{\frac{-H}{2}}^{\frac{H}{2}}[(s_x - \hat{s}_x^T)e_x + (s_y - \hat{s}_y^T)e_y + t_{xy}g_{xy}]dxdydz \qquad (4.35)$$

where $\hat{s}_x^T$ and $\hat{s}_y^T$ are the stresses due to thermal expansion in the x and y direction, respectively. Integrating through the thickness of the actuator, H, gives the total

potential energy function as a function of the normal forces and moments shown in Equation (4.36).

$$p = \int_{-\frac{Lx}{2}}^{\frac{Lx}{2}} \int_{-\frac{Ly}{2}}^{\frac{Ly}{2}} [(N_x - \hat{N}_x^T \Delta T)e_x^0 + (N_y - \hat{N}_y^T \Delta T)e_y^0 + N_{xy} g_{xy}^0 + (M_x - \hat{M}_x^T \Delta T)k_x + (M_y - \hat{M}_y^T \Delta T)k_y + M_{xy} k_{xy}]dxdy \tag{4.36}$$

where $\hat{N}_x^T$, $\hat{N}_y^T$, $\hat{M}_x^T$, and $\hat{M}_y^T$ are the normal forces and moments due to thermal expansion.

4.4.3 Approximate Displacement Expressions

Approximations were made for the displacement field of unsymmetric laminates through the observation of the curved shapes seen after curing. The approximations for the displacements in the *x*, *y*, and *z* directions, respectively, are shown in Equations (4.37).

$$\begin{aligned} u^0(x,y) &= cx - \frac{a^2x^3}{6} - \frac{abxy^2}{4} \\ v^0(x,y) &= dy - \frac{b^2y^3}{6} - \frac{abx^2y}{4} \\ w^0(x,y) &= \frac{1}{2}(ax^2 + by^2) \end{aligned} \tag{4.37}$$

The four unknown coefficients, *a*, *b*, *c*, and *d* are to be determined constants. The *a* and *b* constants describe the actuators curvature in the *x* and *y* directions, respectively. The constants *c* and *d* represent the component of $u^o(x,y)$ and $v^o(x,y)$, respectively, due to in-plane thermal strain causes by the temperature decrease.

4.4.4 Mid-plane Strains and Curvatures

As in CLT, the mid-plane strain and curvature relationships must be established. For ECLT, the non-linear strain terms for the displacement in the *z*-direction in terms of *x* and *y* are left in the strain-displacement relationship. These strain and curvature relationships are defined in terms of the approximate displacement expression in the *x*, *y*, and *z* directions shown in Equations (4.37). The mid-plane strain and curvatures are shown in Equations (4.38). The non-linear terms in the strain-displacement relationships are underlined.

$$
\begin{aligned}
e_x^0 &= \frac{\partial u^0}{\partial x} + \underline{\frac{1}{2}\left(\frac{\partial w^0}{\partial x}\right)^2} \\
e_y^0 &= \frac{\partial v^0}{\partial y} + \underline{\frac{1}{2}\left(\frac{\partial w^0}{\partial y}\right)^2} \\
g_{xy}^0 &= \left(\frac{\partial u^0}{\partial y} + \frac{\partial v^0}{\partial x}\right) + \underline{\left(\frac{\partial w^0}{\partial x}\right)\left(\frac{\partial w^0}{\partial y}\right)} \\
k_x &= -\frac{\partial^2 w^0}{\partial x^2} \\
k_y &= -\frac{\partial^2 w^0}{\partial y^2} \\
k_{xy} &= -2\frac{\partial^2 w^0}{\partial x \partial y}
\end{aligned}
\tag{4.38}
$$

These strain-displacement and curvature displacement relations are substituted into the strain equations. The strains follow the same relationship as the CLT model and are shown in Equations (4.39).

$$
\begin{aligned}
e_x &= e_x^0 + zk_x \\
e_y &= e_y^0 + zk_y \\
g_{xy} &= g_{xy}^0 + zk_{xy}
\end{aligned}
\tag{4.39}
$$

4.4.5 Normal Force and Moment Resultants

ECLT utilizes the relationship between normal forces, moments, stiffness matrices, strains, and curvatures shown in Equation (4.27). The normal forces and moments in an actuator are found in the same fashion as CLT; by integrating the stresses through the thickness of the actuator. Equations (4.28-4.29) show these relationships. Additionally, the same thermal and piezoelectric force and moment expressions are used in ECLT which are shown in Equations (4.30-4.34).

4.4.6 Minimizing the Total Potential Energy Equation

To utilize the ECLT method the four unknown coefficients must be solved for by minimizing the potential energy equation. First, the displacement approximations, found in Equations (4.37), are substituted into the mid-plane strain and curvature equations shown in Equations (4.38) which are in turn substituted into the strain and curvature relationships found in Equations (4.39). These strain and curvature terms are then used in the normal force and moment equations along with the stiffness matrices found from the material properties of the composite. The expressions for the force and moment resultants and the strains and curvatures are then substituted into the total potential energy equation.

To determine the four unknown coefficients, the potential energy equation is integrated with respect to x and y over the dimensions of the actuator. This yields a potential energy equation that is a polynomial equation containing material property terms and the four unknown coefficients. The potential energy expression is then minimized by taking the first variation with respect to each unknown. This leads to a

system of four polynomial equations that are set equal to zero to ensure equilibrium and can then be solved to obtain the four unknown coefficients. To ensure that the solution solved for is the minimum and not the maximum, a second variation is taken as shown in Equation (4.40). This gives a 4 x 4 matrix, referred to as matrix [C]. If the eigenvalues of [C] are positive definite then the solution is stable, if the eigenvalues are not positive definite then the solution is unstable.

$$[C] = \begin{Bmatrix} \partial a \\ \partial b \\ \partial c \\ \partial d \end{Bmatrix} [p] \{\partial a \quad \partial b \quad \partial c \quad \partial d\} \tag{4.40}$$

Once the coefficients that create the minimum potential energy situation for the actuator are found they can be substituted directly back into the approximate displacement expressions in Equations (4.41) along with the *x* and *y* position to find the displacement at that point.

4.4.7 ECLT Model Computer Program

A Matlab™ computer program was created to predict actuator behavior using extended classical lamination theory. This program allows the user to predict the actuator dome height and curvature, as well as the stress and strain distribution through the thickness of the actuator, from material properties and dimensions. This allows different designs to be optimized before building an actuator. Each design can be checked to ensure residual compression on the PZT plate and that the behavior characteristics, such as initial curvature or moment output, are sufficient.

The computer program is setup to be general and applicable to any laminate panel, not just ECLIPSE actuators. Since the CLT and ECLT model use the same material properties and actuator dimensions and layups the user is prompted with the same questions as the CLT model program. The user is first prompted to enter the actuator dimensions and operating conditions which include the number of layers, the length, curing temperature, electric field, and position of the PZT plate in the stacking sequence. The material properties are then entered for each ply, starting from the bottom. The program then displays the dome height and displays the graphs of the stresses and strains in the x and y directions. A flowchart for the computer program is shown in Figure 4.13.

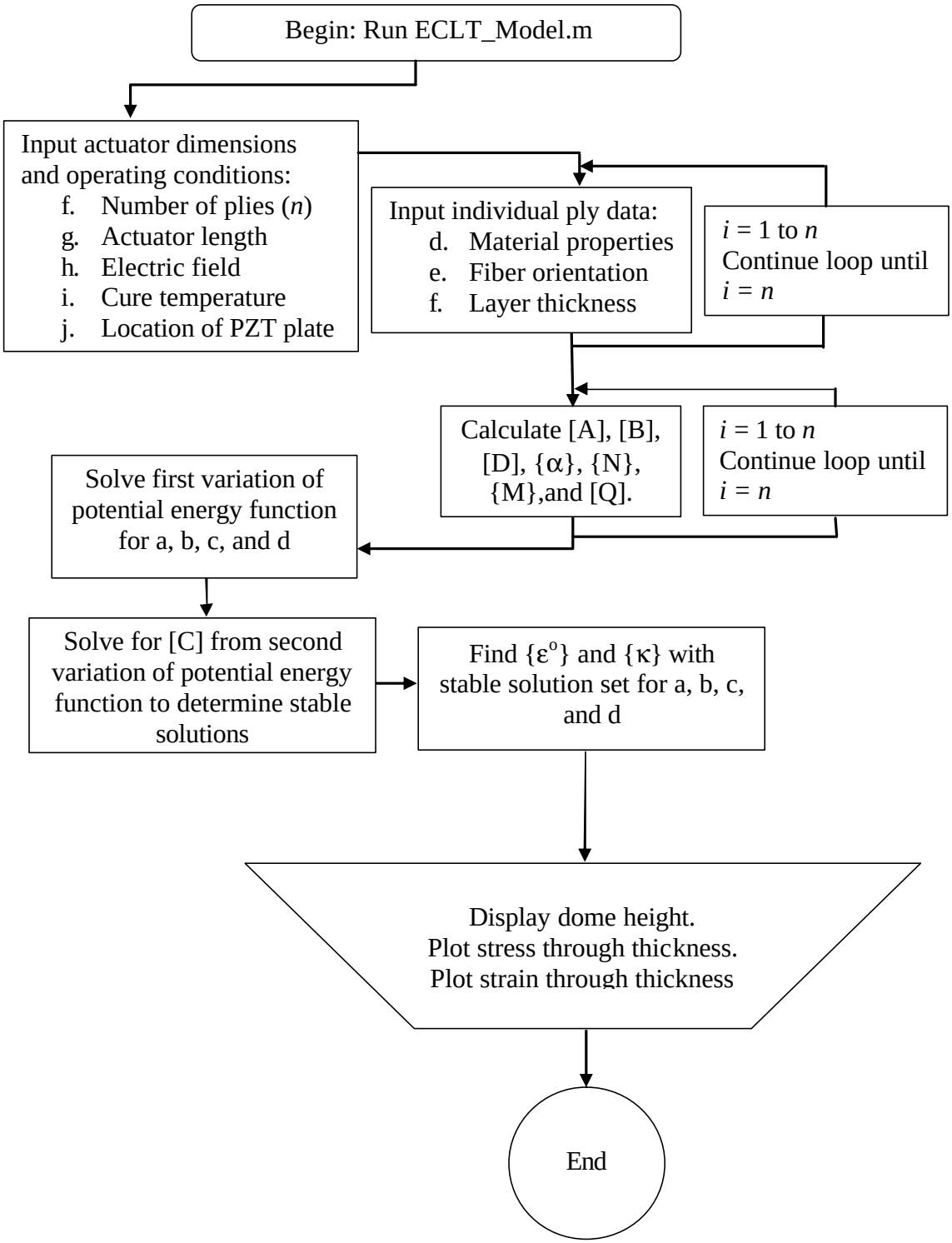

Figure 4.13. ECLT computer program flowchart.

4.4.8 Comparison of Measured and Predicted Dome Heights

The ECLT model was compared to the measured initial dome height and dome height displacement of five specimens. The specimens are the same actuators used for comparison to the CLT model. Table 4.3 contains the stacking sequence for the different specimens. Figures (14a-14e) show the comparison between the ECLT model and the tested actuators.

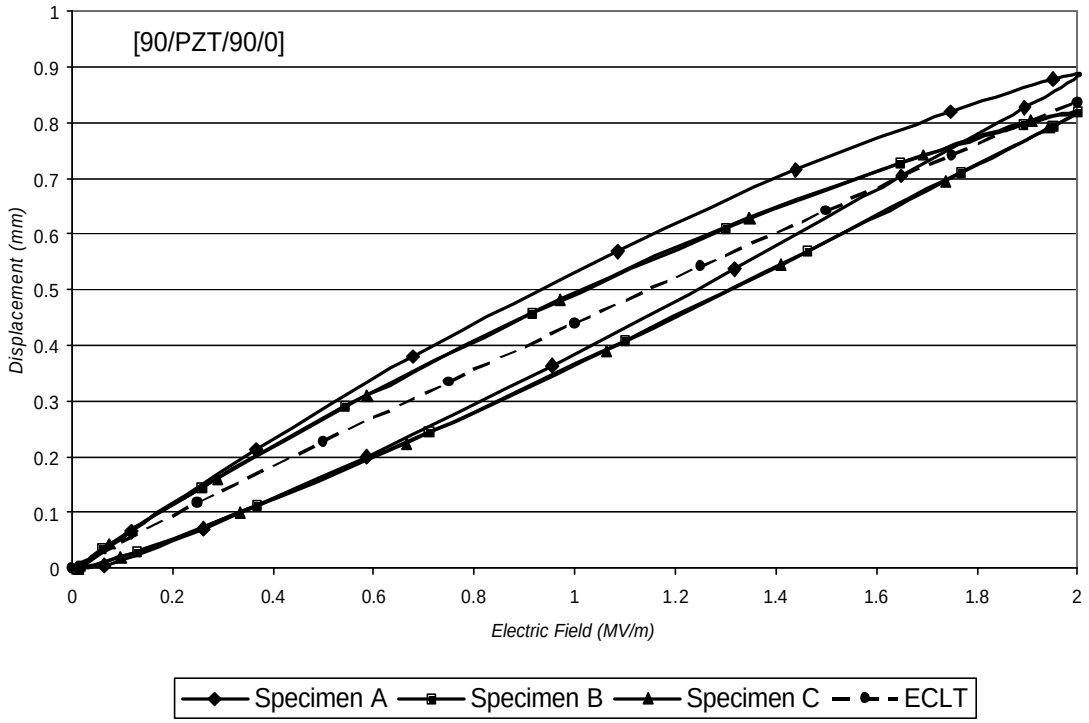

Figure 4.14a. Displacement vs. electric field for the LVDT measurements and ECLT model

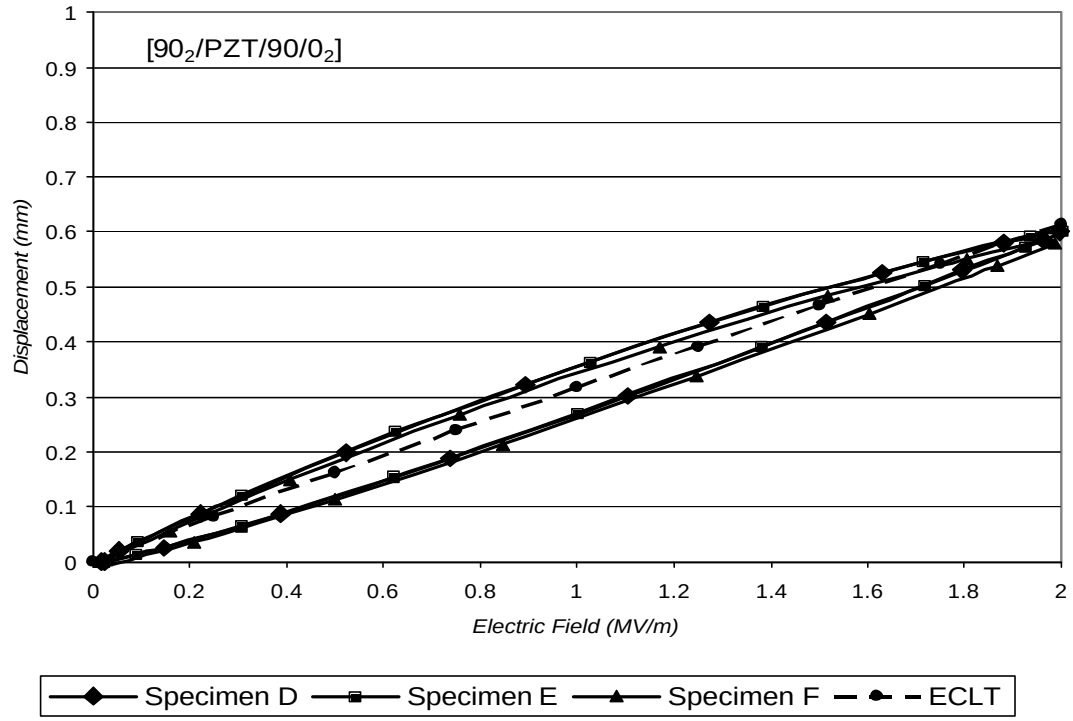

Figure 4.14b. Displacement vs. electric field for the LVDT measurements and ECLT model

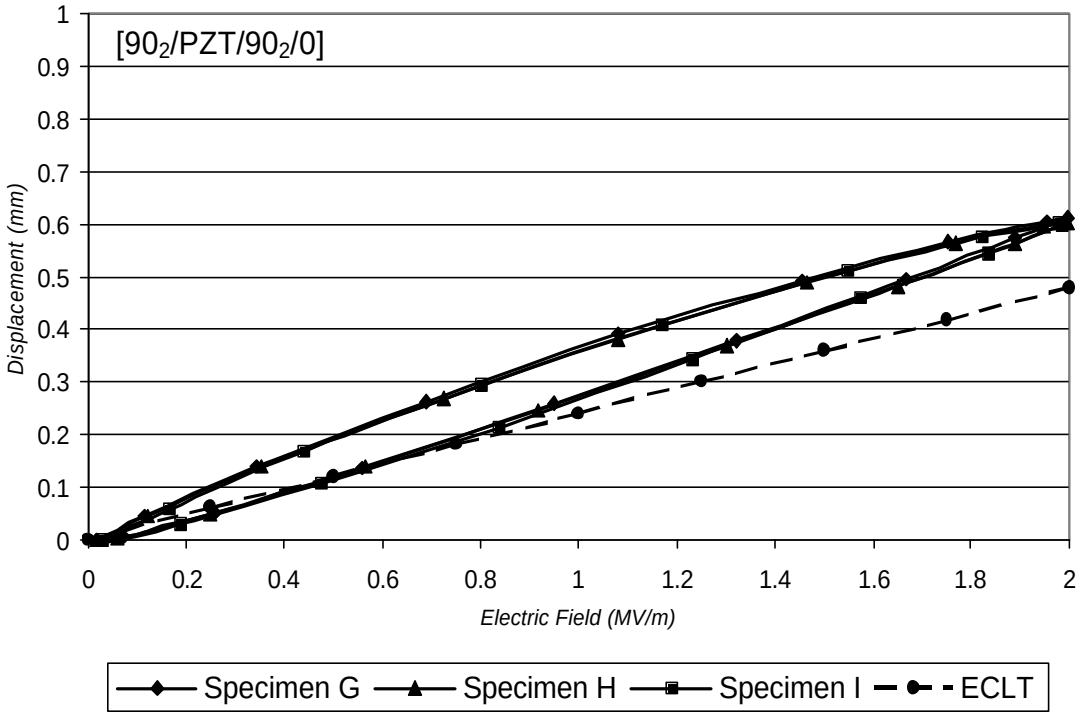

Figure 4.14c. Displacement vs. electric field for the LVDT measurements and ECLT model

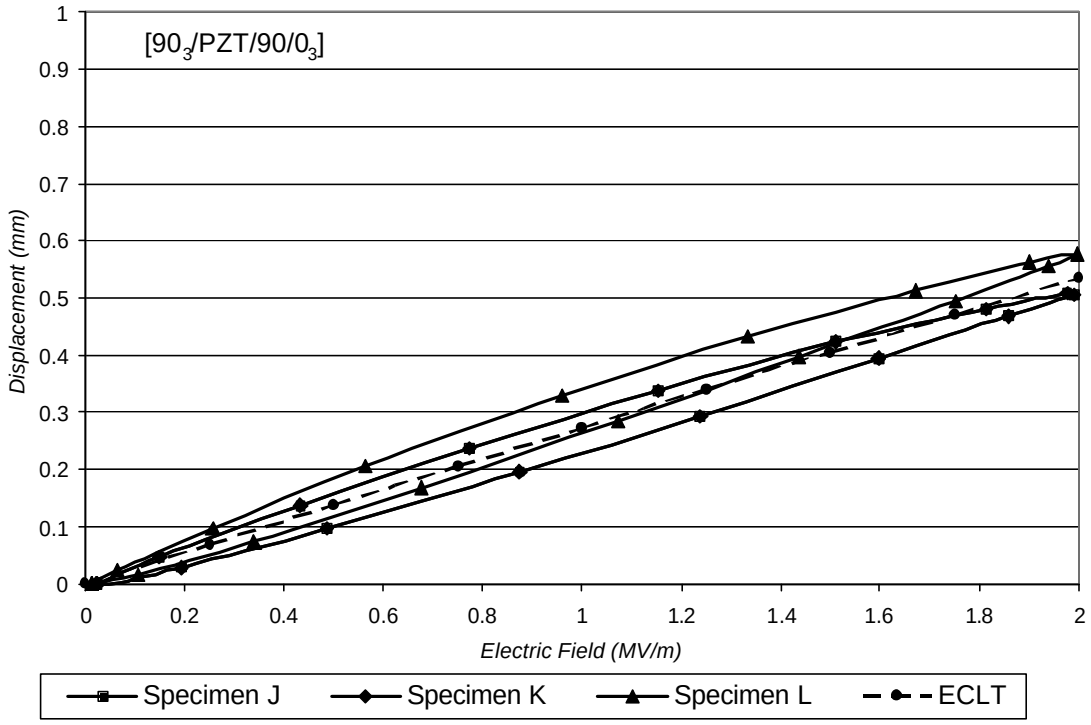

Figure 4.14d. Displacement vs. electric field for the LVDT measurements and ECLT model

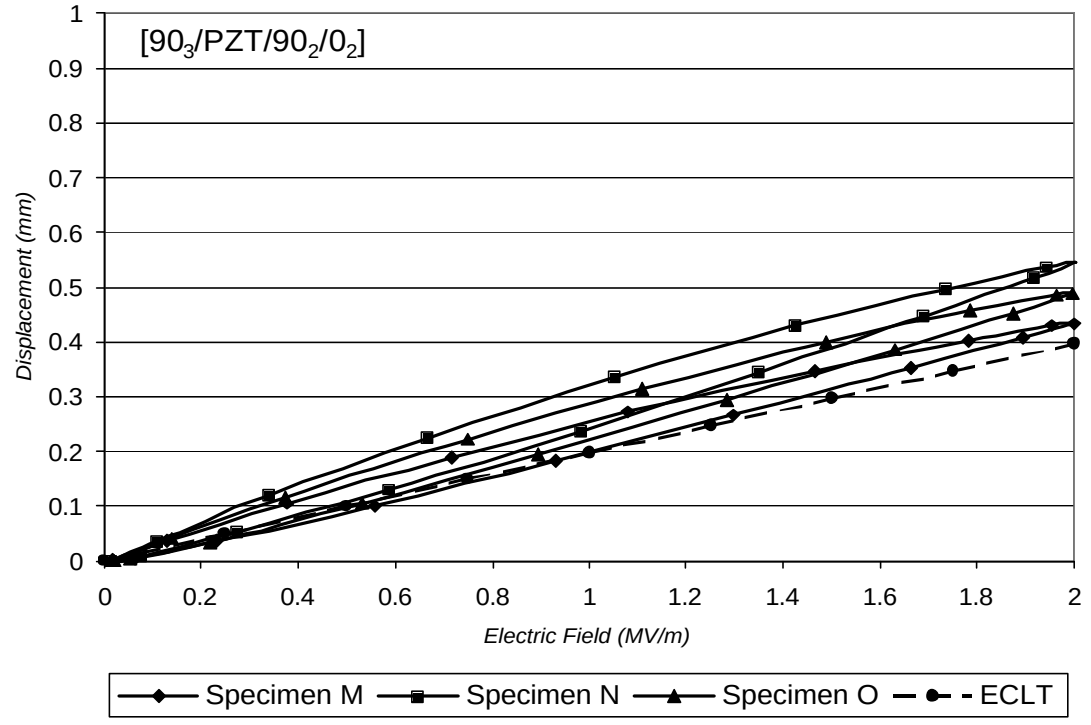

Figure 4.14e. Displacement vs. electric field for the LVDT measurements and ECLT model

The initial actuator dome height predicted by the ECLT model is compared to the measured results in Table 4.3 and the predicted slope of the actuator dome height displacement is compared to the measured values in Table 4.4. The hysteresis loop of the actuator was not considered when finding the slope of the measured actuators.

Table 4.4. Comparison of measured initial dome heights to CLT predictions.

	Actuator 1		Actuator 2		Actuator 3		
	Height (mm)	Diff	Height (mm)	Diff	Height (mm)	Diff	ECLT Model
[90/PZT/90/0]	3.19926	31.31%	3.3481	37.42%	3.5769	46.81%	2.4364
[90_2/PZT/90/0_2]	3.3988	28.50%	3.5606	34.62%	3.5718	35.04%	2.645
[90_2/PZT/90_2/0]	3.0309	18.64%	3.0607	19.81%	3.0458	19.22%	2.5547
[90_3/PZT/90/0_3]	3.4785	33.50%	3.1715	21.72%	2.9278	12.37%	2.6056
[90_3/PZT/90_2/0_2]	3.59506	24.75%	3.27322	13.58%	3.43135	19.07%	2.8819

Table 4.5. Comparison of measured dome height displacement slopes to CLT predictions.

	Actuator 1		Actuator 2		Actuator 3		
	Slope (dh/dE)	Diff	Slope (dh/dE)	Diff	Slope (dh/dE)	Diff	ECLT Model
[90/PZT/90/0]	0.44276	5.77%	0.4102	-2.01%	0.4102	-2.01%	0.4186
[90_2/PZT/90/0_2]	0.30045	-2.17%	0.30045	-2.17%	0.29208	-4.89%	0.3071
[90_2/PZT/90_2/0]	0.30509	27.61%	0.30045	25.67%	0.301377	26.05%	0.239085
[90_3/PZT/90/0_3]	0.24463	-8.53%	0.2539	-5.07%	0.28835	7.81%	0.26745
[90_3/PZT/90_2/0_2]	0.2167	9.44%	0.27161	37.18%	0.244636	23.55%	0.198

The ECLT model predicted the initial dome height, on average, within 26.4% of the actual measured values for every layup. The maximum difference between the model and the measured occurred for the [90/PZT/90/0] layup, which was 46.8%. The ECLT model was able to predict the slope of the dome height displacement with more accuracy. The model predicted the dome height differed from the measured values by an average of 12.7% for all of the layups.

ECLT models prediction capabilities are the reverse of the CLT models. The ECLT model closely predicted the change in dome height with change in electric field, but varied from the initial curvature by a maximum of almost 1 mm for the $[90_2/PZT/90/0_2]$ layup. This difference between the measured and predicted dome heights is due to the displacement approximation functions not accurately representing the laminate displacements. Further research by Aimmanee and Hyer has shown that the four coefficient displacement approximations are best suited to describing the behavior of square laminate panels. They proposed extended displacement approximations that use 23 unknown coefficients. This has been shown to accurately predict the out-of-plane displacements of rectangular laminates. Attempts to implement this newer model were hampered by the computation requirements of solving 23 equations for 23 unknowns in addition to solving for the eigenvalues of a 23 x 23 matrix.

4.4.9 Prediction of Stresses and Strains

The ECLT model is also useful for the prediction of the stresses and strains through the thickness of the actuator. Figures (4.15a-4.15e) show the stress and strain distribution of the actuators through their thickness in the X_1 and X_2 directions for the cases of no applied electric field and full electric field (2 MV/m). The figures illustrating the stress and strain in the X_1 direction show that there is a compressive stress on the PZT plate which is located below the neutral axis. The ECLT model shows, like the CLT model, that applying a positive electric field to the PZT plate makes the dome height of the actuator increase in addition to an increased tensile load on the PZT plate. Similar to the CLT model, the ECLT model shows that the same 90^o plies that caused

compression in the X_1 direction cause an increase in the tensile load of the PZT plate in the X_2 direction. This effect was increased in layups when more 90^o plies are exchanged for 0^o plies above the PZT plate. The ECLT model tends to predict more of a compressive force on the PZT plate in the X_2 direction however. This is due to the differences in the predicted curvatures between the models. The CLT model predicts more curvature in the X_1 and X_2 directions, which increase the strains and therefore the stresses seen in the actuators. Another interesting point to note is that most of the layups have an entirely compressive strain in the X_2 direction which means that the neutral axis is not located within the thickness of the actuator, but below it.

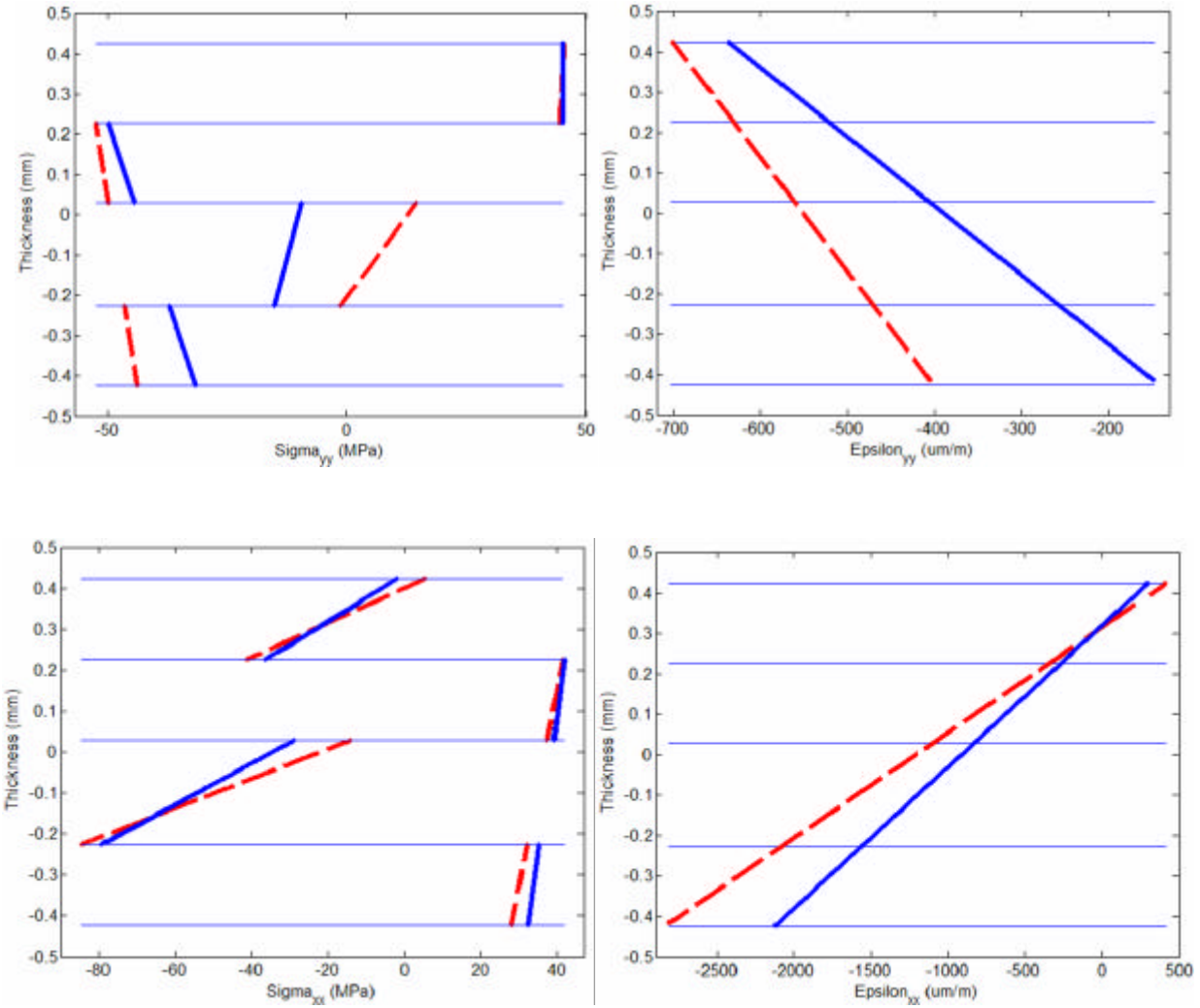

Figure 4.15a. Stress and strain distributions for zero electric field (solid) and full scale electric field (dashed) in the X_1 and X_2 directions for the [90/PZT/90/0] layup.

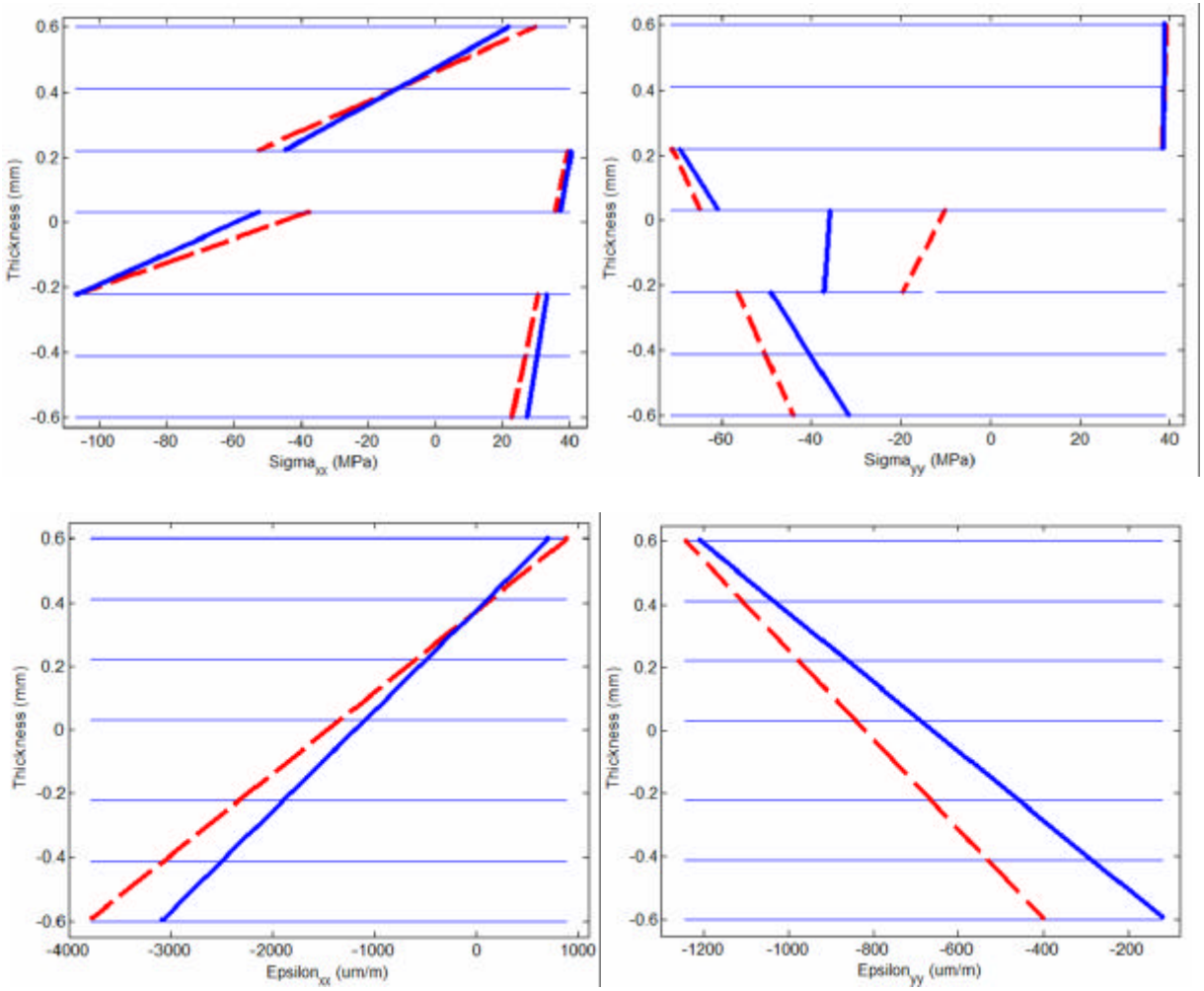

Figure 4.15b. Stress and strain distributions for zero electric field (solid) and full scale electric field (dashed) in the X_1 and X_2 directions for the [90/90/PZT/90/0/0] layup.

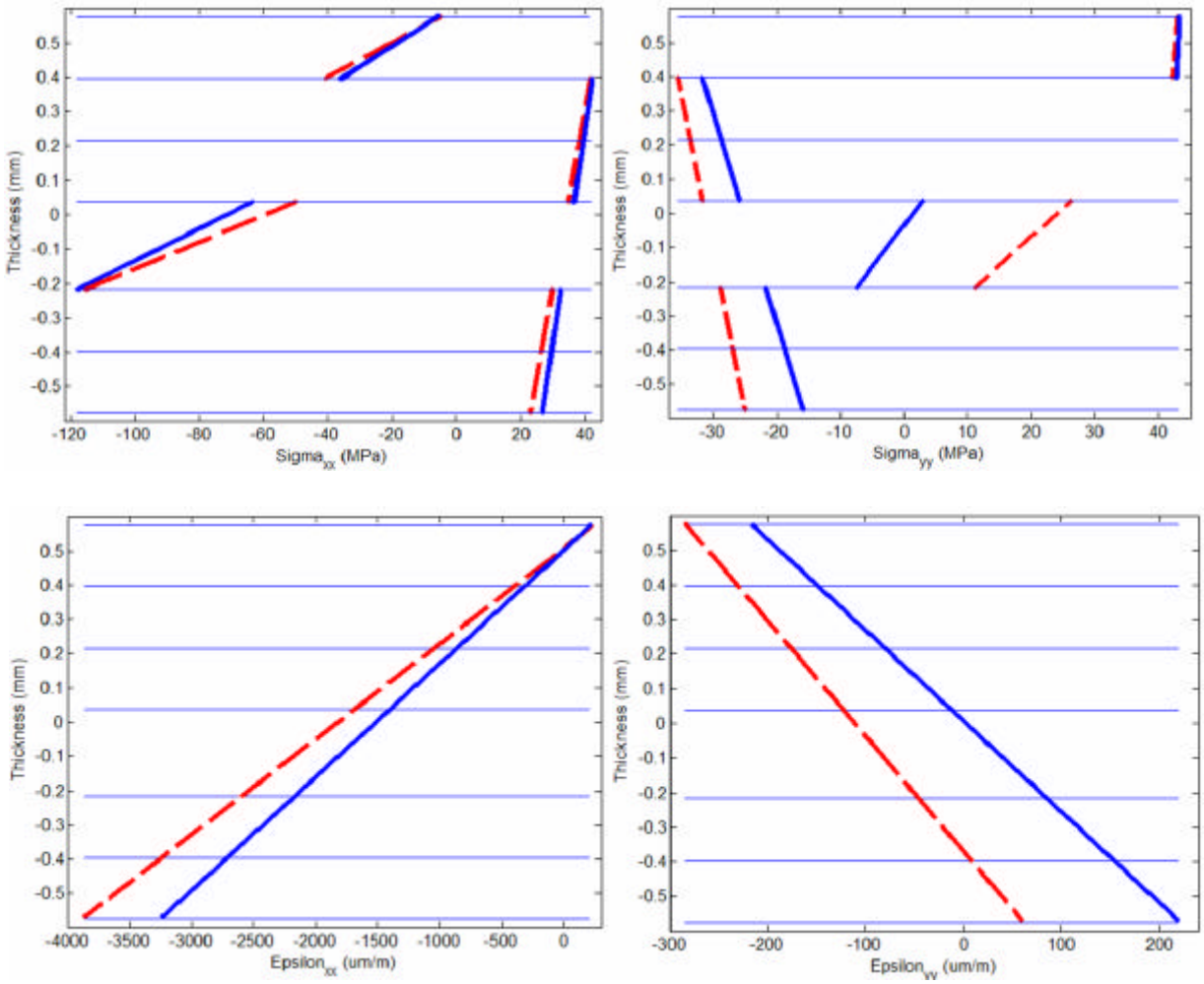

Figure 4.15c. Stress and strain distributions for zero electric field (solid) and full scale electric field (dashed) in the X_1 and X_2 directions for the [90/90/PZT/90/90/0] layup.

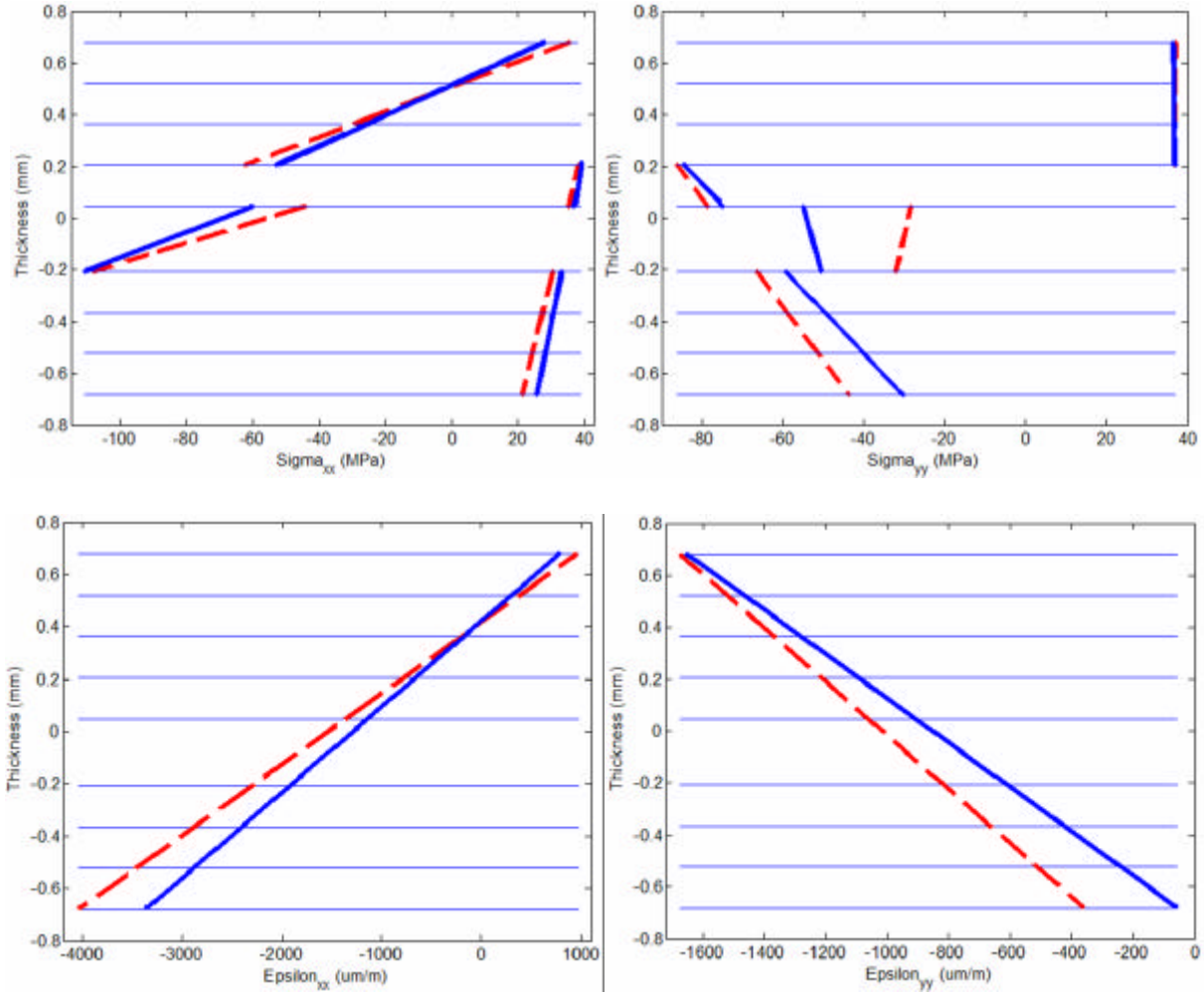

Figure 4.15d. Stress and strain distributions for zero electric field (solid) and full scale electric field (dashed) in the X_1 and X_2 directions for the [90/90/90/PZT/90/0/0/0] layup.

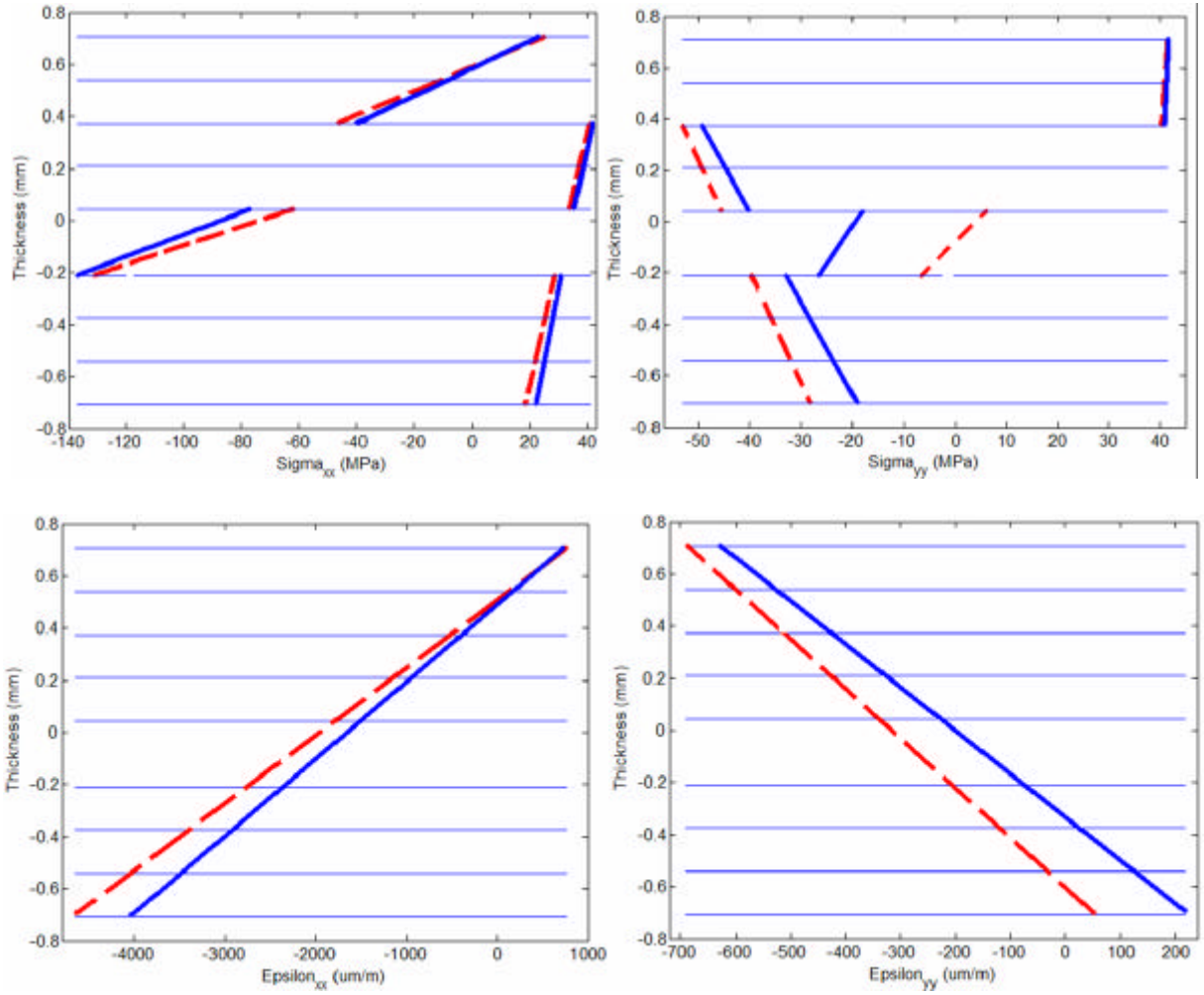

Figure 4.15e. Stress and strain distributions for zero electric field (solid) and full scale electric field (dashed) in the X_1 and X_2 directions for the [90/90/90/PZT/90/90/0/0] layup.

The stresses and the strains that are represented in Figures (4.15a-4.15e) are the stresses and strains found at the center of the actuator where $x = y = 0$. Unlike CLT, which predicts the same stress and strain distribution through the thickness in the entire actuator, ECLT predicts variations in the stresses and strains at different x and y locations. When the midplane strain and curvature relationships are derived and the four unknown coefficients are included they take the form in Equation (4.41).

$$\begin{aligned} e_x^0 &= c - \frac{1}{4}aby^2 \\ e_y^0 &= d - \frac{1}{4}abx^2 \\ g_{xy}^0 &= 0 \\ k_x &= -a \\ k_y &= -b \\ k_{xy} &= 0 \end{aligned} \tag{4.41}$$

From Equation (4.41) it can be seen that the midplane strain in the x direction varies with y and the midplane strain in the y direction varies with x. The curvatures in the x and y directions do not vary throughout the actuator. Combining the terms in the Equation (4.41) with those in Equation (4.39) yields the strain equations for ECLT using the four unknown coefficients seen in Equation (4.42).

$$\begin{aligned} e_x &= c - \frac{1}{4}aby^2 - az \\ e_y &= d - \frac{1}{4}abx^2 - bz \\ g_{xy} &= 0 \end{aligned} \tag{4.42}$$

It can be seen from Equation (4.42) that the total strain in the actuator varies through the thickness of the actuator in addition to the x and y position. Figures 4.16 and 4.17 show the midplane strain as it varies in the x and y directions, respectively.

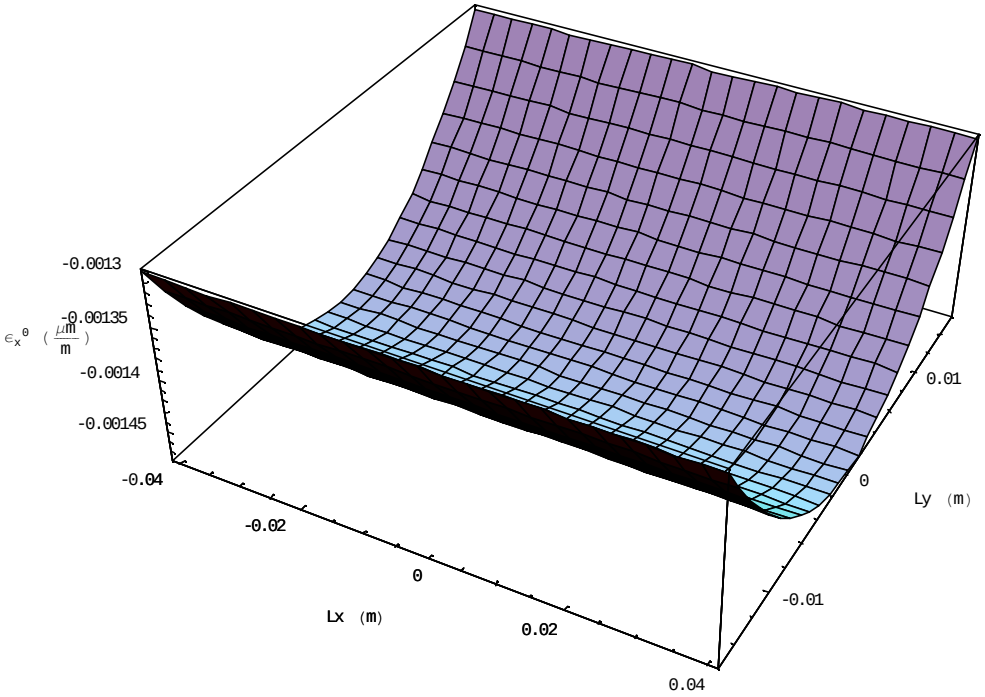

Figure 4.16. Midplane strain variation in the *y*-direction.

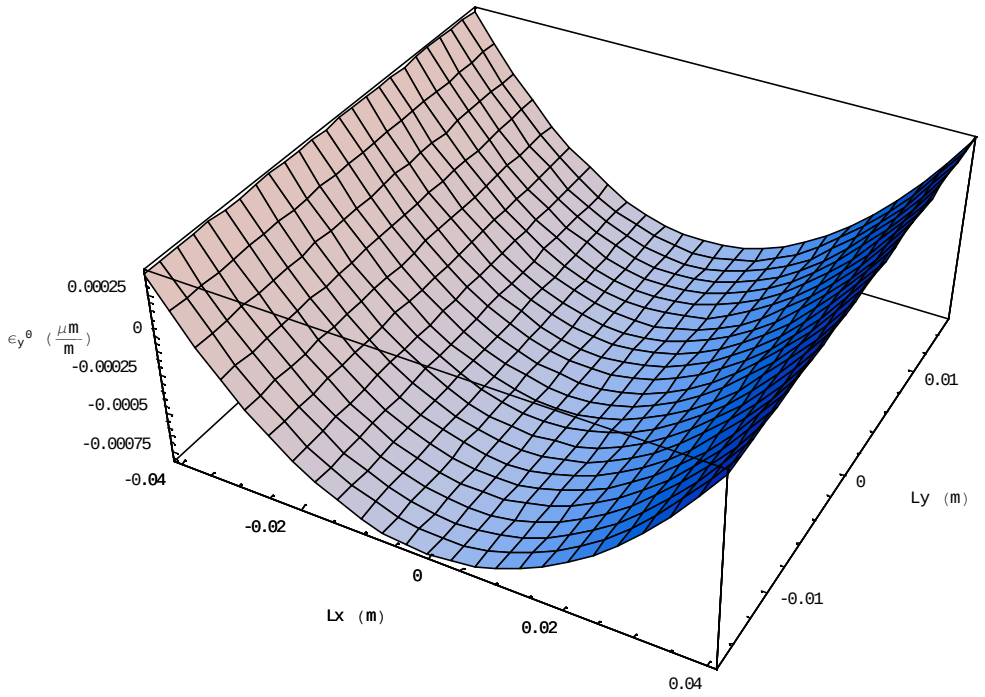

Figure 4.17. Midplane strain variation in the *x*-direction.

CHAPTER 5

CHARACTERIZATION AND EXPERIMENTATION RESULTS

5.1 Material Testing

ECLIPSE actuators were tested under various environmental and loading conditions to determine their response. Kevlar 49/epoxy composite and PZT have unique attributes and responses that must be characterized to fully understand their behavior.

5.1.1 Moisture Absorption

Moisture absorption is a concern for Kevlar 49 fibers. Typically for glass, carbon, and boron fibers the volume of moisture absorbed by the fibers relative to the volume of moisture absorbed by the matrix material is insignificant. This is not that case for Kevlar 49 fibers, which are strongly hygroscopic and often absorb more water than the matrix materials in composites. The effect of exposing ECLIPSE actuators to laboratory air was examined by placing three actuators inside a dark environment that allowed for the passage of air. Figure 5.1 shows the percent change in weight over the trial period. Each actuator followed the same pattern of moisture absorption. The offset between actuators was due to variations in the amount of copper foil, solder, and wire used in each actuator. The dome height displacement was measured for each actuator following fabrication using the LVDT. The actuators were allowed to absorb moisture from the air for 65 days. After this time the displacement was again measured. Figure 5.2 shows the displacements of a representative actuator before and after exposure to atmospheric moisture.

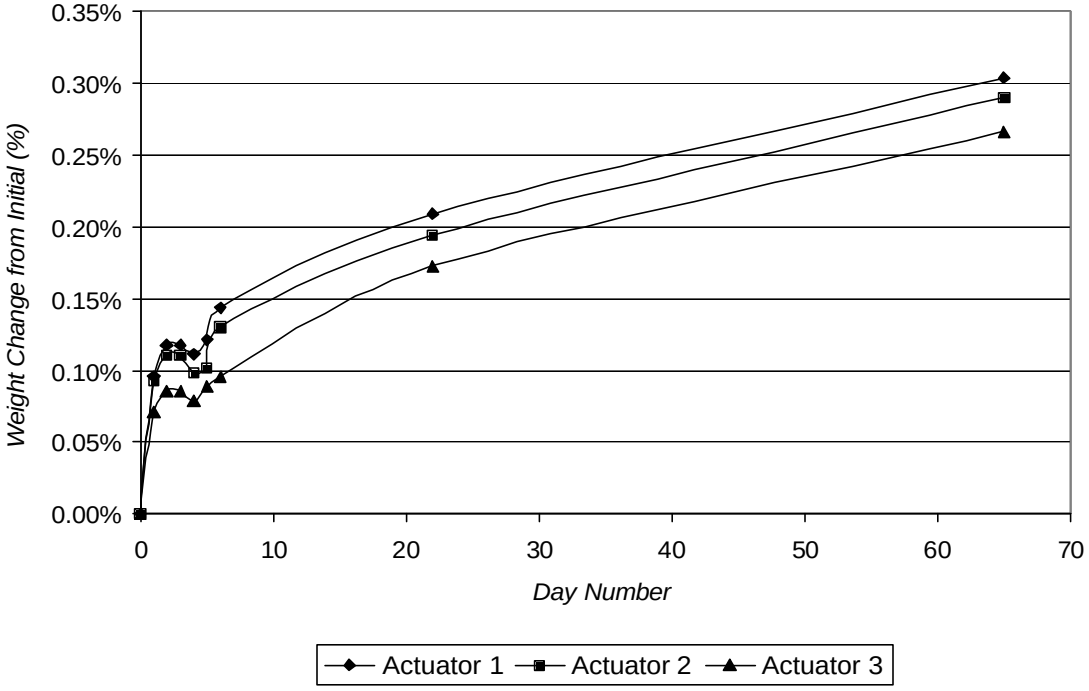

Figure 5.1. Moisture absorption of ECLIPSE actuators in laboratory air

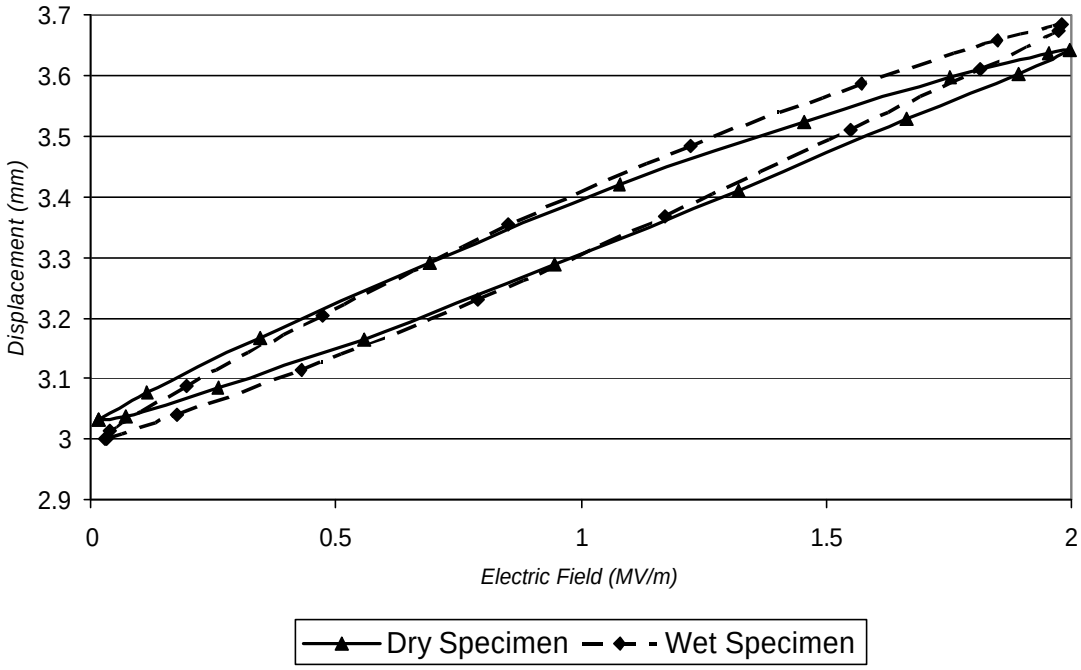

Figure 5.2. Displacement before and after moisture absorption.

After the specimen was allowed to absorb water, the initial dome height decreased and the displacement increased. When composite materials absorb moisture, thermal stresses relax due to the composite material swelling. This explains the decrease in the initial dome height. This effect has been shown to improve the tensile strength and modulus for absorption of small amounts of water by unidirectional prepreg composite made from Kevlar 49 and TGMDA/DDS epoxy resin (Roylance 1976). Adverse effects occur in laminates at increased levels of moisture absorption from deterioration due to resin plasticisation, interface failure, and fiber degradation (Akay 1997).

These results indicate that there is little effect from leaving the actuators in contact with laboratory air for an extended period of time.

5.1.2 Piezoelectric Failure Testing

The maximum recommended electric field operating range for 3195HD material is from -1.2 MV/m to +2 MV/m. To determine where failure occurs past this range two actuators for five different layups were tested. Each actuator was cycled from 0 MV/m to 4 MV/m at a frequency of $1/100^{th}$ Hz.

Failure did not occur at the same point for different actuators. This was the expected result. The measured points of failure indict that the actuators with more plies, and higher residual compression on the PZT plates, failed less frequently. The actuators also failed after a number of cycles, which indicts that the reason for failure was not solely due to an overload of electric field. Table 5.1 summarizes for each layup which cycle failure occurred on, if any, and what the electric field was at the point of failure.

Given the extreme loading condition, actuators that survived 12 cycles without failure were assumed to not fail.

Table 5.1. Summary of the cycle and electric field where failure occurred.

Layup	Actuator 1		Actuator 2	
	Cycle	Electric Field	Cycle	Electric Field
[90/PZT/90/0]	10	3.96	No Failure	
[90/90/PZT/90/0/0]	5	3.69	1	3.93
[90/90/PZT/90/90/0]	3	3.58	No Failure	
[90/90/90/PZT/90/90/0/0]	No Failure		No Failure	
[90/90/90/PZT/90/0/0/0]	No Failure		No Failure	

When an overload caused failure, the piezoelectric material started to break down and eventually short-circuited. This caused an arc to jump through the PZT plate and failure of the actuator. Figure 5.3 shows a picture of PZT plate in an ECLIPSE actuator that was short-circuited during operation. The plate was sectioned and polished to show the area of short-circuiting. There was also a cavity that is a delaminated section caused by the short-circuiting. This void is labeled in Figure 5.3.

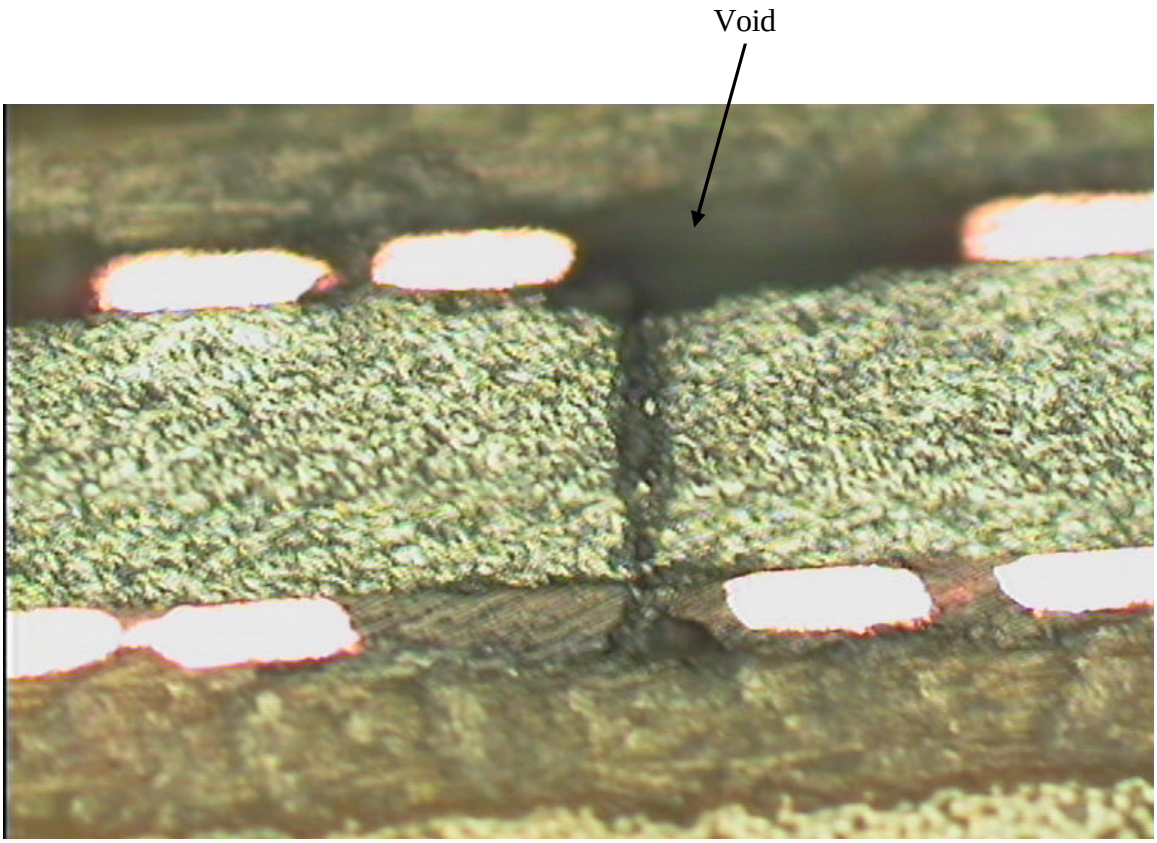

Figure 5.3. Picture of PZT plate exposed to a high electric field.

5.1.3 Cure Temperature Sensitivity

Actuators were cured at various temperatures to determine actuator sensitivity to cure temperature as well as the CLT and ECLT prediction capabilities. Three actuators were tested for each cure temperature. The temperatures considered were 157, 167, 177, 187, and 197 ^{o}C. The cure temperature recommended by the composite manufacturer, APCM, is 177^{o}C. Each actuator had a $[90_2/PZT/90/0_2]$ layup with dimensions of 82.55mm x 31.75mm x 1.2mm (3.25” x 1.25” x 0.05”). The initial dome height and dome height displacement were measured using the LVDT immediately following curing and post-processing. Each actuator was cycled between 0 MV/m and 2 MV/m at ¼ Hz and compared to CLT and ECLT models. Figure 5.4 shows displacement versus electric

field graphs for various cure temperatures. The previous figure shows that the cure temperature has an effect on the initial shape of the actuators, but has little effect on the response of the actuator to electric field. All 15 actuators had the same displacement. The only temperature that showed a significant change in initial dome height was the actuators cured at 157 ^{o}C. The initial dome heights of the other actuators were within 0.1 mm of each other.

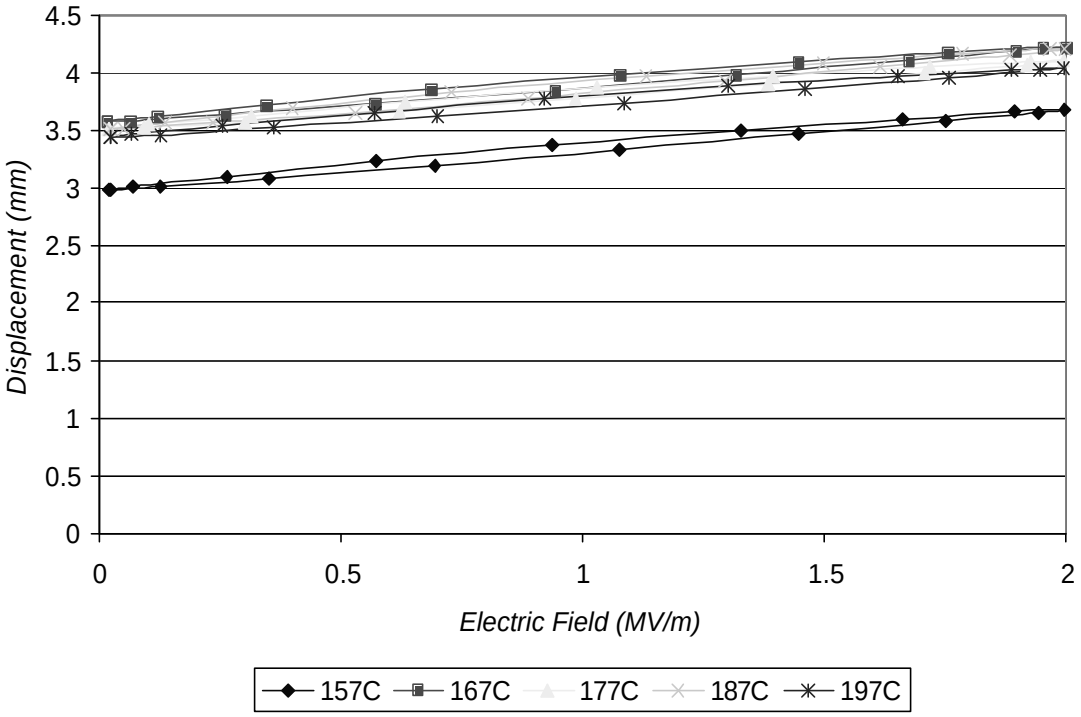

Figure 5.4. Displacement versus electric field for various cure temperatures.

Figures 5.5a - 5.5e show the experimental results for the three actuators tested at each cure temperature. The predictions for the CLT and ECLT models are also shown. Tables 5.2a - 5.2d show the CLT and ECLT prediction in comparison to the measured values for the initial dome heights and slope of the hysteresis loops.

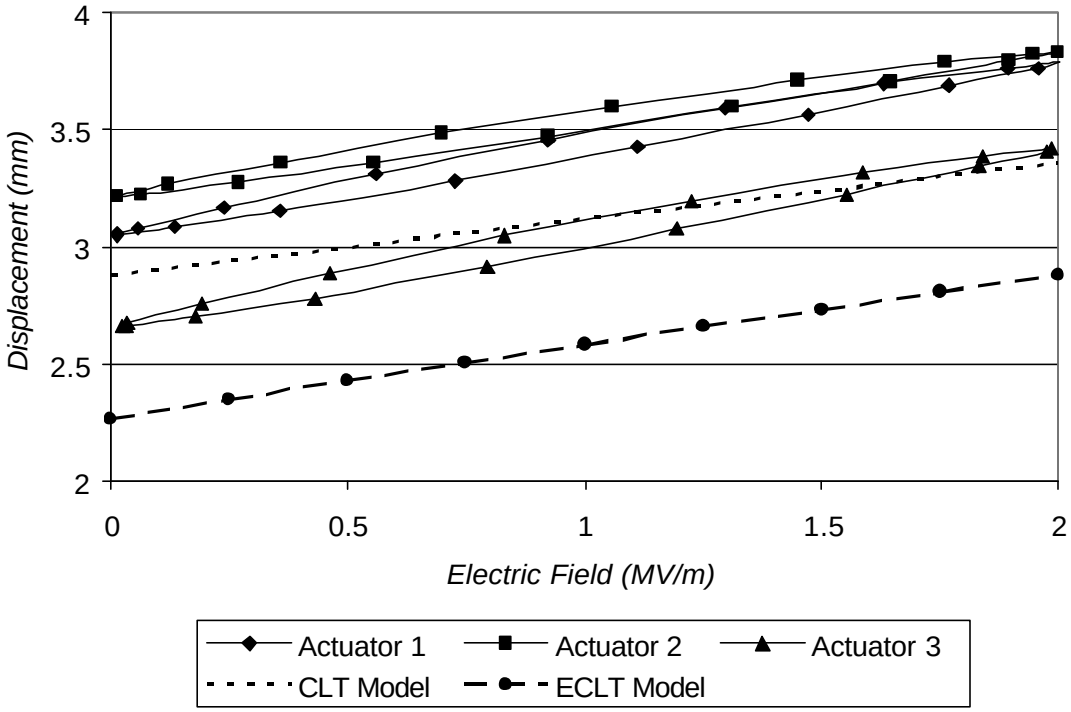

Figure 5.5a. Comparison of experimental data to CLT and ECLT models for a cure temperature of 157°C.

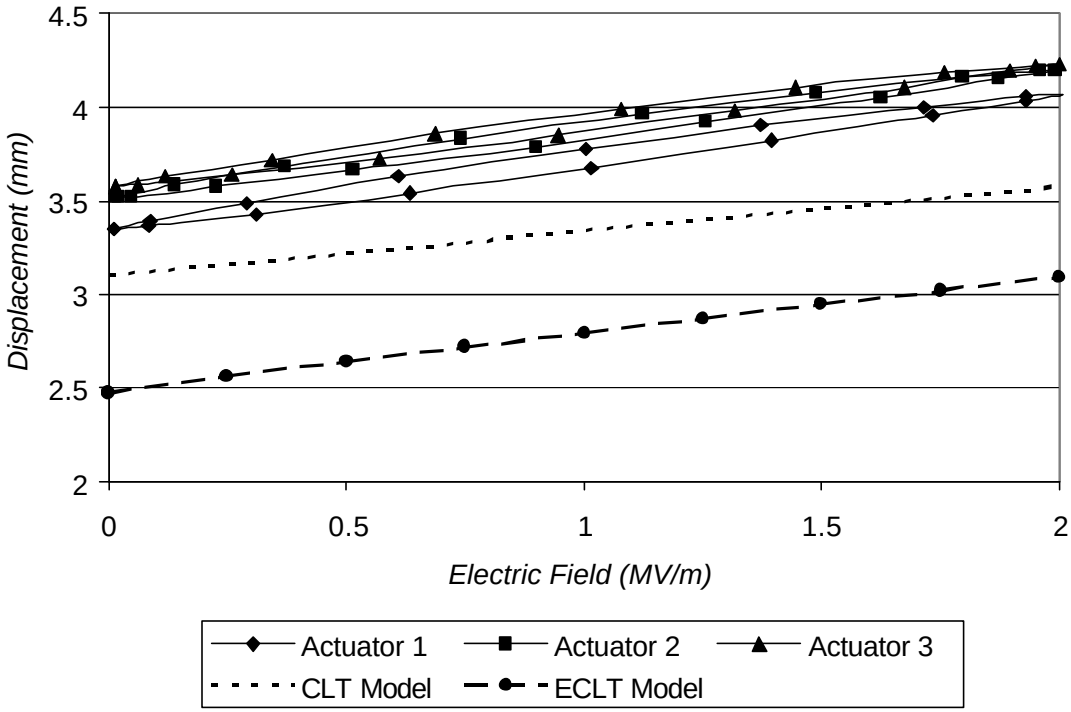

Figure 5.5b. Comparison of experimental data to CLT and ECLT models for a cure temperature of 167°C.

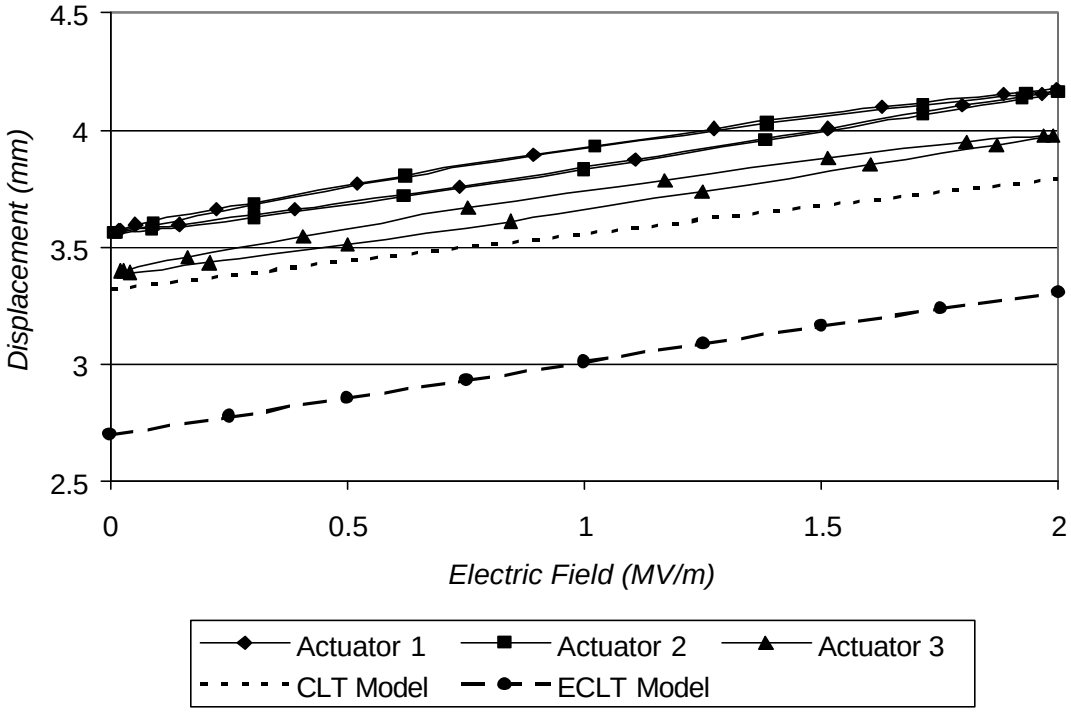

Figure 5.5c. Comparison of experimental data to CLT and ECLT models for a cure temperature of 177°C.

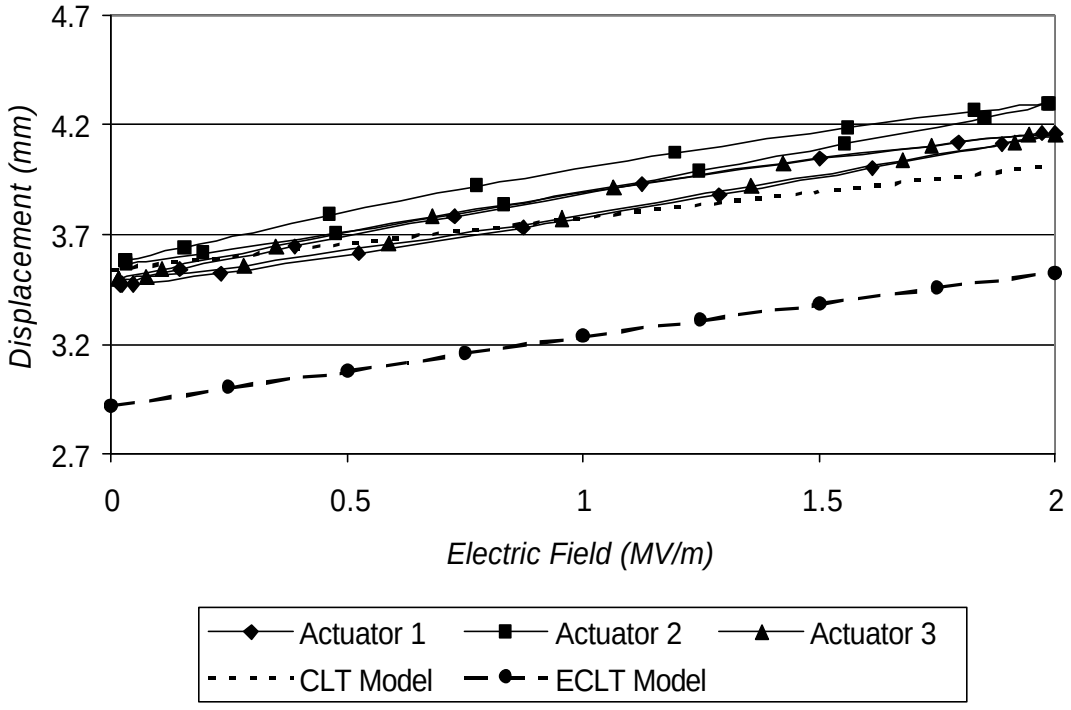

Figure 5.5d. Comparison of experimental data to CLT and ECLT models for a cure temperature of 187°C.

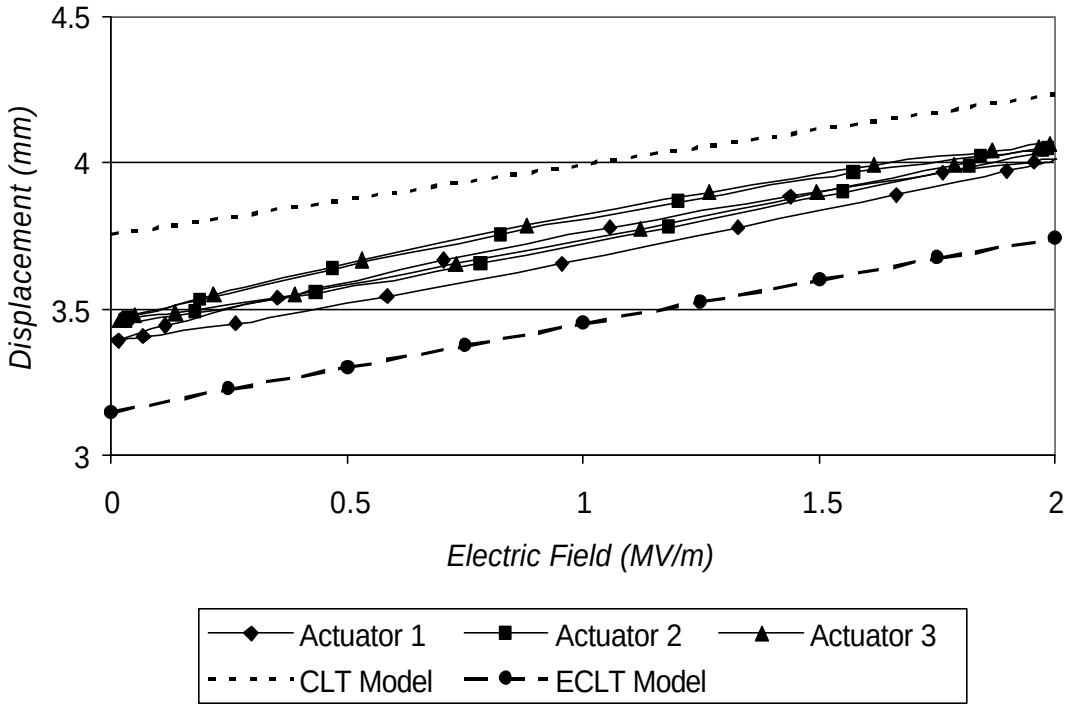

Figure 5.5e. Comparison of experimental data to CLT and ECLT models for a cure temperature of 197°C.

Table 5.2a. Comparison of the CLT model initial dome height predictions to actuators cured at various temperatures.

	Actuator 1		Actuator 2		Actuator 3		
	Height (mm)	Diff	Height (mm)	Diff	Height (mm)	Diff	CLT Model
157 °C	3.0528	5.87%	3.2202	11.68%	2.6602	-7.74%	2.8835
167 °C	3.3486	7.98%	3.5234	13.62%	3.8564	24.36%	3.1011
177 °C	3.5718	7.63%	3.5606	7.29%	3.3951	2.30%	3.3186
187 °C	3.4713	-1.83%	3.5774	1.17%	3.4937	-1.19%	3.5359
197 °C	3.3951	-9.54%	3.4565	-7.90%	3.4620	-7.75%	3.7530

Table 5.2b. Comparison of the ECLT model initial dome height predictions to actuators cured at various temperatures.

	Actuator 1		Actuator 2		Actuator 3		
	Height (mm)	Diff	Height (mm)	Diff	Height (mm)	Diff	ECLT Model
157 °C	3.0528	34.54%	3.2202	41.92%	2.6602	17.24%	2.2691
167 °C	3.3486	35.15%	3.5234	42.21%	3.8564	55.65%	2.4776
177 °C	3.5718	32.56%	3.5606	32.14%	3.3951	26.00%	2.6945
187 °C	3.4713	19.01%	3.5774	22.64%	3.4937	19.77%	2.9169
197 °C	3.3951	8.04%	3.4565	9.99%	3.4620	10.17%	3.1425

Table 5.2c. Comparison of the CLT model predictions of the slope of the hysteresis loop to actuators cured at various temperatures

	Actuator 1		Actuator 2		Actuator 3		
	Slope (dh/dE)	Diff	Slope (dh/dE)	Diff	Slope (dh/dE)	Diff	CLT Model
157 °C	0.3665	53.11%	0.3051	27.46%	0.3804	58.94%	0.2394
167 °C	0.3600	50.52%	0.3339	39.63%	0.2837	18.62%	0.2392
177 °C	0.3004	25.73%	0.3004	25.74%	0.2902	21.45%	0.2390
187 °C	0.3432	43.78%	0.3590	50.40%	0.3274	37.15%	0.2387
197 °C	0.3070	28.71%	0.2958	24.03%	0.3023	26.76%	0.2385

Table 5.2d. Comparison of the ECLT model predictions of the slope of the hysteresis loop to actuators cured at various temperatures

	Actuator 1		Actuator 2		Actuator 3		
	Slope (dh/dE)	Diff	Slope (dh/dE)	Diff	Slope (dh/dE)	Diff	ECLT Model
157 °C	0.3665	19.33%	0.3051	-0.66%	0.3804	23.88%	0.3071
167 °C	0.3600	16.70%	0.3339	8.25%	0.2837	-8.03%	0.3085
177 °C	0.3004	-2.17%	0.3004	-2.17%	0.2902	-5.50%	0.3071
187 °C	0.3432	12.93%	0.3590	18.13%	0.3274	7.72%	0.3039
197 °C	0.3070	2.38%	0.2958	-1.34%	0.3023	0.83%	0.2998

The previous figures and tables illustrate the prediction capabilities of both the CLT and ECLT models. Both the CLT and the ECLT models predicted a different initial dome height for each different temperature, but the predicted dome height displacements remained the same. The CLT model more closely predicted the initial dome height for this layup, while the change in dome height with applied electric field was more closely modeled by ECLT. As the temperature increased beyond the manufacturer's recommended curing temperature the actuators did not have any further increase in dome height due thermal expansion. This caused the CLT model to initially under-predict at lower cure temperatures while over-predicting at the higher cure temperatures. The ECLT model always under-predicted, but became closer to the measured values at the higher temperatures. Both models predicted a linear change in initial dome height with the change in cure temperature.

5.2 Force Output

By restricting the displacement of an actuator a force will be produced. Eight ECLIPSE actuators were tested to determine their force output performance. To measure the force output of a constrained actuator, each ECLIPSE actuator was placed in a four-point bending apparatus. The actuator was held in displacement control while the electric field was increased and the force was measured. A schematic of the experimental setup is found in Figure 5.6.

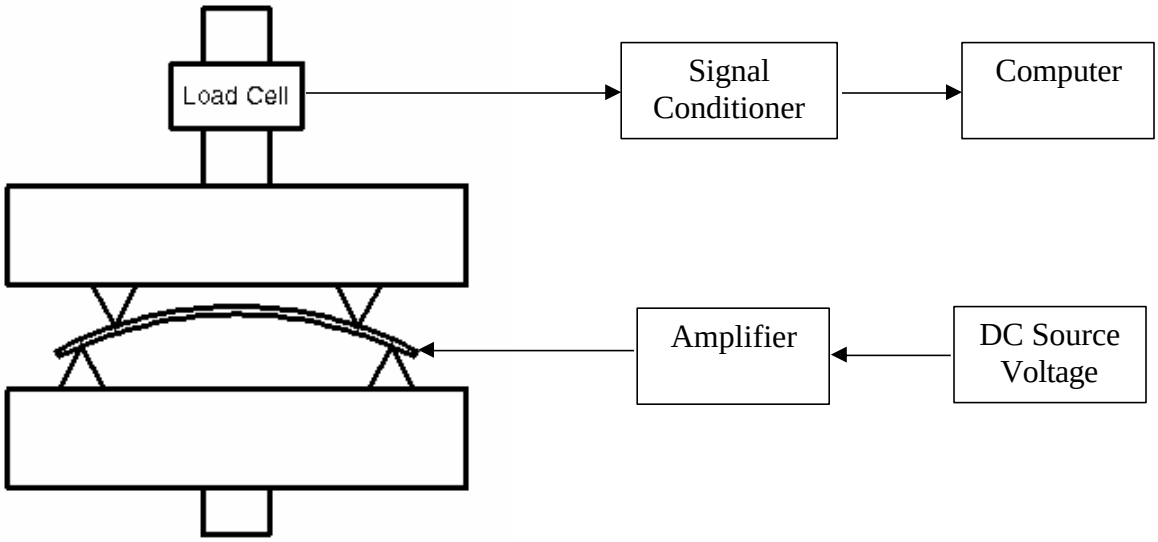

Figure 5.6. Force measurement experimental setup

The actuators tested had the same length and width, but the layups were altered by adding or changing the stacking order to create a different compressive force on the PZT plate. The layups considered were $[90_2/PZT/90_2/0]$ and $[90_3/PZT/90_2/0_2]$. Prior to testing, their initial dome heights and dome height displacements, under the maximum electric field, were measured with a LVDT. The same measurements were taken again after the four-point bending test and both were compared to ensure that there was no damage done during test. There was no change in displacements due to the four-point bend testing.

To hold the actuator securely in the testing device a slight preload was required to ensure that the actuator did not slip prior to testing. To determine if this preload had any effect of the net force output of the actuators, different preloads were used and force output measured for a trial actuator. As seen in Figure 5.7, the amount of preloading had an effect on the net force. By increasing the amount of initial force, the net force output of the actuator increased by approximately 0.5 N for every additional 1 N preload force.

To minimize this effect, the preload used during testing was keep as small as possible while still securely holding the actuator in the fixture. The preload used during experimentation was 1 N. Also to be noted is during the 0 N preload test there is a section between 0 and 150 V where there is no load increase with increase in applied voltage. This is due to the testing grips not being securely in contact with the actuator, which allowed movement prior to the registering of force.

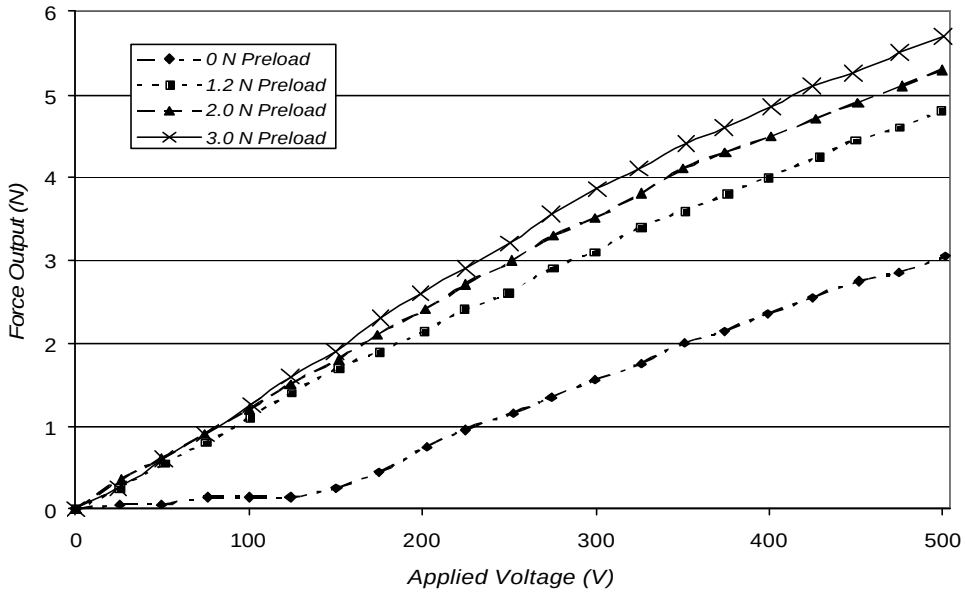

Figure 5.7. Preloading effect.

To test the effect of the grip spacing of the four-point bending apparatus, two actuator layups were tested with the grips at different widths. The layups considered were $[90_2/PZT/90_2/0]$ and $[90_3/PZT/90_2/0_2]$. Force was measured with the grips at a spacing of 5mm and 15mm apart. A schematic is shown in Figure 5.8 that illustrates the experimental setup.

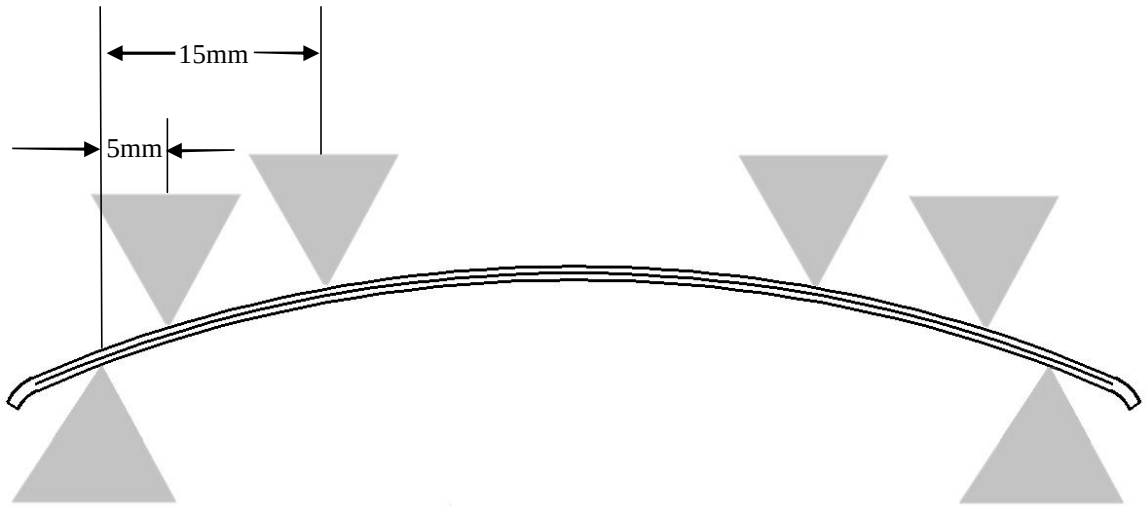

Figure 5.8. Experimental setup illustrating grip spacing.

The force measurement results are seen in Figure 5.9a and 5.9b. It can be seen from these figures that the spacing of the grips has an effect on the force output of the actuators. The actuators had a decrease in the force produced when the grips were spaced at 15mm instead of 5mm. This result was expected. Moment is the cross product of the moment arm and the force that acts perpendicular to it. The actuators produce a fixed amount of moment. As the grips are place further apart and the moment arm increases, less force is required from the grips to counteract the moment force produced by the actuator.

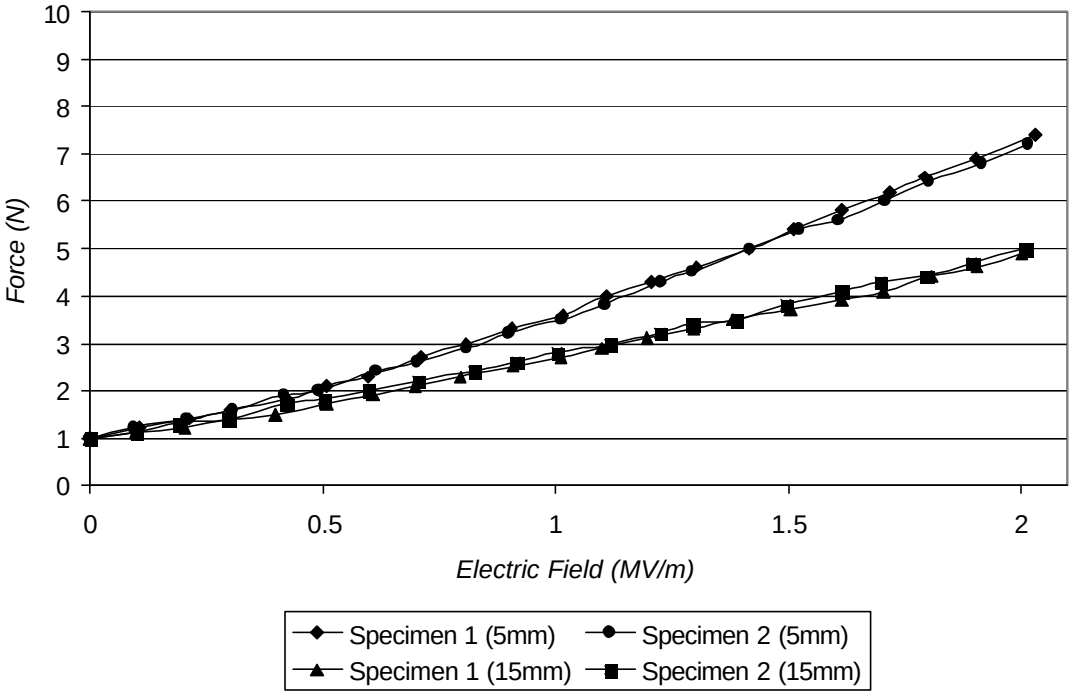

Figure 5.9a. Force produced with varying electric field in a four-point bending apparatus for a $[90_2/PZT/90_2/0]$ layup.

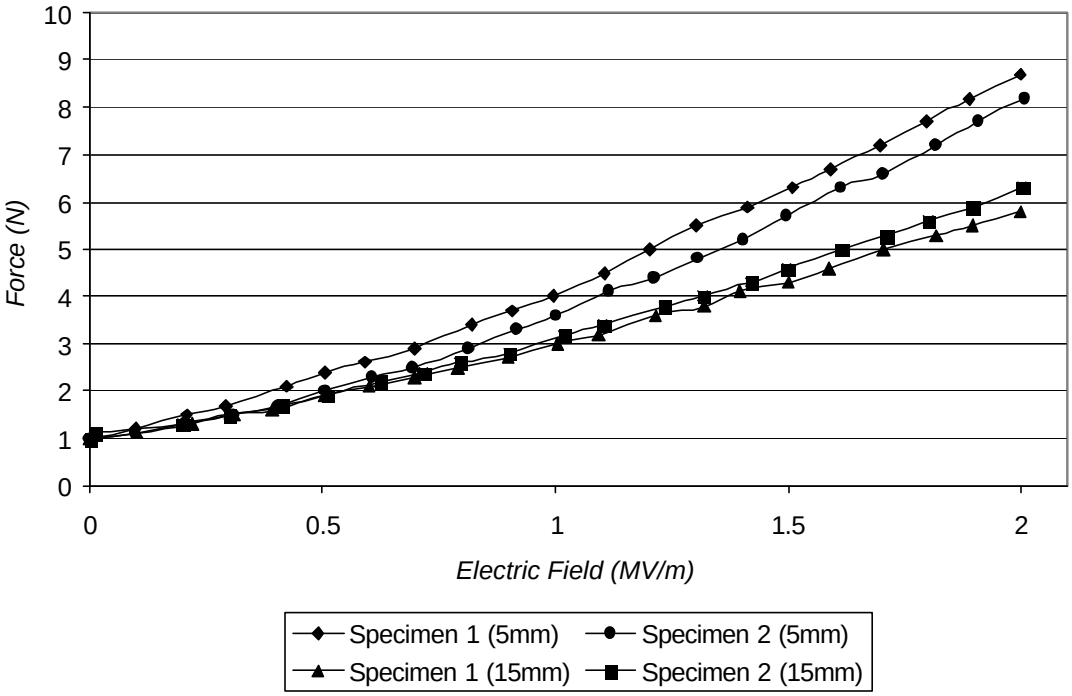

Figure 5.9b. Force produced with varying electric field in a four-point bending apparatus for a $[90_3/PZT/90_2/0_2]$ layup.

The theoretical moment produced by the actuators was modeled by CLT and ECLT. Both models predicted the same moments. For simplification, the actuators were assumed to be straight. Figures 5.10a and 5.10b show the theoretical force produced by the actuators which is calculated from the theoretical mo ment values given by the models.

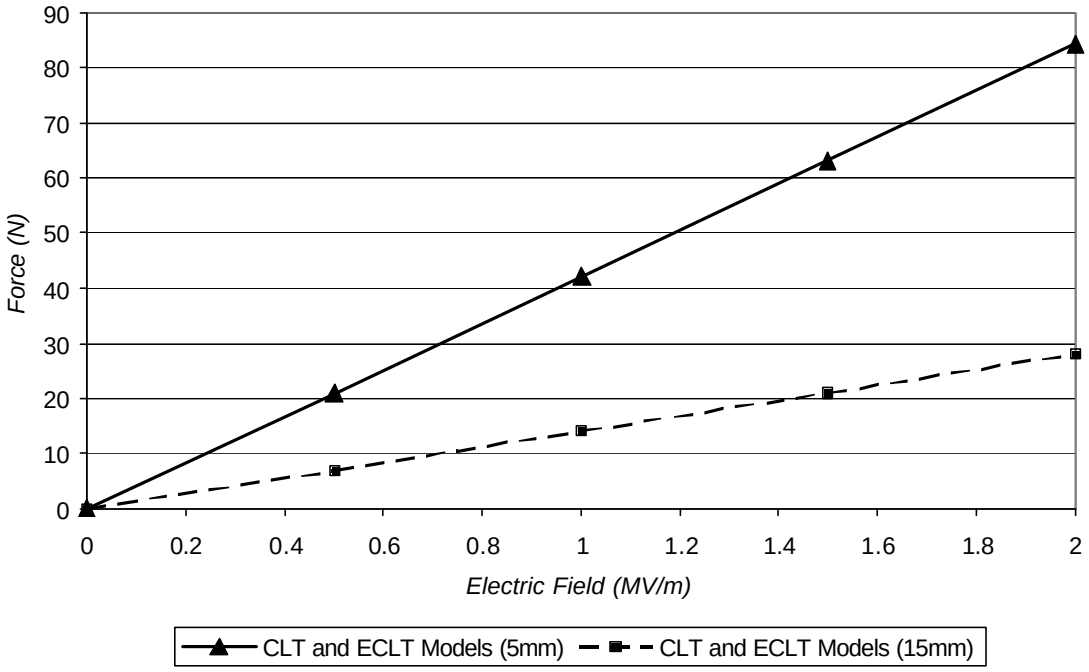

Figure 5.10a. Theoretical force produced with varying electric field in a four-point bending apparatus for a [90_2/PZT/90_2/0] layup.

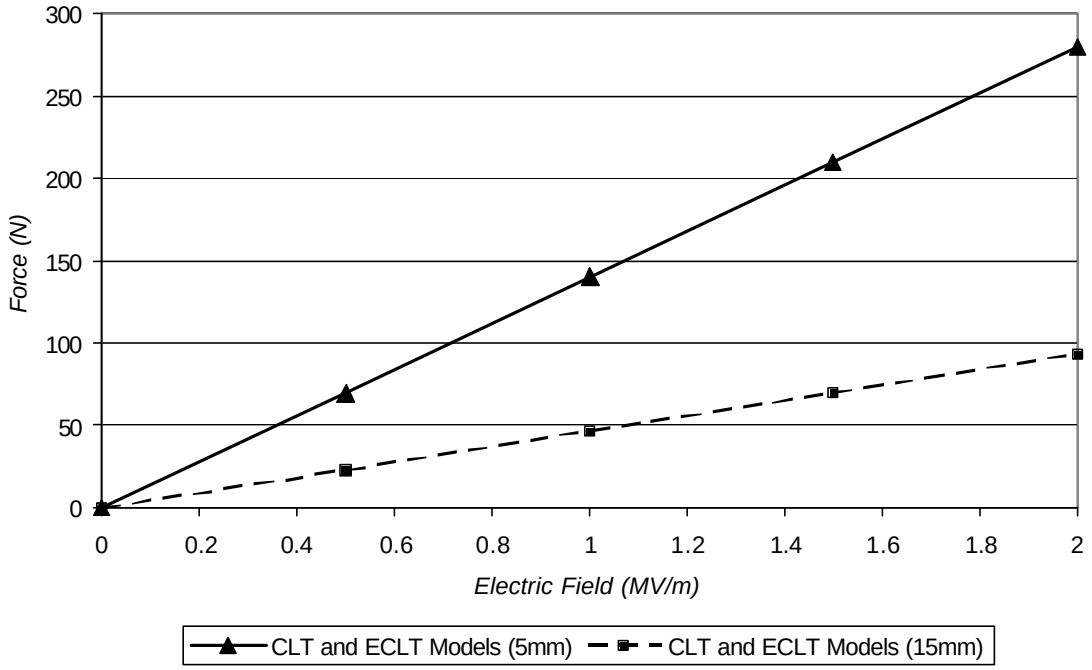

Figure 5.10b. Theoretical force produced with varying electric field in a four-point bending apparatus for a $[90_3/PZT/90_2/0_2]$ layup.

The theoretical calculations do not agree with the measured data. The measured data for the $[90_2/PZT/90_2/0]$ layup is lower then the theoretical predictions by a factor of 11 for the 5mm spacing and a factor of 6 for the 15mm spacing at 2 MV/m. The measured data for the $[90_3/PZT/90_2/0_2]$ layup is lower then the theoretical predictions by a factor of 33 for the 5mm spacing and by a factor of 16 for the 15mm spacing at 2MV/m. Four-point bending is not a good measure of the blocked force for actuators. Actuators produce a fixed amount of moment, independent of the grip spacing. The moments produced by the same actuator at different grip spacing were compared and do not agree. While in the four-point bending apparatus, the entire actuator was not completely constrained. The center section was free to displace. This movement required energy and reduced the amount of force available. Plies with 0^0 fibers are

stiffer in bending then plies with 90^o fibers. The results show that the layup with more 0^o plies was further from the predicted results. Additionally, as the length of the center section was decreased the measured values became closer to the predicted values. Both of these indicate that the displacement of the center section reduced the available force.

5.3 Actuator Fatigue

ECLIPSE actuators were tested to determine their high cycle performance. Incorporating actuators into an engineered structure necessitates understanding the behavior of ECLIPSE actuators after a number of cycles. ECLIPSE actuators were characterized in two different conditions: free displacement under resonant and half-resonance frequencies and in four-point bending.

5.3.1 Free Displacement Fatigue

Twelve ECLIPSE actuators were tested in a free displacement condition to determine their high cycle performance. Each ECLIPSE actuator was cantilevered with fixed-free boundary conditions and cycled from zero electric field to maximum electric field for at least one million cycles. The actuators were not allowed to rest on the table during cycling because at frequencies above 10 Hz they begin to rebound and could damage themselves. The maximum displacement was measured at 0, 100, 1000, 10000, 100000, and 1000000 cycles. A decrease in displacement would be indicative of damage in the actuator. The displacement was measured at the free end with the actuator clamped in the fixture at the other end. Figure 5.11 shows the testing and measurement setup. Each actuator was positioned such that the point of measurement on the actuator

was parallel with the flat surface the fixture holding the actuator was resting on. Using the relationship in Equation (4.2) and Equation (5.1), the height difference, *y*, between the ends of the actuator could be found to ensure a flat measurement surface.

$$y = r[1 - \sin(\frac{p}{2} - q)] \tag{5.1}$$

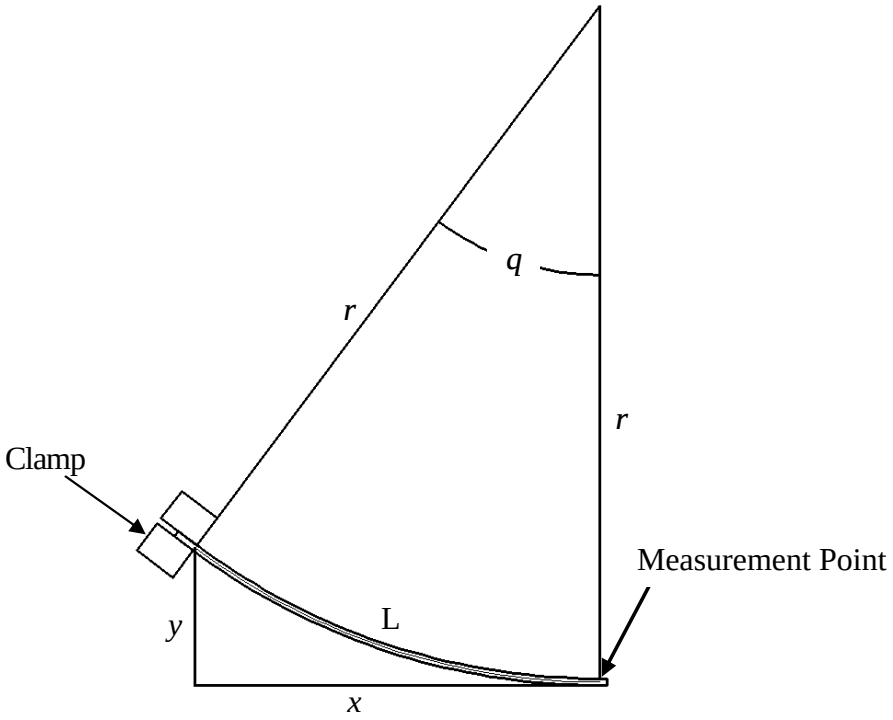

Figure 5.11. Fatigue testing and measurement setup.

The layup considered was $[90_3/PZT/90_2/0_2]$. Six actuators were tested in total. Prior to testing, the resonant frequency of each actuator was measured with a laser doppler vibrometer. The frequency where the maximum displacement occurred during cycling between zero and full scale electric field was defined as the resonant frequency for that actuator. Three specimens were tested at their resonant frequency and three

specimens were tested at one half their resonant frequency. Table 5.3 shows the measured resonant frequencies for each tested actuator.

Table 5.3. Measured resonant frequencies for six samples of ECLIPSE actuators.

Layup	Measured Resonant Frequencies (Hz)
$[90_2/PZT/90/0_2]$	54, 56, 58, 60, 66, 71

The actuators tested did not appear to show a change in the displacement after fatigue cycling at the half resonant or resonant frequency. No statistical analysis was done on these specimens, so there is no confidence interval associated with the presented data. Figure 5.12a and 5.12b show the maximum displacement measured at certain cycles for the half resonant and resonant frequency tests, respectively. There are variations in the displacement shown in the results. These variations can be due to moisture absorption, UV degradation, or micro-cracking, but are most likely due to experimental measurement inaccuracies.

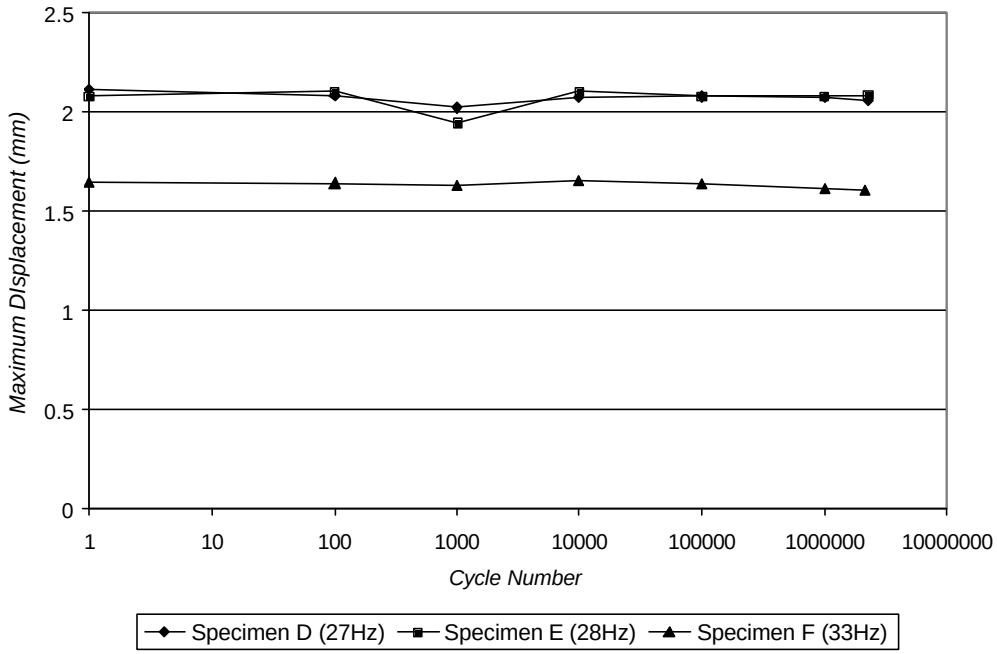

Figure 5.12a. Maximum displacement after cycling at one half resonant frequency.

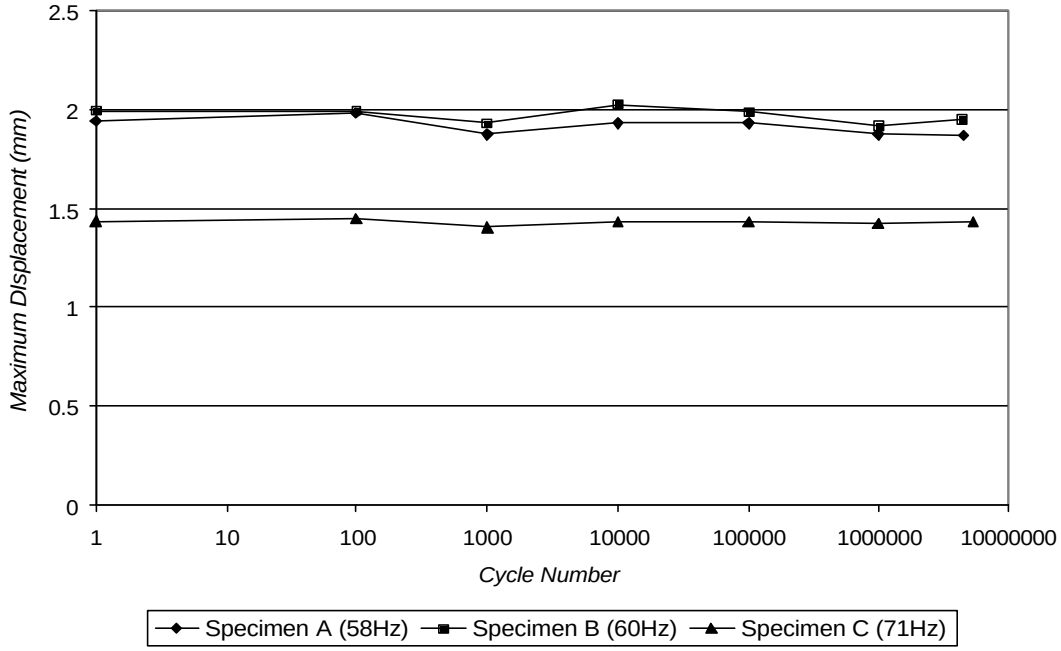

Figure 5.12b. Maximum displacement after cycling at resonant frequency.

The minor hysteresis loop for each actuator was also examined before and after fatigue cycling. There was no difference between the hysteresis loops initially and after the millionth cycle. Figure 5.13 shows an example of the comparison of hysteresis loops for an actuator tested at the resonant frequency.

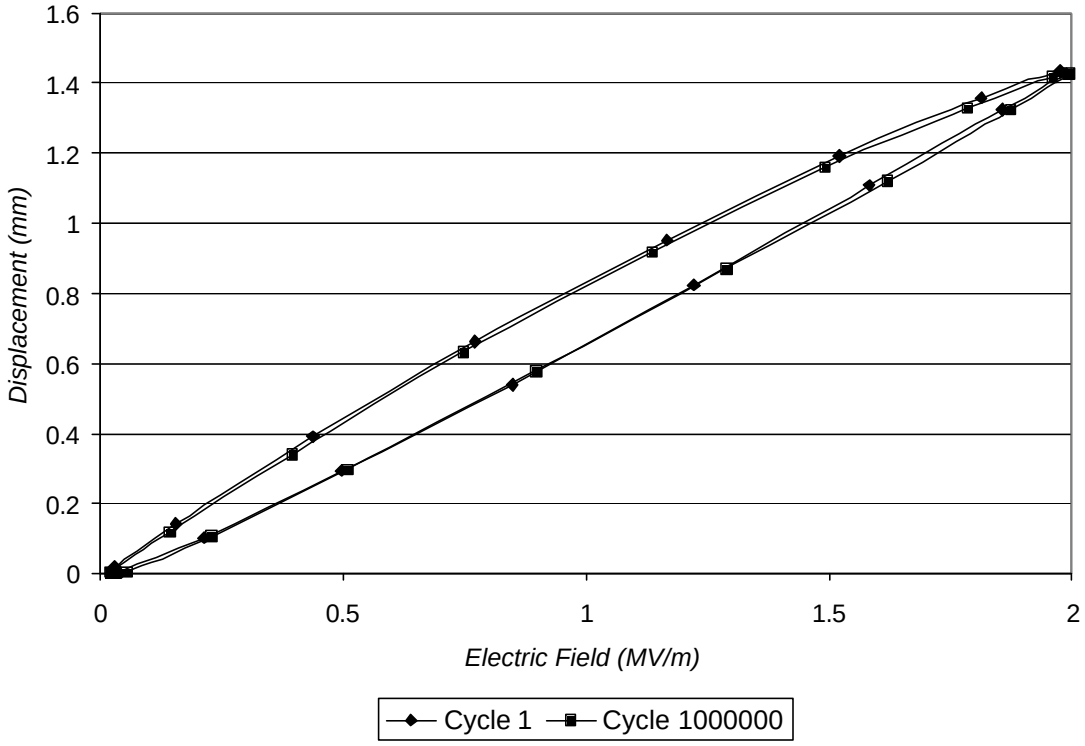

Figure 5.13. Minor hysteresis loop for actuator tested at resonant frequency.

5.3.2 Four-Point Bending Fatigue

An ECLIPSE actuator was tested in a four-point bending apparatus to determine the force output capabilities after a number of cycles. An actuator with a $[90_2/PZT/90_2/0]$ layup was tested at a frequency of $1/10^{th}$ Hz under a zero to full scale cyclic electric field. The test setup is shown previously in Figure 5.6. Figure 5.14 shows the maximum force produced by the actuator after a total of 5500 cycles. Each point in Figure 5.14 is the average of five points. The point for the first cycle is the average of cycles one through five and all of the other data points are the average of the two cycles before and two cycles after the list cycle number. This figure shows that there is a decrease in the force output capabilities after repeated cycling in the four-point bending apparatus. There was no statistical analysis done, therefore there is no

confidence interval associated with this data. Factors could have changed the results include moisture absorption, UV light degradation, and micro-cracking in composite or PZT material. No particular damage mechanism was singled out as the cause of the decrease in force output performance.

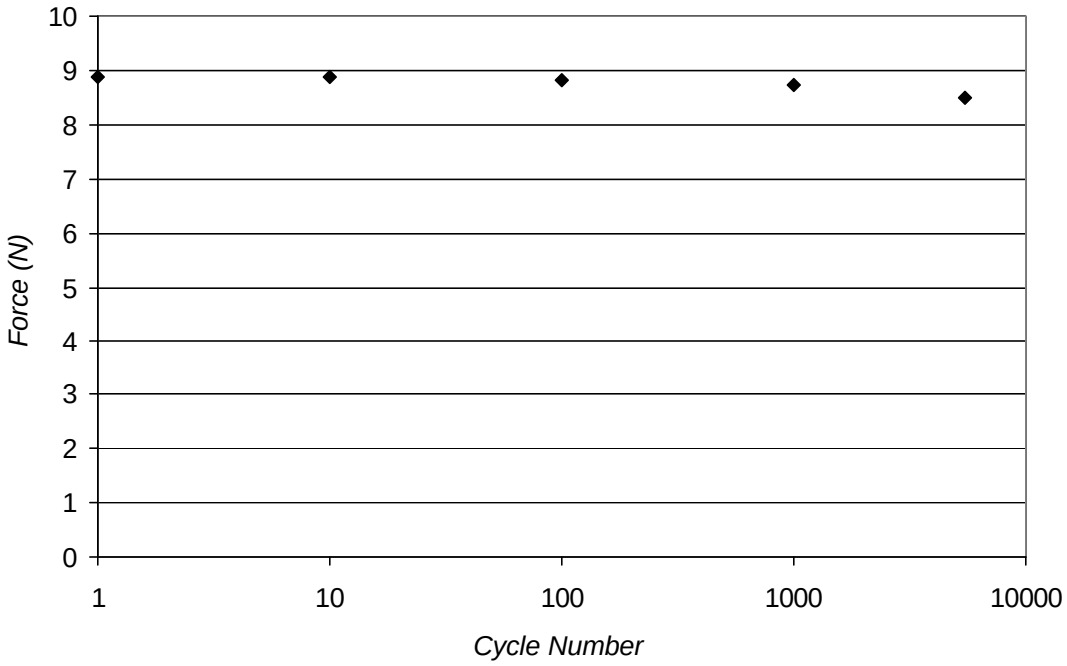

Figure 5.14. Force produced by actuator after cycling.

CHAPTER 6

CONCLUSIONS AND RECOMMENDATIONS

This work progressed the understanding of unimorph composite actuator behavior under various conditions. Actuator design was improved over previous generations by eliminating extraneous composite material. This reduced the weight of the actuator and brought the measured actuator curvatures closer to those predicted. In addition, a miniature-autoclave was created that has the capability to produce multiple actuators daily without the expense of a full scale autoclave. This allowed actuators to be built locally, prepared, and tested daily.

An alternative model to the classical lamination theory model previously presented was introduced to predict actuator behavior. The extended classical lamination theory model began to explain the non-linear behavior of unimorph actuators due to large out of plane deflections. Both models presented were used to design actuators with the PZT material in residual compression. The curvatures were also calculated and compared to the displacements measured by the LVDT. The CLT model was shown to predict the initial dome height more accurately then the ECLT model. The ECLT model under-predicted the initial curvature but more accurately predicted the dome height change with increasing electric field then the CLT model.

Actuator behavior was further characterized under various conditions. The actuators tested in this study were made from a Kevlar 49/epoxy composite. This composite material has limitations which include moisture absorption and UV sensitivity. Actuators were allowed to remain in a dark environment with access to atmospheric air to determine their performance with absorbed moisture. The actuators showed that there

was no decrease in performance with small amounts of moisture absorbed into the composite. The sensitivity of Kevlar was also tested by curing actuators at various temperatures. It was shown that for the composite material used, no additional curvature can be obtained by curing the composite at a temperature above the manufacturer's recommendation. CTS 3195HD was the PZT material used in the actuators. Actuators were tested to determine where failure occurred. It was shown that while there was no definitive failure point, the actuators could be driven to a voltage higher then the recommended maximum voltage without fear of the PZT material failing. Further, the actuator was shown to react linearly throughout the entire range of applied voltages without saturating. Previous generations of actuators were equipped with a PZT material that would saturate at approximately 30% of the recommended voltage creating non-linearities in the displacement response.

By restricting the displacement of these actuators a force will be produced. The force output of the actuators was measured by using a four-point bending apparatus. Various layups were tested to determine what the force capabilities were and whether there is a difference in force output between layups. It was found that the actuators with a PZT layer in a higher residual compressive state created more force.

The fatigue behavior of these devices was also examined. Two different loading conditions were considered. The first loading condition allowed one end of the actuator to move freely while the other was clamped. The resonant frequency of the actuator was measured with a LDV. One set of specimens was cycled at the measured resonant frequency while another set was cycled at one half the measured resonant frequency. It was shown that the there was no decrease in displacement or shape of the minor

hysteresis loop after a high number of cycles for either tested frequency. The second loading condition measured the force output of the actuator after a high number of cycles. It was shown that there was no decrease in actuator force capabilities due to cycling as well. These results strongly suggest that there were no interlaminate debonding, cracking the matrix, or cracking of the PZT material.

Additional work is required to further advance unimorph composite actuators. Other composite materials should be investigated to further refine the actuators performance. Kevlar 49 fiber has drawbacks that can limit the performance of the actuators. By selecting other materials without these shortcomings the actuators could perform better. Additionally, determining more accurate displacement approximations for the ECLT model would prove useful to modeling. Because these actuators could be useful to control the vibrations in a large cylindrical body, further investigation into the moment and force output would be necessary.

APPENDIX A

STRAIN EQUATIONS FROM KIRCHHOFF HYPOTHESIS

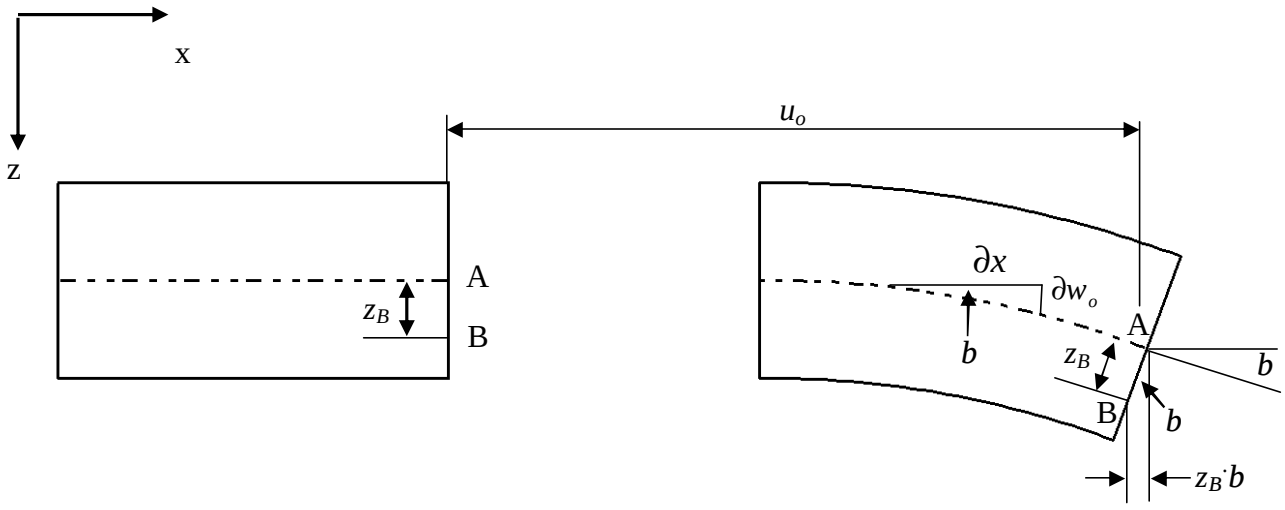

The displacement of point A in the *x*-direction from the undeformed body to the deformed body is u_o. Point A is located along the centerline of the panel, while point B is some distance, z_B, from the centerline in the *z*-direction. From assumptions (ii) and (iii) for CLT, which state that lines originally perpendicular to the middle surface remain perpendicular and retain their length after deformation, and the approximation for small angles ($\sin(\theta) \approx \theta$), the displacement at point B in the *x*-direction follows the form in Equation (A1).

$$u_B = u_o - z_B b \tag{A1}$$

Equation (A2) shows the relationship for the slope of the midplane surface of the laminate, b.

$$b = \frac{\partial w_o}{\partial x} \tag{A2}$$

The displacement for point B in the *x*-direction can be found by combining Equation (A1) and Equation (A2).

$$u = u_o - z \frac{\partial w_o}{\partial x} \tag{A3}$$

The displacement in the *y*-direction can also be found by similar reasoning.

$$v = v_o - z\frac{\partial w_o}{\partial y} \tag{A4}$$

The laminate strains have been reduced to ε_{xx}, ε_{yy}, and γ_{xy} by assumptions (iii) and (iv). Equation (A5) shows the strains equations in terms of displacements for small strains.

$$\begin{aligned} e_{xx} &= \frac{\partial u}{\partial x} \\ e_{yy} &= \frac{\partial v}{\partial y} \\ g_{xy} &= \frac{\partial u}{\partial y} + \frac{\partial v}{\partial x} \end{aligned} \tag{A5}$$

Substituting equations (A3), (A4), and (A5) yields the strain equations used in CLT.

$$\begin{aligned} e_{xx} &= \frac{\partial u_o}{\partial x} - z\frac{\partial^2 w_o}{\partial x^2} \\ e_{yy} &= \frac{\partial v_o}{\partial y} - z\frac{\partial^2 w_o}{\partial y^2} \\ g_{xy} &= \frac{\partial u_o}{\partial y} + \frac{\partial v_o}{\partial x} - 2z\frac{\partial^2 w_o}{\partial x \partial y} \end{aligned} \tag{A6}$$

where the midplane strains are

$$\begin{aligned} e^{o}_{xx} &= \frac{\partial u_o}{\partial x} \\ e^{o}_{yy} &= \frac{\partial v_o}{\partial y} \\ g^{o}_{xy} &= \frac{\partial u_o}{\partial y} + \frac{\partial v_o}{\partial x} \end{aligned} \tag{A7}$$

and the curvatures are

$$k_{xx} = -\frac{\partial^2 w_o}{\partial x^2}$$
$$k_{yy} = -\frac{\partial^2 w_o}{\partial y^2} \qquad \text{(A8).}$$
$$k_{xy} = -2\frac{\partial^2 w_o}{\partial y^2}$$

APPENDIX B

CLT COMPUTER PROGRAM

```
%Author: Kyle Webber

%Date: 12/15/03

%Purpose: A program to find the stresses and strains in a
%         composite structure of an arbitrary lay-up, with
%         or without an embedded piezoelectric material.


%Assumptions: Classical Lamination Theory
%             Plane Stress assumption (sigma_zx = sigma_zy
%             = sigma_zz  = e_zx = e_zy = 0)


%Input: Material properties, lay-up, electric field,
%       dimensions, and temperature.

%Output: Qbar, plots of stress and strain in the x and y
%        directions, dome height using CLT, dome height
%        using Hyers papers.

clear

A=0; B=0; D=0; nt=0; mt=0; nn=0; m=0; ne=[0;0;0];
me=[0;0;0]; r=0; j=0; g=0; k=0; posx=0; negx=0; posy=0;
negy=0; a=0; b=0; c=0; d=0;

n = input('How many layers is the composite? ');
Lx = input('What is the length of the laminate (mm)? ');
E = input('What is the applied electric field (V/m)? ');
temp = input('What is the temperature change (Celsius)? ');
num = input('From the bottom of the lay-up, which number
ply is the PZT (If no PZT, enter 0)? ');

input('The following inputs are from the bottom ply to the
top ply. Please press enter.')

z(1) = 0;

 for i = 1:n;
     fprintf('\n')
     fprintf('Input material properties for layer %d\n',i);
     E0(i) = input('What is E11 of this ply (Pa)? ');
     E90(i) = input('What is E22 of this ply (Pa)? ');
     G12(i) = input('What is the shear modulus of this
        ply (Pa)? ');
     Nu12(i) = input('What is v12 of this ply? ');
```

```
     Nu21(i) = Nu12(i)*(E90(i)/E0(i));
     alpha1(i) = input('What is the thermal expansion
        parallel to the fibers (1/C)?');
     alpha2(i) = input('What is the thermal expansion
        perpendicular to the fibers (1/C)? ');
     Theta(i) = input('What is the angle of this ply; if
        PZT layer enter 0 (radians)?  ');
     t(i) = input('How thick is the ply (mm)? ');

     z(i+1)=z(i) + (t(i)/1000);
 end

for i = 1:n;

h(1)=-(z(n+1)/2);
h(i+1)=z(i+1)-(z(n+1)/2);

%defining material properties for CTS 3195HD PZT
   d31=-190e-12;
   d32=d31;
   d33=390e-12;

%transforming the thermal expansions
alphax(i) = alpha1(i)*((cos(Theta(i)))^2) + alpha2(i)
   *((sin(Theta(i)))^2);

alphay(i) = alpha2(i)*((cos(Theta(i)))^2) + alpha1(i)
   *((sin(Theta(i)))^2);

alphaxy(i) = (2*cos(Theta(i))*sin(Theta(i)))*(alpha1(i)-
   alpha2(i));

%solving for the stiffness coefficients
Q11(i) = E0(i)/(1-(Nu12(i)*Nu21(i)));
Q22(i) = E90(i)/(1-(Nu12(i)*Nu21(i)));
Q12(i) = (Nu12(i)*E90(i))/(1-(Nu12(i)*Nu21(i)));
Q66(i) = G12(i);

%solving for the transformed reduced stiffness matrix
Q11bar(i) = Q11(i)*(cos(Theta(i))^4))+(2*(Q12(i)+
   (2*Q66(i)))*((sin(Theta(i)))^2)*((cos(Theta(i)))^2))
   +(Q22(i) *(sin(Theta(i)))^4);

Q12bar(i) = ((Q11(i)+Q22(i)-4*Q66(i))*((sin(Theta(i)))^2)*
   ((cos(Theta(i)))^2))+(Q12(i)*(((sin(Theta(i)))^4)+
   ((cos(Theta(i)))^4)));
```

```
Q22bar(i)=(Q11(i)*(sin(Theta(i))^4))+(2*(Q12(i)+(2*Q66(i)))
   *((sin(Theta(i)))^2)*((cos(Theta(i)))^2))+(Q22(i)*
   (cos(Theta(i)))^4);

Q16bar(i) = ((Q11(i)-Q12(i)-2*Q66(i))*sin(Theta(i))*
   ((cos(Theta(i)))^3))+((Q12(i)-Q22(i)+2*Q66(i))*
   cos(Theta(i)) *((sin(Theta(i)))^3));

Q26bar(i) = ((Q11(i)-Q12(i)-2*Q66(i))*cos(Theta(i))*
   ((sin(Theta(i)))^3))+((Q12(i)-Q22(i)+2*Q66(i))*
   sin(Theta(i))*((cos(Theta(i)))^3));

Q66bar(i) = ((Q11(i)+Q22(i)-2*Q12(i)-2*Q66(i))*
   ((sin(Theta(i)))^2)*((cos(Theta(i)))^2))+
   (Q66(i)*(((sin(Theta(i)))^4)+((cos(Theta(i)))^4)));

Qbar = [Q11bar(i) Q12bar(i) Q16bar(i); Q12bar(i) Q22bar(i)
   Q26bar(i); Q16bar(i) Q26bar(i) Q66bar(i)];

%normal forces due to electric field
if i == num
   ne = (Qbar)*[d31;d31;0]*(h(num+1)-h(num))*E;
end

%normal force due to thermal change
nt = nt + (((Qbar)*[alphax(i);alphay(i);alphaxy(i)])
   *temp*(h(i+1)-h(i)));

%Neglecting external forces

%moment force due to electric field
if i == num
   me = 0.5*(Qbar)*[d31;d31;0]*(((h(num+1))^2)-
        ((h(num))^2))*E;
end

%moment due to thermal change
mt = mt + ((0.5*(Qbar)*[alphax(i);alphay(i);alphaxy(i)])
   *(((h(i+1))^2)-((h(i))^2))*temp);

%Neglecting external moments

%Calculating laminate stiffnesses
A = A + (Qbar*((h(i+1)-h(i))));
B = B + ((1/2)*(Qbar)*(((h(i+1))^2)-((h(i))^2)));
D = D + ((1/3)*(Qbar)*(((h(i+1))^3)-((h(i))^3)));
```

```
end


F = [A B
     B D];

H = inv(F);

nn = ne+nt;
m = me+mt;

   NM = [nn;m];
   ek = H*NM;
   eox = ek(1);
   eoy = ek(2);
   eoxy = ek(3);
   kx = ek(4);
   ky = ek(5);
   kxy = ek(6);

   rhox = 1/ek(4);
   rhoy = 1/ek(5);

hx = rhox*1000*(1-cos(Lx/(2000*rhox)));

disp('The dome height of the actuator as determined by CLT
is [mm]') ;disp(abs(hx))

%plotting the strains over the thickness
   for q = h(1)*1000:.01:-h(1)*1000
           g = g+1;
           r(g) = q/1000;
           ex(g) = (r(g)/rhox+eox)*1e6;
           ey(g) = (r(g)/rhoy+eoy)*1e6;
   end


%Plot of strains in x-direction
   figure
   plot(ex,r*1000,'r')
   hold on

   for i = 1:n;
           plot([ex(1) ex(g)],[h(i) h(i)]*1000)
   end

    plot([ex(1) ex(g)],[h(n+1) h(n+1)]*1000)
```

```
    xlabel('Epsilon_x_x (um/m)')
    ylabel('Thickness (mm)')


%Plot of strains in y-direction
   figure
   plot(ey,r*1000,'g')
   hold on

   for i = 1:n;
           plot([ey(1) ey(g)],[h(i) h(i)]*1000)
   end

    plot([ey(1) ey(g)],[h(n+1) h(n+1)]*1000)
    xlabel('Epsilon_y_y (um/m)')
    ylabel('Thickness (mm)')


%Plotting the stresses in each ply.
%Since the lines for the stresses in each ply connect
%to one another, a loop is being used.
%The number of data points in each layer is increased and
%the points merge into a line.

resolution = 0.001;

%Plotting the stresses over the thickness
for i = 1:n
   for v = h(i+1)*1000:-resolution:h(i)*1000
       k = k+1;
       j(k) = v/1000;

       if i == num
          sigmax(k)=([Q11bar(i) Q12bar(i) Q16bar(i)]*
          [eox;eoy;eoxy]+[Q11bar(i) Q12bar(i) Q16bar(i)]*
          j(k)*[kx;ky;kxy]-[Q11bar(i) Q12bar(i) Q16bar(i)]
          *[alphax(i);alphay(i);alphaxy(i)]*temp-[Q11bar(i)
          Q12bar(i) Q16bar(i)]*[d31;d31;0]*E)/1e6;

          sigmay(k)=([Q12bar(i) Q22bar(i) Q26bar(i)]*
          [eox;eoy;eoxy]+[Q12bar(i) Q22bar(i) Q26bar(i)]
          *j(k)*[kx;ky;kxy]-[Q12bar(i) Q22bar(i) Q26bar(i)]
          *[alphax(i);alphay(i);alphaxy(i)]*temp-[Q12bar(i)
          Q22bar(i) Q26bar(i)]*[d31;d31;0]*E)/1e6;

       else
          sigmax(k)=(([Q11bar(i) Q12bar(i) Q16bar(i)]*
```

```
            [eox;eoy;eoxy])+([Q11bar(i) Q12bar(i) Q16bar(i)]
            *j(k)*[kx;ky;kxy])-([Q11bar(i) Q12bar(i)
            Q16bar(i)] *[alphax(i);alphay(i);alphaxy(i)]*
            temp))/1e6;

            sigmay(k)=(([Q12bar(i) Q22bar(i) Q26bar(i)]*
            [eox;eoy;eoxy])+([Q12bar(i) Q22bar(i) Q26bar(i)]
            *j(k)*[kx;ky;kxy])-([Q12bar(i) Q22bar(i)
            Q26bar(i)]*[alphax(i);alphay(i);alphaxy(i)]*
            temp))/1e6;
        end

%Checking the equilibrium.  The equilibrium value is not
%exactly zero because of the inexactness of the
%resolution.  As the resolution goes to zero, the
%equilibirum goes to zero.  The trapezoidal rule was used

 if k > 1
   if sigmax(k)>0
    posx = posx + (((sigmax(k)+sigmax(k-1))/2)*resolution);
   else
    negx = negx + (((sigmax(k)+sigmax(k-1))/2)*resolution);
   end

   if sigmax(k)>0
    posy = posy + (((sigmay(k)+sigmay(k-1))/2)*resolution);
   else
    negy = negy + (((sigmay(k)+sigmay(k-1))/2)*resolution);
   end
 end
end
end

  if abs(posx + negx) < 0.1
   disp('Laminate is in equilibrium in x-direction')
  else
   disp('Laminate is not in equilibrium in x-direction')
  end

  if abs(posy + negy) < 0.1
   disp('Laminate is in equilibrium in y-direction')
  else
   disp('Laminate is not in equilibrium in y-direction')
  end

%Plot of stresses in x-direction
figure
```

```
plot(sigmax,j*1000,'r.')
hold on

for i = 1:n;
 plot([min(sigmax) max(sigmax)],[h(i) h(i)]*1000)
end

plot([min(sigmax) max(sigmax)],[h(n+1) h(n+1)]*1000)
 xlabel('Sigma_x_x (MPa)')
 ylabel('Thickness (mm)')


%Plot of stresses in y-direction
figure
plot(sigmay,j*1000,'g.')
hold on

for i = 1:n;
 plot([min(sigmay) max(sigmay)],[h(i) h(i)]*1000)
end

plot([min(sigmay) max(sigmay)],[h(n+1) h(n+1)]*1000)
 xlabel('Sigma_y_y (MPa)')
 ylabel('Thickness (mm)')
```

APPENDIX C

ECLT COMPUTER PROGRAM

```
clear

A=0; B=0; D=0; nt=0; mt=0; nn=0; m=0; ne=[0;0;0];
me=[0;0;0]; r=0; j=0; g=0; k=0; posx=0; negx=0; posy=0;
negy=0; a=0; b=0; c=0; d=0;

%dimensions and stacking order
  n = input('How many layers is the composite? ');
  Lx = input('What is the length of the laminate (mm)? ');
  Ly = input('What is the width of the laminate (mm)? ');
  num = input('From the bottom of the lay-up, which number
               ply is the PZT (If no PZT,enter 0)? ');

%operating and curing conditions
  E = input('What is the applied electric field (V/m)? ');
  temp = input('What is the temperature change (Celsius)?
');

 input('The following inputs are from the bottom ply to the
        top ply. Please press enter.')

z(1)=0;

%material properties for individual actuator plies
 for i=1:n;
    fprintf('\n')
    fprintf('Input material properties for layer %d \n',i);
    E0(i) = input('What is E11 of this ply (Pa)? ');
    E90(i) = input('What is E22 of this ply (Pa)? ');
    G12(i) = input('What is the shear modulus of this ply
(Pa)? ');
    Nu12(i) = input('What is v12 of this ply? ');
    Nu21(i) = Nu12(i)*(E90(i)/E0(i));
    alpha1(i) = input('What is the thermal expansion
parallel to
                       the fibers (1/C)? ');
    alpha2(i) = input('What is the thermal expansion
perpendicular
                       to the fibers (1/C)? ');
    Theta(i)=input('What is the angle of this ply; if PZT
layer
                    enter 0 (radians)?  ');
    t(i)=input('How thick is the ply (mm)? ');
    z(i+1)=z(i) + (t(i)/1000);
    end
```

```
    for i=1:n;

        h(1)=-(z(n+1)/2);
        h(i+1)=z(i+1)-(z(n+1)/2);

      %defining material properties for CTS 3195HD PZT
        d31=-190e-12;
        d32=d31;
        d33=390e-12;
      %transforming the thermal expansions
        alphax(i)=alpha1(i)*((cos(Theta(i)))^2) +
                  alpha2(i)*((sin(Theta(i)))^2);
        alphay(i)=alpha2(i)*((cos(Theta(i)))^2) +
                  alpha1(i)*((sin(Theta(i)))^2);

alphaxy(i)=(2*cos(Theta(i))*sin(Theta(i)))*(alpha1(i)-
                    alpha2(i));

      %solving for the stiffness coefficients
        Q11(i)=E0(i)/(1-(Nu12(i)*Nu21(i)));
        Q22(i)=E90(i)/(1-(Nu12(i)*Nu21(i)));
        Q12(i)=(Nu12(i)*E90(i))/(1-(Nu12(i)*Nu21(i)));
        Q66(i)=G12(i);

      %solving for the transformed reduced stiffness matrix

Q11bar(i)=(Q11(i)*(cos(Theta(i))^4))+(2*(Q12(i)+(2*Q66(i)))
*
          ((sin(Theta(i)))^2)*((cos(Theta(i)))^2))+(Q22(i)*
          (sin(Theta(i)))^4);
Q12bar(i)=((Q11(i)+Q22(i)-4*Q66(i))*((sin(Theta(i)))^2)*
          ((cos(Theta(i)))^2))+(Q12(i)*(((sin(Theta(i)))^4)
          + ((cos(Theta(i)))^4)));
Q22bar(i)=(Q11(i)*(sin(Theta(i))^4))+(2*(Q12(i)+(2*Q66(i)))
*
          ((sin(Theta(i)))^2)*((cos(Theta(i)))^2))
          +(Q22(i)*(cos(Theta(i)))^4);
Q16bar(i)=((Q11(i)-Q12(i)-2*Q66(i))*sin(Theta(i))*
          ((cos(Theta(i)))^3))+((Q12(i)-
Q22(i)+2*Q66(i))*cos(Theta(i))*((sin(Theta(i)))^3));
Q26bar(i)=((Q11(i)-Q12(i)-2*Q66(i))*cos(Theta(i))*
          ((sin(Theta(i)))^3))+((Q12(i)-
Q22(i)+2*Q66(i))*sin(Theta(i))*((cos(Theta(i)))^3));
Q66bar(i)=((Q11(i)+Q22(i)-2*Q12(i)-
2*Q66(i))*((sin(Theta(i)))^2)*
          ((cos(Theta(i)))^2))+(Q66(i)*(((sin(Theta(i)))^4)
     +
```

```
          ((cos(Theta(i)))^4)));

Qbar=[Q11bar(i) Q12bar(i) Q16bar(i); Q12bar(i) Q22bar(i)
Q26bar(i);
      Q16bar(i) Q26bar(i) Q66bar(i)];




     %normal forces due to electric field
         if i==num
         ne=(Qbar)*[d31;d31;0]*(h(num+1)-h(num))*E;
         end

      %normal force due to thermal change
         nt = nt +
(((Qbar)*[alphax(i);alphay(i);alphaxy(i)])
              *temp*(h(i+1)-h(i)));

      %Neglecting external forces

      %moment force due to electric field
         if i==num
         me=0.5*(Qbar)*[d31;d31;0]*(((h(num+1))^2)-
((h(num))^2))*E;
         end



      %moment due to thermal change
         mt = mt +
((0.5*(Qbar)*[alphax(i);alphay(i);alphaxy(i)])
              *(((h(i+1))^2)-((h(i))^2))*temp);

      %Neglecting external moments

      %Calculating laminate stiffnesses
         A = A + (Qbar*((h(i+1)-h(i))));
         B = B + ((1/2)*(Qbar)*(((h(i+1))^2)-((h(i))^2)));
         D = D + ((1/3)*(Qbar)*(((h(i+1))^3)-((h(i))^3)));

    end


        NxE=ne(1);
        NyE=ne(2);
```

```
        NxT=nt(1);
        NyT=nt(2);

        MxE=me(1);
        MyE=me(2);
        MxT=mt(1);
        MyT=mt(2);

        nn=ne+nt;
        m=me+mt;

        A11=A(1,1);
        A12=A(1,2);
        A22=A(2,2);
        B11=B(1,1);
        B12=B(1,2);
        B22=B(2,2);
        D11=D(1,1);
        D12=D(1,2);
        D22=D(2,2);


    syms a b c d real
%first variation of potential energy without electric field
terms
    DUaT=A11*(-b*c/48*Ly^2+a*b^2/1280*Ly^4)+A12*
          (a*b^2/1152*Ly^2*Lx^2-b*d/48*Ly^2-b*c/48*Lx^2)+
          A22*(a*b^2/1280*Lx^4-b*d/48*Lx^2)-B11*(c-
          a*b/24*Ly^2)+B12*(a*b/24*Lx^2+b^2/48*Ly^2-
          d)+B22*(b^2/48*Lx^2)+D11*a+D12*b+NxT*b/48*Ly^2+Ny
          T*b/48*Lx^2+MxT;

    DUbT=A11*(-a*c/48*Ly^2+a^2*b/1280*Ly^4)+A12*(-
a*d/48*Ly^2-
          a*c/48*Lx^2+a^2*b/1152*Ly^2*Lx^2)+A22*(-
          a*d/48*Lx^2+a^2*b/1280*Lx^4)+B11*(a^2/48*Ly^2)-
          B12*(c-a*b/24*Ly^2-a^2/48*Lx^2)-B22*(d-
          a*b/24*Lx^2)+NxT*(a/48*Ly^2)+NyT*(a/48*Lx^2)+D12*
          a+D22*b+MyT;
    DUcT=A11*(c-a*b/48*Ly^2)+A12*(d-a*b/48*Lx^2)-B11*a-
B12*b-NxT;
    DUdT=A12*(c-a*b/48*Ly^2)+A22*(d-a*b/48*Lx^2)-B12*a-
B22*b-NyT;

    %electric field components
    DUaE=NxE*b/48*Ly^2+NyE*b/48*Lx^2+MxE;
    DUbE=NxE*a/48*Ly^2+NyE*a/48*Lx^2+MyE;
```

```
    DUcE=-NxE;
    DUdE=-NyE;

    %total variation
    DUa=DUaT+DUaE;
    DUb=DUbT+DUbE;
    DUc=DUcT+DUcE;
    DUd=DUdT+DUdE;

    [a,b,c,d]=solve(DUa,DUb,DUc,DUd);

    a=double(a);
    b=double(b);
    c=double(c);
    d=double(d);


    %determining whether solution one is usable
    total1=a(1)+b(1)+c(1)+d(1);

    %determining if solution one is stable
    if isreal(total1)==1

C111=A(1,1)*(Ly^4)*(b(1)^2)/1280+A(1,2)*(Ly^2)*(Lx^2)*(b(1)
)^2/1152
     +A(2,2)*(Lx^4)*(b(1))^2/1280+B(1,1)*(Ly^2)*b(1)/24+B(1
     ,2) *(Lx^2)*b(1)/24+D(1,1);
C112=A(1,1)*(-c(1)*(Ly^2)/48+a(1)*(Ly^4)*b(1)/640)+A(1,2)*
     (a(1)*b(1)*(Ly^2)*(Lx^2)/576-d(1)*(Ly^2)/48-
     c(1)*(Lx^2)/48)+A(2,2)*(a(1)*b(1)*(Lx^4)/640-
     d(1)*(Lx^2)/48)+B(1,1)*a(1)*(Ly^2)/24+B(1,2)*
     (a(1)*(Lx^2)/24+b(1)*(Ly^2)/24)+B(2,2)*b(1)*
     (Lx^2)/24+D(1,2)+NxT*temp*(Ly^2)/48+NyT*temp*(Lx^2)/48
;
C113=-A(1,1)*b(1)*(Ly^2)/48-A(1,2)*b(1)*(Lx^2)/48-B(1,1);
C114=-A(1,2)*b(1)*(Ly^2)/48-A(2,2)*b(1)*(Lx^2)/48-B(1,2);
C122=A(1,1)*(a(1)^2)*(Ly^4)/1280+A(1,2)*(a(1)^2)*(Ly^2)*(Lx
^2)/1152
     +A(2,2)*(a(1)^2)*(Lx^4)/1280+B(1,2)*a(1)*(Ly^2)/24+B(2
     ,2) *a(1)*(Lx^2)/24+D(2,2);
C123=-A(1,1)*a(1)*(Ly^2)/48-A(1,2)*a(1)*(Lx^2)/48-B(1,2);
C124=-A(1,2)*a(1)*(Ly^2)/48-A(2,2)*a(1)*(Lx^2)/48-B(2,2);
C133=A(1,1);
C134=A(1,2);
C144=A(2,2);

    C1=[C111 C112 C113 C114
```

```
        C112 C122 C123 C124
        C113 C123 C133 C134
        C114 C124 C134 C144];

        v1=eig(C1);

        if v1(1)>0
            if v1(2)>0
                if v1(3)>0
                    if v1(4)>0
                        disp('Solution one is stable')
                        eox=c(1);
                        eoy=d(1);
                        eoxy=0;
                        kx=-a(1);
                        ky=-b(1);
                        kxy=0;
                        rhox=1/(a(1));
                        rhoy=1/(b(1));
                    end
                end
            end
        else
            disp('Solution one is unstable')
        end

h=a(1)*(1-cos(Lx/2/a(1))^2)*1000;
disp('The dome height of actuator one is [mm]'); disp(h)

dx=Lx/50;
dy=dx;
m=0;

for x=-Lx/2:dx:Lx/2
   m=m+1;
   xdum(m)=x;
   p=0;
   for y=-Ly/2:dy:Ly/2
      p=p+1;
      ydum(p)=y;
      w1(p,m)=1/2*(a(1)*x^2+b(1)*y^2);
   end
end
figure
surf(xdum,ydum,w1)
xlabel('Lx [mm]')
ylabel('Ly [mm]')
```

```
 zlabel('h [mm]')
 title('Solution One Actuator')

    else
        disp('Solution set one is not a viable solution')
    end

 %determining whether solution two is usable
    total2=a(2)+b(2)+c(2)+d(2);

 %determining if solution two is stable
    if isreal(total2)==1

C211=A(1,1)*(Ly^4)*(b(2)^2)/1280+A(1,2)*(Ly^2)*(Lx^2)*(b(2)
)^2/1152
     +A(2,2)*(Lx^4)*(b(2))^2/1280+B(1,1)*(Ly^2)*b(2)/24+B(1
     ,2) *(Lx^2)*b(2)/24+D(1,1);
C212=A(1,1)*(-c(2)*(Ly^2)/48+a(2)*(Ly^4)*b(2)/640)+A(1,2)*
     (a(2)*b(2)*(Ly^2)*(Lx^2)/576-d(2)*(Ly^2)/48-
     c(2)*(Lx^2)/48)+A(2,2)*(a(2)*b(2)*(Lx^4)/640-
     d(2)*(Lx^2)/48)+B(1,1)*a(2)*(Ly^2)/24+B(1,2)*(a(2)*(Lx
     ^2)/24+b(2)*(Ly^2)/24)+B(2,2)*b(2)*(Lx^2)/24+D(1,2)+Nx
     T*temp*(Ly^2)/48+NyT*temp*(Lx^2)/48;
C213=-A(1,1)*b(2)*(Ly^2)/48-A(1,2)*b(2)*(Lx^2)/48-B(1,1);
C214=-A(1,2)*b(2)*(Ly^2)/48-A(2,2)*b(2)*(Lx^2)/48-B(1,2);
C222=A(1,1)*(a(2)^2)*(Ly^4)/1280+A(1,2)*(a(2)^2)*(Ly^2)*(Lx
^2)/1152
     +A(2,2)*(a(2)^2)*(Lx^4)/1280+B(1,2)*a(2)*(Ly^2)/24+B(2
     ,2) *a(2)*(Lx^2)/24+D(2,2);
C223=-A(1,1)*a(2)*(Ly^2)/48-A(1,2)*a(2)*(Lx^2)/48-B(1,2);
C224=-A(1,2)*a(2)*(Ly^2)/48-A(2,2)*a(2)*(Lx^2)/48-B(2,2);
C233=A(1,1);
C234=A(1,2);
C244=A(2,2);

    C2=[C211 C212 C213 C214
        C212 C222 C223 C224
        C213 C223 C233 C234
        C214 C224 C234 C244];

        v2=eig(C2);

        if v2(1)>0
            if v2(2)>0
                if v2(3)>0
                    if v2(4)>0
                        disp('Solution two is stable')
```

```
                        eox=c(2);
                        eoy=d(2);
                        eoxy=0;
                        kx=-a(2);
                        ky=-b(2);
                        kxy=0;
                        rhox=1/(a(2));
                        rhoy=1/(b(2));
                    end
                end
            end
        else
            disp('Solution two is unstable')
        end

h=a(2)*(1-cos(Lx/2/a(2))^2)*1000;
disp('The dome height of actuator two is [mm]'); disp(h)

dx=Lx/50;
dy=dx;
m=0;

for x=-Lx/2:dx:Lx/2
   m=m+1;
   xdum(m)=x;
   p=0;
   for y=-Ly/2:dy:Ly/2
      p=p+1;
      ydum(p)=y;
      w2(p,m)=1/2*(a(2)*x^2+b(2)*y^2);
   end
end
figure
surf(xdum,ydum,w2)
xlabel('Lx [mm]')
ylabel('Ly [mm]')
zlabel('h [mm]')
title('Solution Two Actuator')

   else
       disp('Solution set two is not a viable solution')
   end

%determining whether solution three is usable
   total3=a(3)+b(3)+c(3)+d(3);

%determining if solution three is stable
```

```
    if isreal(total3)==1

C311=A(1,1)*(Ly^4)*(b(3)^2)/1280+A(1,2)*(Ly^2)*(Lx^2)*(b(3)
)^2/1152
     +A(2,2)*(Lx^4)*(b(3))^2/1280+B(1,1)*(Ly^2)*b(3)/24+B(1
     ,2) *(Lx^2)*b(3)/24+D(1,1);
C312=A(1,1)*(-c(3)*(Ly^2)/48+a(3)*(Ly^4)*b(3)/640)+A(1,2)
     *(a(3)*b(3)*(Ly^2)*(Lx^2)/576-d(3)*(Ly^2)/48-
     c(3)*(Lx^2)/48)+A(2,2)*(a(3)*b(3)*(Lx^4)/640-
     d(3)*(Lx^2)/48)+B(1,1)*a(3)*(Ly^2)/24+B(1,2)*(a(3)*(Lx
     ^2)/24+b(3)*(Ly^2)/24)+B(2,2)*b(3)*(Lx^2)/24+D(1,2)+Nx
     T*temp*(Ly^2)/48+NyT*temp*(Lx^2)/48;
C313=-A(1,1)*b(3)*(Ly^2)/48-A(1,2)*b(3)*(Lx^2)/48-B(1,1);
C314=-A(1,2)*b(3)*(Ly^2)/48-A(2,2)*b(3)*(Lx^2)/48-B(1,2);
C322=A(1,1)*(a(3)^2)*(Ly^4)/1280+A(1,2)*(a(3)^2)*(Ly^2)*(Lx
^2)/1152
     +A(2,2)*(a(3)^2)*(Lx^4)/1280+B(1,2)*a(3)*(Ly^2)/24+B(2
     ,2) *a(3)*(Lx^2)/24+D(2,2);
C323=-A(1,1)*a(3)*(Ly^2)/48-A(1,2)*a(3)*(Lx^2)/48-B(1,2);
C324=-A(1,2)*a(3)*(Ly^2)/48-A(2,2)*a(3)*(Lx^2)/48-B(2,2);
C333=A(1,1);
C334=A(1,2);
C344=A(2,2);

    C3=[C311 C312 C313 C314
        C312 C322 C323 C324
        C313 C323 C333 C334
        C314 C324 C334 C344];

        v3=eig(C3);

        if v3(1)>0
            if v3(2)>0
                if v3(3)>0
                    if v3(4)>0
                        disp('Solution three is stable')
                        eox=c(3);
                        eoy=d(3);
                        eoxy=0;
                        kx=-a(3);
                        ky=-b(3);
                        kxy=0;
                        rhox=1/(a(3));
                        rhoy=1/(b(3));
                    end
                end
            end
```

```
        else
            disp('Solution three is unstable')
        end

h=a(3)*(1-cos(Lx/2/a(3))^2)*1000;
disp('The dome height of actuator three is [mm]'); disp(h)

dx=Lx/50;
dy=dx;
m=0;

for x=-Lx/2:dx:Lx/2
   m=m+1;
   xdum(m)=x;
   p=0;
   for y=-Ly/2:dy:Ly/2
      p=p+1;
      ydum(p)=y;
      w3(p,m)=1/2*(a(3)*x^2+b(3)*y^2);
   end
end
figure
surf(xdum,ydum,w3)
xlabel('Lx [mm]')
ylabel('Ly [mm]')
zlabel('h [mm]')
title('Solution Three Actuator')

   else
       disp('Solution set three is not a viable solution')
   end

%determining whether solution four is usable
   total4=a(4)+b(4)+c(4)+d(4);

%determining if solution four is stable
   if isreal(total4)==1

C411=A(1,1)*(Ly^4)*(b(4)^2)/1280+A(1,2)*(Ly^2)*(Lx^2)*(b(4)
)^2/1152
     +A(2,2)*(Lx^4)*(b(4))^2/1280+B(1,1)*(Ly^2)*b(4)/24+B(1
     ,2) *(Lx^2)*b(4)/24+D(1,1);
C412=A(1,1)*(-c(4)*(Ly^2)/48+a(4)*(Ly^4)*b(4)/640)+A(1,2)
     *(a(4)*b(4)*(Ly^2)*(Lx^2)/576-d(4)*(Ly^2)/48-
     c(4)*(Lx^2)/48)+A(2,2)*(a(4)*b(4)*(Lx^4)/640-
     d(4)*(Lx^2)/48)+B(1,1)*a(4)*(Ly^2)/24+B(1,2)*(a(4)*(Lx
```

```
     ^2)/24+b(4)*(Ly^2)/24)+B(2,2)*b(4)*(Lx^2)/24+D(1,2)+Nx
     T*temp*(Ly^2)/48+NyT*temp*(Lx^2)/48;
C413=-A(1,1)*b(4)*(Ly^2)/48-A(1,2)*b(4)*(Lx^2)/48-B(1,1);
C414=-A(1,2)*b(4)*(Ly^2)/48-A(2,2)*b(4)*(Lx^2)/48-B(1,2);
C422=A(1,1)*(a(4)^2)*(Ly^4)/1280+A(1,2)*(a(4)^2)*(Ly^2)*(Lx
^2)/1152
     +A(2,2)*(a(4)^2)*(Lx^4)/1280+B(1,2)*a(4)*(Ly^2)/24+B(2
     ,2)*a(4)*(Lx^2)/24+D(2,2);
C423=-A(1,1)*a(4)*(Ly^2)/48-A(1,2)*a(4)*(Lx^2)/48-B(1,2);
C424=-A(1,2)*a(4)*(Ly^2)/48-A(2,2)*a(4)*(Lx^2)/48-B(2,2);
C433=A(1,1);
C434=A(1,2);
C444=A(2,2);

    C4=[C411 C412 C413 C414
        C412 C422 C423 C424
        C413 C423 C433 C434
        C414 C424 C434 C444];

        v4=eig(C4);

        if v4(1)>0
            if v4(2)>0
                if v4(3)>0
                    if v4(4)>0
                        disp('Solution four is stable')
                        eox=c(4);
                        eoy=d(4);
                        eoxy=0;
                        kx=-a(4);
                        ky=-b(4);
                        kxy=0;
                        rhox=1/(a(4));
                        rhoy=1/(b(4));
                    end
                end
            end
        else
            disp('Solution four is unstable')
        end

 h=a(4)*(1-cos(Lx/2/a(4))^2)*1000;
 disp('The dome height of actuator four is [mm]'); disp(h)

 dx=Lx/50;
 dy=dx;
 m=0;
```

```
 for x=-Lx/2:dx:Lx/2
    m=m+1;
    xdum(m)=x;
    p=0;
    for y=-Ly/2:dy:Ly/2
       p=p+1;
       ydum(p)=y;
       w4(p,m)=1/2*(a(4)*x^2+b(4)*y^2);
    end
 end
 figure
 surf(xdum,ydum,w4)
 xlabel('Lx [mm]')
 ylabel('Ly [mm]')
 zlabel('h [mm]')
 title('Solution Four Actuator')

    else
        disp('Solution set four is not a viable solution')
    end

 %determining whether solution five is usable
    total5=a(5)+b(5)+c(5)+d(5);



%determining if solution five is stable
    if isreal(total5)==1

C511=A(1,1)*(Ly^4)*(b(5)^2)/1280+A(1,2)*(Ly^2)*(Lx^2)*(b(5)
)^2/1152
     +A(2,2)*(Lx^4)*(b(5))^2/1280+B(1,1)*(Ly^2)*b(5)/24+B(1
     ,2)*(Lx^2)*b(5)/24+D(1,1);
C512=A(1,1)*(b(5)*(Ly^2)/48+a(5)*(Ly^4)*b(5)/640)+A(1,2)*(a
(5)*b(5)
     *(Ly^2)*(Lx^2)/576-d(5)*(Ly^2)/48-
     c(5)*(Lx^2)/48)+A(2,2)*(a(5)*b(5)*(Lx^4)/640-
     d(5)*(Lx^2)/48)+B(1,1)*a(5)*(Ly^2)/24+B(1,2)*(a(5)*(Lx
     ^2)/24+b(5)*(Ly^2)/24)+B(2,2)*b(5)*(Lx^2)/24+D(1,2)+Nx
     T*temp*(Ly^2)/48+NyT*temp*(Lx^2)/48;
C513=-A(1,1)*b(5)*(Ly^2)/48-A(1,2)*b(5)*(Lx^2)/48-B(1,1);
C514=-A(1,2)*b(5)*(Ly^2)/48-A(2,2)*b(5)*(Lx^2)/48-B(1,2);
C522=A(1,1)*(a(5)^2)*(Ly^4)/1280+A(1,2)*(a(5)^2)*(Ly^2)*(Lx
^2)/1152
     +A(2,2)*(a(5)^2)*(Lx^4)/1280+B(1,2)*a(5)*(Ly^2)/24+B(2
     ,2)*a(5)*(Lx^2)/24+D(2,2);
```

```
C523=-A(1,1)*a(5)*(Ly^2)/48-A(1,2)*a(5)*(Lx^2)/48-B(1,2);
C524=-A(1,2)*a(5)*(Ly^2)/48-A(2,2)*a(5)*(Lx^2)/48-B(2,2);
C533=A(1,1);
C534=A(1,2);
C544=A(2,2);

    C5=[C511 C512 C513 C514
        C512 C522 C523 C524
        C513 C523 C533 C534
        C514 C524 C534 C544];

        v5=eig(C5);

        if v5(1)>0
            if v5(2)>0
                if v5(3)>0
                    if v5(4)>0
                        disp('Solution five is stable')
                        eox=c(5);
                        eoy=d(5);
                        eoxy=0;
                        kx=-a(5);
                        ky=-b(5);
                        kxy=0;
                        rhox=1/(a(5));
                        rhoy=1/(b(5));
                    end
                end
            end
        else
            disp('Solution five is unstable')
        end

 h=a(5)*(1-cos(Lx/2/a(5))^2)*1000;
 disp('The dome height of actuator five is [mm]'); disp(h)

 dx=Lx/50;
 dy=dx;
 m=0;

 for x=-Lx/2:dx:Lx/2
    m=m+1;
    xdum(m)=x;
    p=0;
    for y=-Ly/2:dy:Ly/2
       p=p+1;
       ydum(p)=y;
```

```
       w5(p,m)=1/2*(a(5)*x^2+b(5)*y^2);
    end
 end
 figure
 surf(xdum,ydum,w5)
 xlabel('Lx [mm]')
 ylabel('Ly [mm]')
 zlabel('h [mm]')
 title('Solution Five Actuator')

    else
        disp('Solution set five is not a viable solution')
    end


    hx=rhox*1000*(1-cos((Lx)/(2*rhox)));
    disp('The dome height of the actuator as determined by
CLT is
          [mm]') ;disp(abs(hx))


%plotting the strains through the thickness of the actuator
%assuming x=0 and y=0

for q=h(1)*1000:.01:-h(1)*1000
    g=g+1;
    r(g)=q/1000;
    ex(g)=(r(g)/rhox+eox)*1e6;
    ey(g)=(r(g)/rhoy+eoy)*1e6;
end

%Plot of strain in x-direction
 figure
 plot(ex,r*1000,'r')
 hold on

for i=1:n;
    plot([ex(1) ex(g)],[h(i) h(i)]*1000)
end

    plot([ex(1) ex(g)],[h(n+1) h(n+1)]*1000)
    xlabel('Epsilon_x_x (um/m)')
    ylabel('Thickness (mm)')

%Plot of strain in y-direction
 figure
 plot(ey,r*1000,'g')
```

```
 hold on

for i=1:n;
    plot([ey(1) ey(g)],[h(i) h(i)]*1000)
end

    plot([ey(1) ey(g)],[h(n+1) h(n+1)]*1000)
    xlabel('Epsilon_y_y (um/m)')
    ylabel('Thickness (mm)')



resolution=0.001;

%Plotting the stresses over the thickness
for i=1:n
    for v=h(i+1)*1000:-resolution:h(i)*1000
        k=k+1;
        j(k)=v/1000;
        if i==num
           sigmax(k)=([Q11bar(i)
Q12bar(i)Q16bar(i)]*[eox;eoy;eoxy]
                    +[Q11bar(i)Q12bar(i) Q16bar(i)]*j(k)*
                    [kx;ky;kxy]-[Q11bar(i) Q12bar(i)
                    Q16bar(i)]*[alphax(i);alphay(i);alphaxy
                    (i)]*temp-[Q11bar(i) Q12bar(i)
                    Q16bar(i)]*[d31;d31;0]*E)/1e6;

           sigmay(k)=([Q12bar(i)
Q22bar(i)Q26bar(i)]*[eox;eoy;eoxy]
                    +[Q12bar(i)Q22bar(i) Q26bar(i)]*j(k)*
                    [kx;ky;kxy]-[Q12bar(i) Q22bar(i)
                    Q26bar(i)
                    ]*[alphax(i);alphay(i);alphaxy(i)]*temp
                    -[Q12bar(i) Q22bar(i)
                    Q26bar(i)]*[d31;d31;0]*E)/1e6;

                        else

sigmax(k)=(([Q11bar(i)Q12bar(i)Q16bar(i)]*[eox;eoy;eoxy]
                    )+([Q11bar(i)Q12bar(i) Q16bar(i)]*j(k)*
                    [kx;ky;kxy])-([Q11bar(i) Q12bar(i)
                    Q16bar(i)]*[alphax(i);alphay(i);alphaxy
                    (i)]*temp))/1e6;

sigmay(k)=(([Q12bar(i)Q22bar(i)Q26bar(i)]*[eox;eoy;eoxy]
```

```
                    )+([Q12bar(i)Q22bar(i) Q26bar(i)]*j(k)*
                    [kx;ky;kxy])-([Q12bar(i) Q22bar(i)
                    Q26bar(i)]*[alphax(i);alphay(i);alphaxy
                    (i)]*temp))/1e6;
        end

 %Checking the equilibrium of actuator

 if k > 1
    if sigmax(k)>0
       posx = posx + (((sigmax(k)+sigmax(k-
1))/2)*resolution);
    else
       negx = negx + (((sigmax(k)+sigmax(k-
1))/2)*resolution);
    end

    if sigmax(k)>0
       posy = posy + (((sigmay(k)+sigmay(k-
1))/2)*resolution);
    else
       negy = negy + (((sigmay(k)+sigmay(k-
1))/2)*resolution);
    end
   end
  end
 end

if abs(posx + negx) < 0.1
   disp('Laminate is in equilibrium in x-direction')
else
   disp('Laminate is not in equilibrium in x-direction')
end

if abs(posy + negy) < 0.1
   disp('Laminate is in equilibrium in y-direction')
else
   disp('Laminate is not in equilibrium in y-direction')
end



%Plot of stresses in x-direction
 figure
 plot(sigmax,j*1000,'r.')
 hold on
```

```
 for i=1:n;
     plot([min(sigmax) max(sigmax)],[h(i) h(i)]*1000)
 end

     plot([min(sigmax) max(sigmax)],[h(n+1) h(n+1)]*1000)
          xlabel('Sigma_x_x (MPa)'),ylabel('Thickness
(mm)')

%Plot of stresses in y-direction
 figure
 plot(sigmay,j*1000,'g.')
 hold on

 for i=1:n;
     plot([min(sigmay) max(sigmay)],[h(i) h(i)]*1000)
 end

     plot([min(sigmay) max(sigmay)],[h(n+1) h(n+1)]*1000)
          xlabel('Sigma_y_y (MPa)'),ylabel('Thickness
(mm)')
```

REFERENCES

Aimmanee, S. and M. W. Hyer (2004). "Analysis of the manufactured shape of rectangular THUNDER-type actuators". *Smart Materials and Structures*. Vol 13. pp 1389-1406.

Akay, M., S. Kong Ah Mun, and A. Stanley (1997). "Influence of moisture on the thermal and mechanical properties of autoclaved and oven-cured Kevlar 49/epoxy laminates". *Composites Science and Technology*. Vol. 57. pp. 565-571.

Brown, D.F. (2003). "Single Crystal Piezoelectric Pumping Using Displacement Amplification." Master's Thesis. Atlanta, GA, Georgia Institute of Technology.

Cady, W. G. (1964). Piezoelectricity: an introduction to the theory and applications of electromechanical phenomena in crystals. Vol. 1, Dover Publications, Inc. New York.

Clark, R.L., and C.R. Fuller, (1993). "Active control of structurally radiated sound from an enclosed finite cylinder". *Proceedings of the 2nd Conference on Recent Advances in Active Control of Sound and Vibration*. pp. 380-402.

Daniel, I. M., T.M. Wang, D. Karalekas, and J. T. Goltro (1990). "Determination of Chemical Cure Shrinkage in Composite Laminates". *American Society for Testing and Materials*. pp. 172-176

Dano, M. L. and M. W. Hyer (1998). "Thermally-induced deformation behavior of unsymmetric laminates". *International Journal of Solids Structures*. Vol. 35. No. 17, pp. 2101-2120.

Gigliotti, M., M. R. Wisnom, and K. D. Potter (2003). "Development of curvature during the cure of AS4/8552 [0/90] unsymmetric composite plates" . *Composites Science and Technology*. Vol. 63. pp. 187-197.

Haertling, G.H. (1994). "Rainbow Ceramic: A New Type of Ultra High Displacement Actuator". American Ceramic Society Bulletin, Vol. 73, pp. 93-96.

Hamamoto, A. and M. W. Hyer (1987). "Non-linear temperature-curvature relationships for unsymmetric graphite-epoxy laminates". *International Journal of Solids Structures*. Vol. 23. No. 7, pp. 919-935.

Herakovich, C.T. (1998). Mechanics of Fibrous Composites. New York, NY, Wiley.

Hopkinson, D. 2003. "Development of stress gradient enhanced piezoelectric unimorph actuator composites". MS. Thesis, Georgia Institute of Technology, Georgia, Atlanta.

Hyer, M. W. (1981a). "Some observations on the cured shape of thin unsymmetric laminates". *Journal of Composite Materials*. Vol. 15. pp. 175-194.

Hyer, M. W. (1981b). "Calculation of the room-temperature shapes of unsymmetric laminates". *Journal of Composite Materials*. Vol. 15. pp. 296-310.

Hyer, M. W. (1982). "The room-temperature shapes of four-layer unsymmetric cross-ply laminates". *Journal of Composite Materials*. Vol. 16. pp. 318-340.

Hyer, M. W. and A. Jilani (1998). "Predicting the deformation characteristics of rectangular unsymmetrically laminates piezoelectric materials". *Smart Materials and Structures*. Vol. 7. pp. 784-791.

Jaffe, B., W.R. Cook, and H. Jaffe (1971). Piezoelectric Ceramics, Second Edition. Marietta, OH, Academic Press Limited, Reprinted by CBLS.

Jones, M. J. (1999). Mechanics of Composite Materials, Second Edition. Philadelphia, PA, Taylor and Francis, Inc.

Kugel, V.D., S. Chandran, and L.E. Cross. (1997). "A comparative analysis of piezoelectric bending-mode actuators". *SPIE*. Vol. 3040. pp 70-79.

Lahtinen, H. (2003). "Calculation of Residual Stresses of Cross-ply Laminates". *Journal of Composite Materials*. Vol. 37. No. 11, pp.945-966.

Lines, M.E., A.M. Glass. (1977). Principles and Applications of Ferroelectrics and Related Materials. Clarendon Press. Oxford.

Love, A.E.H. (1927). A Treatise on the Mathematical Theory of Elasticity, Fourth Edition. Cambridge, UK, Cambridge University Press.

Lynch, C.S. (1996). "The Effect of Uniaxial Stress on the Electro-Mechanical Response of 8/65/35 PLZT". *Acta Mater*. Vol. 44. No.10, pp. 4137-4148.

Mallick, P.K. (1993). Fiber-Reinforced Composites: Materials, Manufacturing, and Design, Second Edition. New York, NY, Marcel Dekker.

Mauck, L.D. (2002). "The Role of Rate Dependence and Dissipation in the Constitutive Behavior of Ferroelectric Ceramics for High Power Applications." Ph.D. Thesis. Atlanta, GA, Georgia Institute of Technology.

Mulling, J., T. Usher, B. Dessent, J. Palmer, P. Franzon, E. Grant, and A. Kingon (2000) "High Displacement Piezoelectric Actuators: Characterization at High Load with Controlled End Conditions". *IEEE International Symposium on Applications of Ferroelectrics*. Vol. 2. pp. 745-748.

Ounaies, Z., K. Mossi, R. Smith, and J. Bernd (2001). “Low-field and high-field characterization of THUNDER actuators”. *ICASE Report No. 2001-9*, NASA Langley Research Center, Hampton, VA.

Perrin, V., M. Troccaz, and P. Gonnard (2000). “Non linear behavior of the permittivity and of the piezoelectric strain constant under high electric field drive”. *Journal of Electroceramics*. Vol. 4. No. 1, pp 189-194.

Pister, K.S. and S.B. Dong (1959). “Elastic bending of layered plates”. *Journal of the Engineering Mechanics Division*. ASCE, October, pp 1-10.

Reissner E. and Y. Stavsky (1961). “Bending and stretching of certain types of heterogeneous aeolotropic elastic plates”. *Journal of Applied Mechanics*. September, pp. 402-408.

Roylance, D. and M. Roylance (1976). “Influence of ourdoor weathering on dynamic mechanical properties of glass/epoxy laminate”. *Environmental Effects on Advanced Composite Materials, ASTM STP 602*. pp. 85-94.

Schlecht, M., K. Schulte, and M. W. Hyer (1995). “Advanced calculation of the room-temperature shapes of thin unsymmetric composite laminates”. *Composite Structures*. Vol 32. pp. 627-633.

Simpson, M.A., T.M. Luong, C.R. Fuller, and J.D. Jones. (1991). “Full-scale demonstration tests of cabin noise reduction using active vibration control”. *J. Aircraft*. Vol. 28. No. 3, pp. 208-215.

Smits, J.G., S.I. Dalke, and T.H. Cooney (1990). "The Constituent Equations of Piezoelectric Bimorphs". *Sensors and Actuators A: Physical*, Vol. 28, pp. 41-61.

Sturgeon, J. B. (1978). “Creep of fibre reinforced thermosetting resins”. *Creep of Engineering Materials*, Mechanical Engineering Publishing Ltd., London (1978).

Sumali, H., H. Cudney, and J. Vipperman. (1991). “Vibration Control of Cylinders using Piezoelectric Sensors and Actuators”. *Proceedings of ADPA Conference.*

Wisnom, M. R. (2004). “Development of Residual Stresses and Distortion During the Cure of Polymer Matrix Composites”. *Proceedings of the Joint American Society for Composites/American Society for Testing and Materials Committee D30*, Oct. 17-20, Atlanta.

White, P.H., and R.J. Sawley. (1972). “Energy transmission in piping systems and its relation to noise control,” *American Society of Mechanical Engineering Journal of Engineering for Industry.* Vol. 94. Ser. B. No. 2, pp 745-751.

Yoon, K.J., J.H. Chung, N.S. Goo, and H.C. Park (2001). “Thermal deformation and

residual stress analysis of lightweight piezo-composite curved actuator device". *Proceedings of SPIE Conference*, Newport Beach, CA, USA. SPIE proceeding series 2001:4333-68.

Yoon, K. J. and J. S. Kim (2001). "Effect of Thermal Deformation and Chemical Shrinkage on the Process Induced Distortion of Carbon/Epoxy Curved Laminates". *Journal of Composite Materials*. Vol. 35. No. 03, pp.253-263.

Yoon, K. J., S. S. Shin, H.C. Park, and M.K. Kwak (2000). "Development of lightweight THUNDER with fiber composite layers". *Proceedings of SPIE Conference*, Newport Beach, CA, USA. SPIE proceeding series 2000:3992-06.